Spatiotemporally resolved photoemission from plasmonic nanoparticles

by

Jianxiong Li

B.S., Beihang University, China, 2010

AN ABSTRACT OF A DISSERTATION

submitted in partial fulfillment of the
requirements for the degree

DOCTOR OF PHILOSOPHY

Department of Physics
College of Arts and Sciences

KANSAS STATE UNIVERSITY
Manhattan, Kansas

2020

Abstract

Streaked photoemission from nanostructured surfaces and nanoparticles by attosecond extreme ultraviolet (XUV) pulses into an infrared (IR) or visible streaking pulse allows for sub-femtosecond resolution of the plasmonically enhanced streaking-pulse electric field. It holds promise for the temporally and spatially resolved imaging of the dielectric response near nanostructures. In this dissertation, I present four distinct yet interconnected aspects of numerically modeling plasmonic reconstruction by the photoemission from nanoparticles.

First, I present a theoretical model of simulating the IR-streaked XUV photoemission spectra, by calculating (a) the plasmonic field induced by IR pulses within Mie theory, and (b) the T-matrix elements for photoemission using a quantum-mechanical model. The simulation results show significant oscillation-amplitude enhancements and phase shifts, comparing to calculations without the induced plasmonic field. These observable effects can be traced to the dielectric properties of the nanoparticles, demonstrating the applicability of streaking spectroscopy to the investigation of induced plasmonic effect near nanoparticles and nanostructured surfaces.

Second, based on this model, I propose a scheme for the reconstruction of plasmonic near-fields at isolated nanoparticles from streaked photoelectron spectra. The success of this proposed scheme is demonstrated by the accurate imaging of the IR-streaking-pulse-induced plasmonic fields at the surface of gold nanospheres and nanoshells with sub-femtosecond temporal and sub-nanometer spatial resolution.

Third, I further improve the physical accuracy of the model, by developing a semi-classical approach, ACCTIVE, to solve the time-dependent Schrödinger's equation in spatially inhomogeneous electromagnetic fields. I demonstrate the validation of this method by studying electron final-state wavefunctions in Coulomb and laser fields, before applying these improved final photoelectron states to streaked photoemission from hydrogen atoms. The results show

excellent quantitative agreement with direct solution of the Schrödinger's equation. Implementing this method to simulating the streaked photoemission from Au nanospheres shows better agreement in plasmonic-field reconstruction for low energy photoelectrons than previous strong-field-approximation simulations.

Finally, I extend the previous work and explore the non-linear optical response of nanoparticles observed in momentum imaging experiments at the Kansas State University Department of Physics. My Mie simulations, by including intensity-dependent index of refraction, show a significant non-linear effect in SiO_2-core-Au-shell nanoparticles in response to 10^{10} - 10^{12} W/cm^2 intensity and 780 nm central wavelength IR pulses. This effect is responsible for the change in the experimentally observed photoelectron "cut-off" energies, as a function of the external pulse intensity, suggesting the non-linear optical response to be a significant factor in strong-field photoemission from plasmonic nanoparticles.

Spatiotemporally resolved photoemission from plasmonic nanoparticles

by

Jianxiong Li

B.S., Beihang University, China, 2010

A DISSERTATION

submitted in partial fulfillment of the
requirements for the degree

DOCTOR OF PHILOSOPHY

Department of Physics
College of Arts and Sciences

KANSAS STATE UNIVERSITY
Manhattan, Kansas

2020

Approved by:

Major Professor
Uwe Thumm

Copyright

© Jianxiong Li 2020.

Abstract

Streaked photoemission from nanostructured surfaces and nanoparticles by attosecond extreme ultraviolet (XUV) pulses into an infrared (IR) or visible streaking pulse allows for sub-femtosecond resolution of the plasmonically enhanced streaking-pulse electric field. It holds promise for the temporally and spatially resolved imaging of the dielectric response near nanostructures. In this dissertation, I present four distinct yet interconnected aspects of numerically modeling plasmonic reconstruction by the photoemission from nanoparticles.

First, I present a theoretical model of simulating the IR-streaked XUV photoemission spectra, by calculating (a) the plasmonic field induced by IR pulses within Mie theory, and (b) the T-matrix elements for photoemission using a quantum-mechanical model. The simulation results show significant oscillation-amplitude enhancements and phase shifts, comparing to calculations without the induced plasmonic field. These observable effects can be traced to the dielectric properties of the nanoparticles, demonstrating the applicability of streaking spectroscopy to the investigation of induced plasmonic effect near nanoparticles and nanostructured surfaces.

Second, based on this model, I propose a scheme for the reconstruction of plasmonic near-fields at isolated nanoparticles from streaked photoelectron spectra. The success of this proposed scheme is demonstrated by the accurate imaging of the IR-streaking-pulse-induced plasmonic fields at the surface of gold nanospheres and nanoshells with sub-femtosecond temporal and sub-nanometer spatial resolution.

Third, I further improve the physical accuracy of the model, by developing a semi-classical approach, ACCTIVE, to solve the time-dependent Schrödinger's equation in spatially inhomogeneous electromagnetic fields. I demonstrate the validation of this method by studying electron final-state wavefunctions in Coulomb and laser fields, before applying these improved final photoelectron states to streaked photoemission from hydrogen atoms. The results show

excellent quantitative agreement with direct solution of the Schrödinger's equation. Implementing this method to simulating the streaked photoemission from Au nanospheres shows better agreement in plasmonic-field reconstruction for low energy photoelectrons than previous strong-field-approximation simulations.

Finally, I extend the previous work and explore the non-linear optical response of nanoparticles observed in momentum imaging experiments at the Kansas State University Department of Physics. My Mie simulations, by including intensity-dependent index of refraction, show a significant non-linear effect in SiO_2-core-Au-shell nanoparticles in response to 10^{10} - 10^{12} W/cm^2 intensity and 780 nm central wavelength IR pulses. This effect is responsible for the change in the experimentally observed photoelectron "cut-off" energies, as a function of the external pulse intensity, suggesting the non-linear optical response to be a significant factor in strong-field photoemission from plasmonic nanoparticles.

Table of Contents

List of Figures xi

List of Tables xiv

Acknowledgements xv

Dedication xvii

1 Introduction 1

1.1 Background and motivation 1

1.1.1 Recent developments of nanoscience and technology 1

1.1.2 Recent developments of laser technology 2

1.2 Challenges of moving towards complex targets 4

1.2.1 Physical phenomena beyond atomic and molecular targets 4

1.2.2 Challenges in theoretical modeling 5

1.3 Dissertation overview 6

2 Streaked photoemission from plasmonic nanoparticles 8

2.1 Numerical model 10

2.1.1 Induced plasmonic response to the streaking field 10

2.1.2 Quantum-mechanical photoemission amplitude 16

2.1.3 Evaluation of the photoemission amplitude 18

2.1.4 Summation over initial states 19

2.2 Streaked photoelectron spectra 21

2.2.1 Size and streaking-wavelength dependence 21

2.2.2 Comparison with classical calculations . . . 26
2.2.3 Plasmonic-field-information retrieval . . . 28
2.3 Summary . . . 35

3 Imaging plasmonic fields with atomic spatiotemporal resolution . . . 36
3.1 Suggested experimental setup . . . 37
3.2 Simulation of photoelectron spectra . . . 38
3.2.1 Numerical model . . . 38
3.2.2 Simulated spectra . . . 40
3.3 Plasmonic field reconstruction . . . 41
3.3.1 Mathematical derivation . . . 41
3.3.2 Plasmonic field reconstruction of Au nanospheres . . . 43
3.3.3 Plasmonic field reconstruction of Au nanoshells . . . 46
3.4 Summary . . . 50

4 A semi-classical approach for solving the time-dependent Schrödinger equation in spatially inhomogeneous electromagnetic pulses . . . 51
4.1 Theory . . . 52
4.2 Examples . . . 57
4.2.1 Volkov wavefunction . . . 57
4.2.2 Coulomb wavefunction . . . 58
4.2.3 Coulomb-Volkov wavefunction . . . 59
4.2.4 Streaked photoemission from hydrogen atoms . . . 61
4.2.5 Streaked photoemission from metal nanospheres . . . 62
4.3 Summary . . . 65

5 Tracking the non-linear optical response in plasmonic nanoparticles with strong-field photoemission spectroscopy . . . 68
5.1 Experimental setup . . . 69

5.2 Size-dependent photoelectron cut-off energies . . . 71
5.3 Intensity-dependent photoelectron cut-off energies . . . 73
5.4 Summary . . . 79

6 Conclusion and outlook . . . 81
6.1 Streaked photoemission from plasmonic nanoparticles . . . 81
6.2 Plasmonic field imaging . . . 82
6.3 ACCTIVE method . . . 82
6.4 Non-linear optical response in nanoparticles . . . 83

Publications . . . 84

Bibliography . . . 85

Appendix A Mathematical derivation of plasmonic field reconstruction . . . 101
A.1 Evaluation of the spatial integral in Eq. (3.3) . . . 101
A.2 Evaluation of Eq. (3.11) . . . 102
A.2.1 Simplification of Eq. (A.6) . . . 103
A.2.2 Integration over $\mathcal{E}_f$ in Eq. (A.7) . . . 105
A.2.3 Integration over the initial-state energy . . . 106

Appendix B Mathematical derivation and comments on three applications of the ACCTIVE method . . . 108
B.1 Derivation of Eq. (4.19) . . . 108
B.2 Numerical calculation of Coulomb wavefunctions using ACCTIVE . . . 109
B.3 Comments on streaked photoemission from Au nanospheres . . . 113

List of Figures

1.1 Illustration of collective oscillation of electrons with the incident electromagnetic field . . . 2

1.2 Schematic of the attosecond streaking from atomic gas target . . . 3

2.1 Schematic of attosecond streaking from nanoparticles . . . 9

2.2 Real and imaginary components of the complex permittivity $\epsilon(\omega)$ for Au, Ag, and Cu . . . 11

2.3 Plasmonic field enhancement and phase shift of various Au nanospheres . . . 13

2.4 Plasmonic field enhancement and phase shift of various Ag nanospheres . . . 14

2.5 Plasmonic field enhancement and phase shift of various Cu nanospheres . . . 14

2.6 Simulated streaked XUV photoemission spectra for 10 and 50 nm diameter Au nanospheres . . . 22

2.7 Simulated streaked XUV photoemission spectra for 10 and 50 nm diameter Ag nanospheres . . . 23

2.8 Simulated streaked XUV photoemission spectra for 10 and 50 nm diameter Cu nanospheres . . . 24

2.9 Comparison of streaked XUV photoemission spectra using quantum-mechanical and classical models . . . 27

2.10 Centers-of-energy of streaked XUV photoemission spectra for 10 nm diameter Au, Ag, and Cu nanospheres . . . 29

2.11 Plasmonic amplitude-enhancement and phase-shift retrieval for Au nanospheres 31

2.12 Plasmonic amplitude-enhancement and phase-shift retrieval for Ag nanospheres 32

2.13 Plasmonic amplitude-enhancement and phase-shift retrieval for Cu nanospheres 33

3.1 Schematic of attosecond nanoplasmonic imaging 37
3.2 Streaked photoelectron spectra for 50 nm radius Au nanospheres 40
3.3 Time-resolved reconstruction of the plasmonic field of Au nanospheres . . . 44
3.4 Spatiotemporal reconstruction of the plasmonic field for Au nanospheres and nanoshells 45
3.5 Average error of field reconstruction 46
3.6 Simulated electric field-strength distribution of an Au nanosphere and an Au nanoshell 47
3.7 Simulated wavelength-dependent plasmonic field-strength enhancement of an Au nanosphere and an Au nanoshell 48
3.8 Time-resolved reconstruction of the plasmonic field of Au nanoshells 49

4.1 Illustration of the shooting method used for determining classical trajectories 56
4.2 Comparison of analytical and ACCTIVE-simulated Coulomb wavefunctions . 59
4.3 Comparison of Coulomb, ACCTIVE-calculated Coulomb-Volkov, and Volkov wavefunctions 61
4.4 Comparison of streaked photoelectron spectra from hydrogen simulated using ACCTIVE-calculated final states, SFA, and directly solving TDSE 63
4.5 Comparison of streaked photoelectron spectra and plasmonic field reconstruction from Au nanospheres, using ACCTIVE final-states and SFA 66

5.1 High energy VMI spectrometer coupled to nanoparticle source 70
5.2 Size-dependent study of experimentally measured maximum cut-off energy and theoretically simulated plasmonic near-field enhancement 72
5.3 Intensity-dependent study of experimentally measured maximum cut-off energy, theoretically simulated plasmonic near-field enhancement, IR skin depth, and trasmitted field intensity 74

5.4 Mie simulated spatial distribution of electric field intensity and wave-length dependent plasmonic near-field enhancement as various intensities 78

B.1 Two possible classical trajectories passing through $(\mathbf{r}, t)$ satisfying the same outgoing plane wave boundary condition. 110

B.2 Illustration of the superposition of two possible velocity fields 111

B.3 Comparison of ACCTIVE wavefunction and SFA modeled wavefunction as final states of streaked photoemission from Au nanospheres, and corresponding photoemission cross section 113

List of Tables

2.1 Workfunctions, conduction-band widths, and mean-free-paths (MFP) for Au, Ag, and Cu 18

Acknowledgments

The journey of pursuing my Ph.D. degree is not a journey that I can finish on my own. I am grateful that I am surrounded by these amazing people, who helped and supported me during through journey. To them, I would like to address my sincere gratitude.

First of all, to my advisor, Dr. Uwe Thumm, for his teaching, guidance, and encouragement during these years. His knowledge and vision in atomic, molecular and optical physics, as well as encouragement to me to explore my own ideas, help me to establish myself as a young researcher in this field. He is a kind and patient person to work with, and I will always be grateful to have him as my advisor and mentor.

To the committee members, Dr. Artem Rudenko, Dr. Christopher Sorensen, Dr. Christine Aikens, and the outside chairperson, Dr. Donald Fenton, for their insightful discussion with my research, and their time and effort of reviewing my dissertation.

To my colleagues in Dr. Uwe Thumm's group, both previous and present, including Erfan Saydanzad, who I had the pleasure to most closely work with, Dr. Qing Liao, who helped me with many research methods and ideas when I first joined the group, and Dr. Aihua Liu, Dr. Maia Magrakvelidze, Dr. Marcelo Ambrosio, Dr. Francisco Navarrete, Dr. Paul Abanador, Hongyu Shi, and Alex Kramer. They are not only colleagues that helped me with my research, but also friends in life.

To Dr. Jeffrey Powell, a previous member of Dr. Rudenko's group, whom I had the pleasure to closely work with in the experiment-theory collaboration, for the amazing experimental work and insightful discussion. This pleasant collaboration then becomes an important building block of my dissertation.

To Dr. Carlos Trallero-Herrero and his group, especially Dr. Adam Summers, for their experimental work and insightful input, which greatly helps with my research, particularly the most recent collaboration.

To the professors in Physics Department, whom I am most fortunate to learn from in the their courses and discussions, especially Dr. Brett Esry, Dr. Chii-Dong Lin, Dr. Bharat Ratra, Dr. Jeremy Schmit and Dr. Andrew Ivanov.

To the professors outside of Physics Department, whom I had the pleasure to learned from in their courses, Dr. Shing-I Chang and Dr. Xinmin Ou.

To the professors and staffs whom I worked with as Teaching Assistant during the past years, Dr. Tim Bolton, Dr. Bret Flanders, Dr. Muhammad Farooq, Barbara Steward, and Peter Nelson.

To the support staffs in Physics Department, both previous and present, especially Larry McFeeters and Vince Needham for maintaining the computing resources for our research needs, and Kim Coy, Kim Elliott, and Peggy Matthews for the help with office work.

To all my colleagues and friends in Physics Department, for helping me with my research and course work, and being friends in life.

To my dear father Zhi Li, mother Shufen Zhang, and grandmother Zhengxiu Nie, for loving and raising me, and supporting me through this long journey far from home.

To my dear aunt Hong Li, uncle Hui Ouyang, and cousins Kelly Ouyang, Chris Ouyang, and Cindy Ouyang, for their love and support, making Kansas my second home.

To my dear brothers and sisters in Manhattan Chinese Christian Fellowship (MCCF), who are my closest family in Manhattan, and Christian Witness Center, Grace Baptist Church, Bridges International, Helping International Students (HIS), Faith E. Free Church, and Christian Challenge, for their love and prayers. Without them I would not have become the person I am today.

To all my friends and family who are a part of my life during my years in Kansas State University.

Last but not the least, to my dearest wife whom I share my life with, Dongxu Wang. Her unconditional love, patience, encouragement, and prayers are what always support me even during the most difficult time. She is the greatest blessing of my life. As Proverb 31:29 says, “Many daughters have done nobly, but you excel them all.”

Dedication

This dissertation is dedicated to Jesus Christ, the Lord our Savior,

"Great are the works of the Lord; They are studied by all who delight in them."

–Psalm 111:2

Chapter 1

Introduction

1.1 Background and motivation

1.1.1 Recent developments of nanoscience and technology

Significant advances in nano-science and technologies have enabled the design and synthesis of nanometer-sized structures with a tunable response to electromagnetic radiation [1–3]. Induced by the transient electric field of an incident laser pulse, this plasmonic response in metals is due to the electromagnetic field generated by the driven collective motion of conduction electrons (Fig. 1.1). Near the surface of sub-wavelength-size isolated nanoparticles [4–6] and nanostructured surfaces [7–13], the induced plasmonic electromagnetic field can strongly enhance an incident inducing field, and the plasmonic near-field intensity can exceed the incident external-field intensity by several orders of magnitude [1]. Extreme plasmonic light-intensity amplification of several orders of magnitudes is being applied in well-established surface-enhanced Raman spectroscopy, allowing the spectroscopic characterization of individual molecules [14]. This huge light amplification forms the physical basis for promising new discipline-transcending techniques, such as attosecond nanoplasmonic-field microscopy [7], light-harvesting [15], nanoplasmonically enhanced photocatalysis [16], and photothermal cancer therapy [17]. The continued unfolding of nanoplasmonic imaging techniques and nanoplasmonically-enhanced devices is supported by recent theoretical [5, 6, 18–

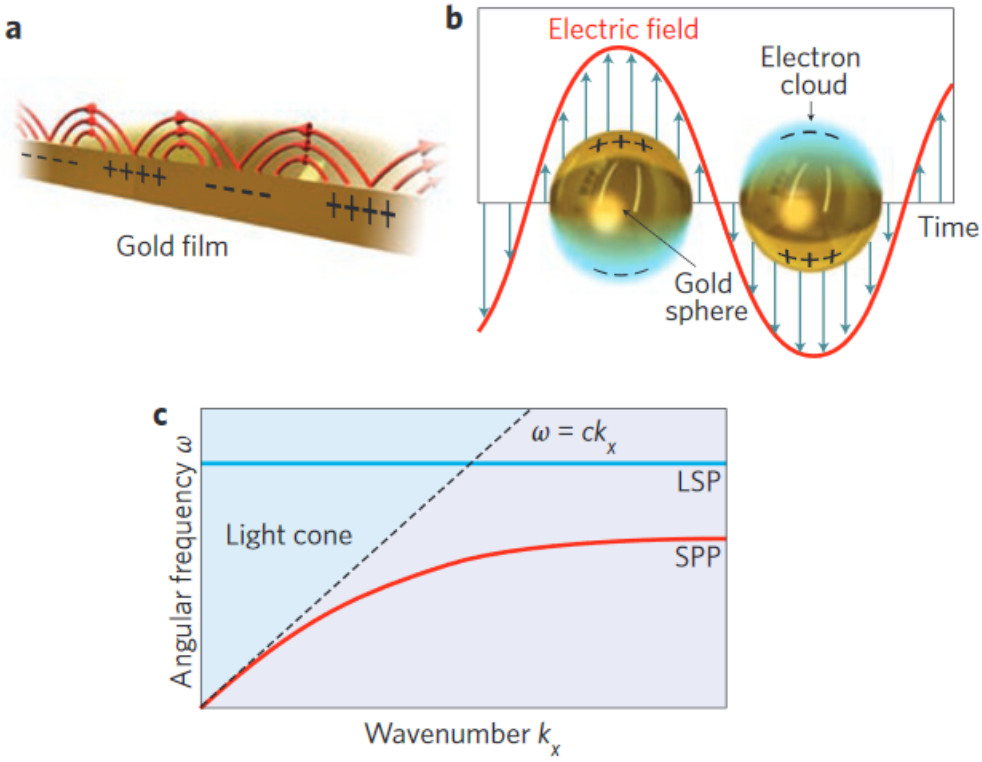


Figure 1.1: *Illustration of collective oscillation of electrons with the incident electromagnetic field at (a) a flat goldair interface (surface plasmon polariton, or SPP), and in (b) a gold nanoparticle (localized surface plasmon, or LSP). (c)Typical dispersion curves of SPPs (red) and LSPs (blue). (Figure from [23])*

21] and experimental [4, 22] efforts to help understand and detect induced plasmonic fields near nanostructures.

1.1.2 Recent developments of laser technology

The dynamical response of atoms, molecules, and solids to electromagnetic radiation is governed by electronic processes that occur at the timescale of one atomic time unit (24 attoseconds = 24 as = 24×10^{-18} s) [24]. Driven by rapid progress in the development of tabletop attosecond-duration light sources over the past two decades [3, 25–28], this timescale has become accessible in laboratories with the availability of intense ultrashort pulses of electromagnetic radiation in the infrared (IR) and extreme ultraviolet (XUV) spectral range with pulse durations of a few femtoseconds (1 fs = 10^{-15} s) and a few tens of

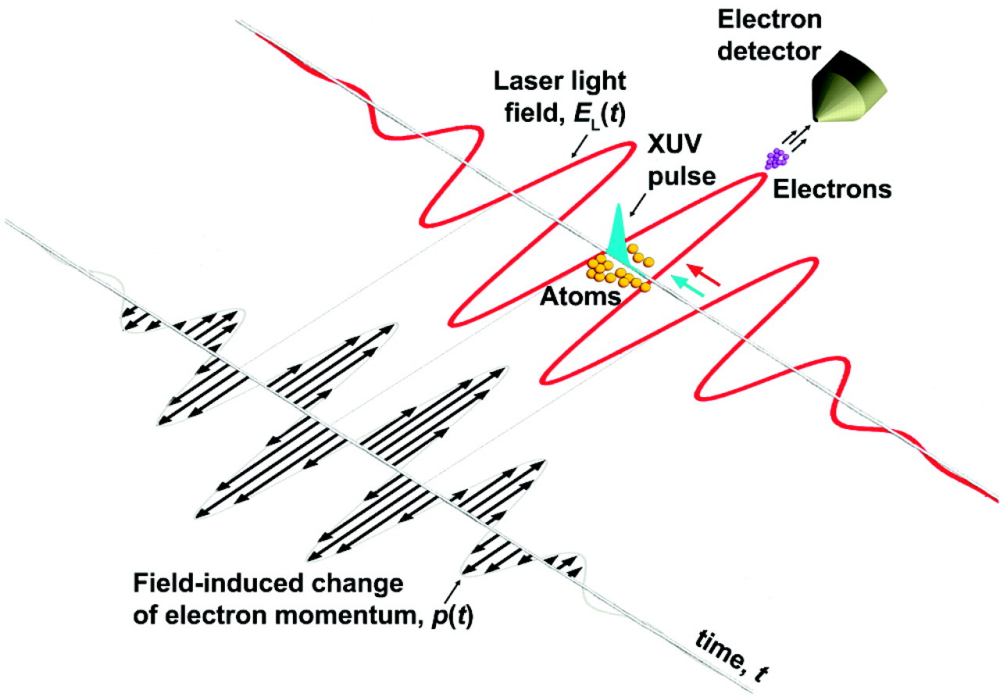


Figure 1.2: *Schematic of the attosecond streaking from atomic gas target. A few-cycle pulse of laser light, together with a synchronized sub-fs XUV burst, is focused into an atomic gas target. The XUV pulse knocks electrons free by photoionization. The light electric field* $\boldsymbol{E}_L(t)$ *to be measured imparts a momentum change to the electrons (black arrows), which scales as the instantaneous value of the vector potential* $\boldsymbol{A}_L(t)$ *at the instant of release of the probing electrons. The momentum change is measured by an electron detector, which collects the electrons ejected along the direction of the linearly polarized* $\boldsymbol{E}_L(t)$*. (Figure from [36])*

attoseconds, respectively. Pairs of such pulses can be synchronized, mutually delayed, and jointly focused on a target to allow the time-resolved investigation, such as nuclear motion in small molecules [29–31], electronic dynamics during the photoionization of atoms [32–35], the recording of streaked photoelectron spectra (Fig. 1.2) [33, 36–44] and two-photon-two-pathway-photoemission interferograms [27, 45]. As this technique is being further refined, emerging attosecond time-, spin-, energy-, and emission-angle-resolved photoelectron spectroscopy is starting to allow, e.g., the imaging of ultrafast bandstructure changes, dynamical screening effects in solids, and electronic correlation in magnetic materials [28, 46, 47].

1.2 Challenges of moving towards complex targets

1.2.1 Physical phenomena beyond atomic and molecular targets

Attosecond time-resolved photoemission spectroscopy, as mentioned previously, has been successfully demonstrated in experiments for gaseous atomic [32, 33, 48–52] and molecular [53–55] targets over the years. It is currently being extended to complex targets [26, 38], such as nanostructures and nanoparticles [6, 22, 43, 56–60], and solid surfaces [27, 28, 41, 44–46, 61–63], making it possible to examine, for example, the dynamics of photoemission from a surface on an absolute time scale [64] and suggesting, for example, the time-resolved observation of the collective motion of electrons (plasmon) in condensed-matter systems [65–67].

In contrast to time-resolved photoemission studies on isolated atoms in the gas phase, the experimental execution and theoretical analysis of time-resolved photoemission from nanotips [22, 68], solid surfaces, and nanoparticles in sub-optical-cycle time-resolved streaking [6, 38, 41, 69–71] and RABBITT (reconstruction of attosecond beating by interference of two-photon transitions) [45, 46, 72–74] experiments add challenges in preparing and characterizing clean and atomically flat solid surfaces and size- and shape-selected nanoparticles. Compared with photoemission from isolated gaseous atoms, the investigation of such experiments on complex targets requires, in addition, taking into consideration of (i) the complex electronic band structure [40, 46], (ii) elastic and inelastic scattering of released photoelectrons inside the solid [40, 70], (iii) the excitation of surface and bulk collective electronic excitations [65, 67, 75], (iv) the dielectric screening and reflection [27, 74] of the assisting IR-laser field at the solid surface, (v) the influence of equilibrating residual charge distributions on emitted photoelectrons [65], and (vi) the effect of spatially inhomogeneous plasmonic fields on the photoemission process [4–6, 19–21, 38].

1.2.2 Challenges in theoretical modeling

Correct theoretical modeling of those phenomena is especially crucial in order to understand the underlying physics. However, the existing theoretical models for investigating atomic and molecular targets fall short when moving towards complex targets. First, for example, while for atomic photoionization by visible and near UV light, the size of the target is small compared to the wavelength of the incident light pulse, this is no longer true for nanoparticles [6, 43, 56–60], (nanostructured) surfaces [40, 63, 71, 76], and layered structures [41, 42, 62, 63]. Not only the comparability of the wavelength and structure size, but also the target's spatially inhomogeneous dielectric response to the incident light pulse requires careful quantum-mechanical modeling beyond the dipole approximation [40, 71]. Second, most numerical models for streaked and interferometric photoemission from atoms are based on the so-called "strong-field approximation (SFA)" [38]. The SFA builds on the assumption that photo-emitted electrons are solely exposed to *spatially homogeneous* external fields. It discards all other interactions photo-released electrons may be subject to (e.g., with the residual parent ion) and cannot accommodate spatially inhomogeneous final-state interactions. While the SFA was shown to deteriorate for lower photoelectron energies [77], it completely loses its applicability for complex targets as screening and plasmonic effects expose photoelectrons to *inhomogeneous* net electromagnetic fields [38, 40, 65, 71]. The convenient use of analytically known so-called "Volkov wavefunctions" for the photoelectrons' motion in homogeneous electromagnetic fields [78] is no longer acceptable, since dielectric response effects entail screening length and induced plasmonic fields at the nm length scale [6, 56–60, 63, 65]. Thus, the numerical modeling of photoemission from complex targets with morphologies or plasmonic response lengths at the nm scale by intense short wavelength pulses (made increasingly available at new (X)FEL light sources [79]), necessitates photoemission models beyond the SFA.

1.3 Dissertation overview

The main focus of this dissertation is to theoretically investigate the photoemission process from plasmonic nanoparticles, particularly streaked photoemission and velocity map imaging, as well as improving the theoretical modeling of such investigations.

In Chapter 2, we present a theoretical model of simulating the IR-streaked XUV photoemission spectra, by calculating (a) the plasmonic field induced by IR pulses within Mie theory, and (b) the T-matrix elements for photoemission using a quantum-mechanical model. By implementing this model, we also demonstrate the applicability of streaking spectroscopy to the investigation of induced plasmonic effect near nanoparticles and nanostructured surfaces. This chapter lays the foundation for the following work.

In Chapter 3, based on the theoretical model in Chapter 2, we propose a scheme for the reconstruction of plasmonic near-fields at isolated nanoparticles from streaked photoelectron spectra. The success of this proposed scheme is demonstrated by the accurate imaging of the IR-streaking-pulse-induced plasmonic fields at the surface of gold nanospheres and nanoshells with sub-femtosecond temporal and sub-nanometer spatial resolution.

In Chapter 4, we further improve the theoretical model in Chapter 2, by developing a semi-classical approach, termed ACCTIVE, to solve the time-dependent Schrödinger's equation in spatially inhomogeneous electromagnetic fields, in order to obtain final-state wavefunctions with higher accuracy. We demonstrate the validation of this method by studying electron final-state wavefunctions in Coulomb and laser fields, before applying these improved final photoelectron states to streaked photoemission from hydrogen atoms and Au nanospheres. The results show excellent quantitative agreement with direct solution of the Schrödinger's equation. Implementing this method to simulating the streaked photoemission from Au nanospheres shows better agreement in plasmonic-field reconstruction for low energy photoelectrons than previous SFA simulations.

In Chapter 5, we further extend the linear-optical-response model of simulating the plasmonic field in Chapter 2, and explore the non-linear optical response of nanoparticles, which is observed in momentum imaging experiments at the Kansas State University Department

of Physics. Our simulations, by including the intensity-dependent index of refraction, show a significant non-linear effect in SiO_2-core-Au-shell nanoparticles in response to 10^{10} - 10^{12} W/cm^2 intensity and 780 nm central wavelength IR pulses. This effect is responsible for the change in the experimentally observed photoelectron "cut-off" energies, as a function of the external pulse intensity, suggesting the non-linear optical response to be a significant factor in strong-field photoemission from plasmonic nanoparticles.

Finally, in Chapter 6, we summarize this dissertation and present a brief outlook.

Atomic units are used throughout this dissertation unless otherwise indicated.

Chapter 2

Streaked photoemission from plasmonic nanoparticles

In this chapter, we developed a single-active-electron quantum-mechanical model to the calculation of streaked XUV-photoemission spectra from Au, Ag, and Cu nanospheres (Fig. 2.1) [6, 58]. We summarize our numerical model in Sec. 2.1, which is subdivided into four subsections. These describe our calculation of the plasmonic $\mathbf{E}_{plas}$ and total electric field $\mathbf{E}_{tot}$ induced by the incident (visible or IR) streaking pulse within classical electrodynamics (Sec. 2.1.1), our quantum-mechanical modeling of the photoemission amplitude from a given initial valence-band state of the nanoparticle (Sec. 2.1.2), an approximated analytical evaluation of the time-integration in our expression for the photoemission amplitude (Sec. 2.1.3), and our method for sampling over a large number of occupied initial states, required for the simulation of observable spectra (Sec. 2.1.4). In Sec. 2.2 we present our simulated streaked photoelectron spectra, starting with the discussion of the dependence of streaked spectra on the nanoparticle size and streaking-pulse wavelength in Sec. 2.2.1 and following with the comparison of results from our quantum-mechanical calculation with two independent classical simulations [19, 57] in Sec. 2.2.2. In Sec. 2.2.3 we compare examples for the accurate quantitative retrieval of plasmonic-field information, followed by our summary in Sec. 2.3.

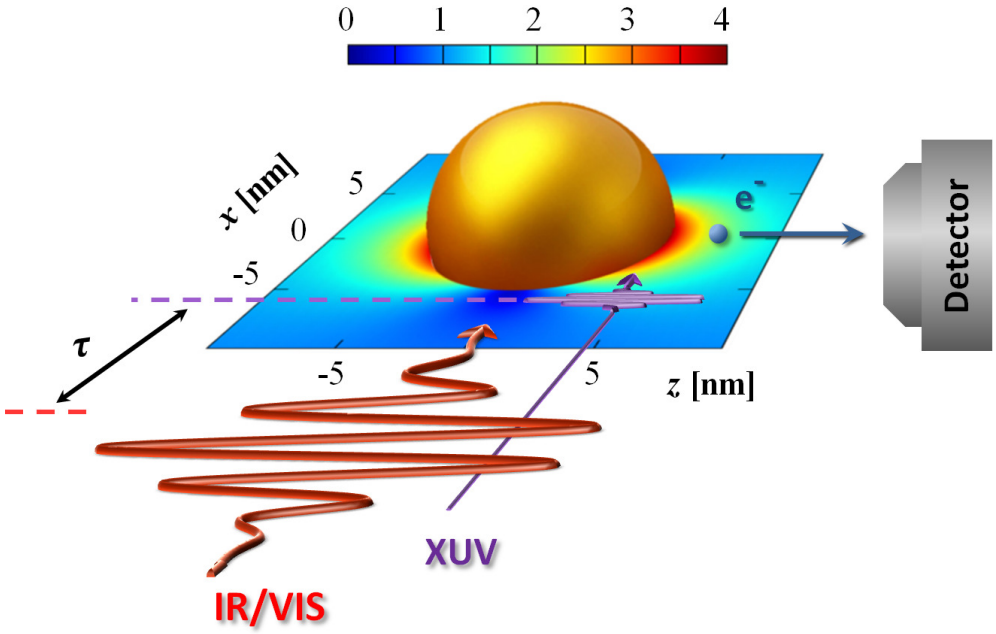


Figure 2.1: *Schematic of attosecond streaking from nanoparticles. A single ultrashort attosecond XUV pulse emits electrons into the field of a delayed IR or visible streaking laser pulse. The linear color/gray scale represents the maximal local electric-field-strength enhancement $\eta(\boldsymbol{r})$ [cf., Eq. (2.25)] in the $x-z$ plane for the example of 10 nm diameter Ag nanospheres exposed to 720 nm incident IR pulses with peak intensity $10^{12}\,W/cm^2$.*

2.1 Numerical model

In our single-active-electron model, we study photoemission from the conduction band of a metallic (Au, Ag, or Cu) nanospheres of diameter D by isolated XUV pulses into the electric field of a delayed IR or visible streaking pulse (Fig. 2.1). We assume both pulses to be incident along the positive x-axis and linearly polarized along the z-axis of our coordinate system, the origin of which coincides with the center of the nanosphere. We designate the center-to-center IR-to-XUV pulse delay time as τ, such that IR pulses precede the XUV pulses for positive values of τ, and arbitrarily define the time $t = 0$ as the instant when the center of the XUV pulse passes the center of the nanosphere. In compliance with laser and XUV pulse parameters in typical streaking experiments, we further assume that (i) the XUV pulse length τ_X is significantly shorter than an optical cycle of the streaking pulse, and (ii) the intensity of the streaking pulse is too small to induce photoemission from the target or to noticeably perturb the nanosphere's electronic structure, thus merely causing a delay-dependent shift of the photoelectron's final kinetic energy $\varepsilon_f(\tau)$ [38]. This energy shift is observable by streaked photoemission spectroscopy and carries information on the total electric field $\mathbf{E}_{tot}$ near the nanosphere surface. $\mathbf{E}_{tot}$ is given by the incident streaking field $\mathbf{E}_{inc}$ and the spatially inhomogeneous induced plasmonic field $\mathbf{E}_{plas}$.

2.1.1 Induced plasmonic response to the streaking field

For any given spectral component of the incident streaking pulse

$$\mathbf{E}_{inc}(\mathbf{r}, t; \omega) = \hat{\mathbf{z}} E_0(\omega)\ e^{i(kx-\omega t)}, \tag{2.1}$$

the corresponding spectral component of the total electric field,

$$\begin{aligned} \mathbf{E}_{tot}(\mathbf{r}, t; \omega) &= \mathbf{E}_{inc}(\mathbf{r}, t; \omega) + \mathbf{E}_{plas}(\mathbf{r}, t; \omega) \\ &= \mathbf{E}_{tot,0}(\mathbf{r}; \omega)\ e^{i\phi_{tot}(\mathbf{r};\omega)}\ e^{i(kx-\omega t)}, \end{aligned} \tag{2.2}$$

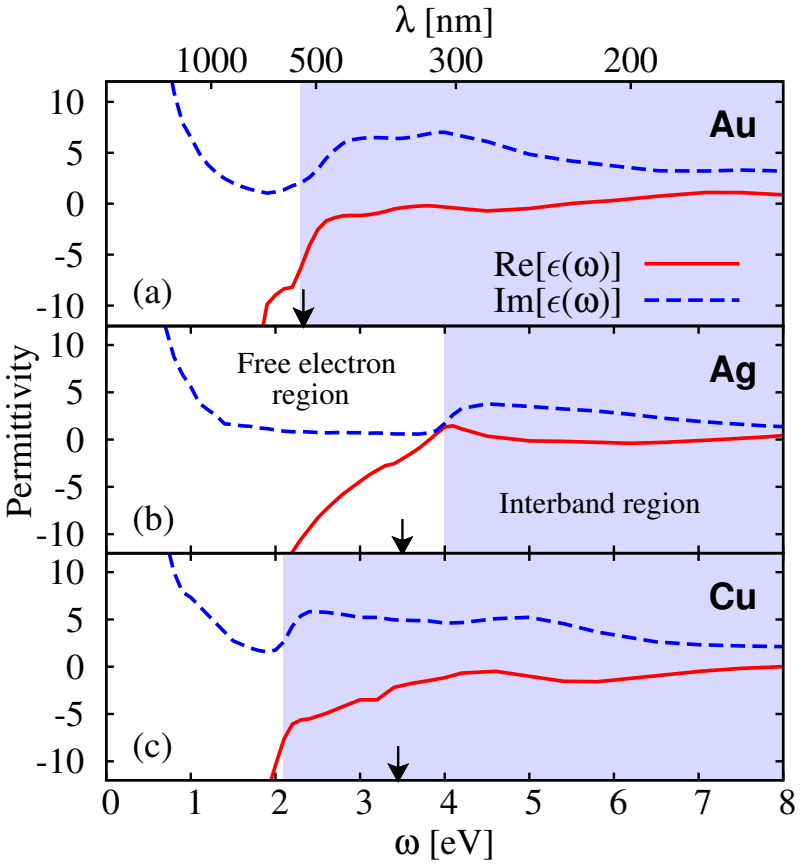


Figure 2.2: *Real and imaginary components of the complex permittivity $\epsilon(\omega)$ for Au, Ag, and Cu (adapted from Ref. [82]). The white and shaded areas indicate free-electron and interband-transition regions, respectively. Arrows point to the dipole surface-plasmon frequencies ω_D of sub-wavelength nanoparticles for each material.*

is obtained by solving Maxwell's equations. This is done by expressing both the incident and plasmonic field in terms of an infinite series expansion and by determining the expansion coefficients by applying the appropriate boundary conditions at large distances from the nanosphere and for the normal and tangential total electric-field components at the nanosphere surface following the work of Mie [80, 81]. The phase factor $\phi_{tot}(\mathbf{r};\omega)$ is defined so that the z-component of $\mathbf{E}_{tot,0}(\mathbf{r},t;\omega)$ is real. $\phi_{tot}(\mathbf{r};\omega)$ thus constitutes the spectral phase shift of the plasmonically enhanced incident streaking pulse relative to the incident plane-wave component $\mathbf{E}_{inc}(\mathbf{r},t;\omega)$.

The dielectric properties of the nanosphere materials are given by the complex permittivity $\epsilon(\omega) = \tilde{n}(\omega)^2$ or, alternatively, the complex index of refraction $\tilde{n}(\omega)$, for which we adopt

the experimental values for bulk Au, Ag, and Cu of Ref. [82]. Figures 2.2(a), 2.2(b), and 2.2(c) show the real and imaginary components of the permittivity for Au, Ag, and Cu, respectively. Two distinguishable frequency domains can be identified in these figures [83, 84]: the 'free-electron region' (white) at low frequencies and the 'interband region' (shaded) at higher frequencies. In the free-electron region, the incident field oscillates sufficiently slowly for conduction electrons to behave like free electrons as described by the Drude model [85]. In this domain, $\left|Re[\epsilon(\omega)]\right|$ and $\left|Im[\epsilon(\omega)]\right|$ decrease as the frequency of the incident field increases, followed by a strong increase of $Im[\epsilon(\omega)]$ near the threshold of interband transitions at frequency ω_I. The interband-transition-threshold frequencies (wavelengths) are approximately 2.3 eV (530 nm) for Au, 4.0 eV (310 nm) for Ag, and 2.1 eV (580 nm) for Cu. In the interband region, the loss function $-Im[\epsilon(\omega)]^{-1}$ tends to be large, indicating the likely loss of photon energy to interband excitations [83].

For sub-wavelength nanoparticles ($D << \lambda$) the quasi-static electric-field approximation applies. Within this approximation, the dipole surface plasmon frequency ω_D, i.e., the natural frequency of the induced collective electron oscillation, can be obtained at the maximal polarizability of the nanoparticle according to the Fröhlich condition [85]

$$Re[\epsilon(\omega_D)] = -2\epsilon_m, \tag{2.3}$$

where ϵ_m (=1) is the permittivity of the surrounding medium (vacuum in this study). The dipole surface plasmon frequencies ω_D = 2.3 eV (530 nm) for Au, 3.4 eV (360 nm) for Ag, and 3.3 eV (375 nm) for Cu are indicated as arrows in Figs. 2.2(a), 2.2(b), and 2.2(c), respectively. The resonant behavior of the polarizability at ω_D also depends on $Im[\epsilon(\omega)]$ and tends to be most pronounced for small or slowly varying $Im[\epsilon(\omega)]$ in the free-electron region. In contrast, the resonant polarization enhancement may be suppressed and hardly, if at all, recognizable if ω_D lies in the interband region: while the polarization enhancement in Ag is characterized by a pronounced resonance in the free-electron region at ω_D, for Cu ω_D - as determined based on the real part of $\epsilon(\omega)$ only according to Eq. (2.3) - lies in the interband region where interband excitations damp the surface-plasmon resonance and strongly red-

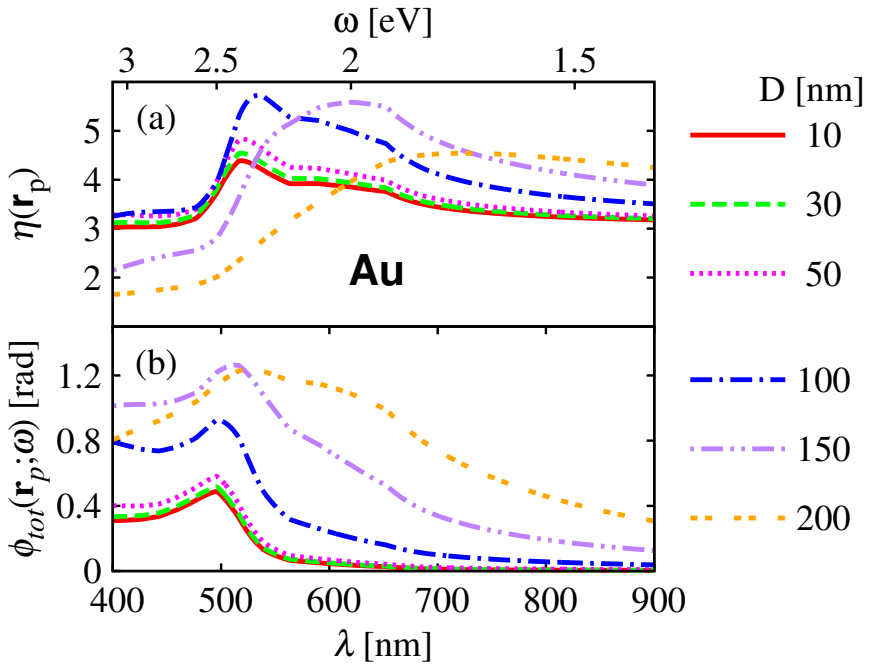


Figure 2.3: *(a) Plasmonic field enhancement $\eta(\boldsymbol{r}_p)$ and (b) phase shift $\phi_{tot}(\boldsymbol{r}_p;\omega)$ at the electric-field poles $\boldsymbol{r}_p$ on Au nanospheres with diameters D as a function of the incident plane wave's wavelength λ.*

shift ω_D to a broad resonance near ω_I. These profound differences in the dielectric response of Au, Ag, and Cu are reflected in the calculated electric-field enhancements discussed next.

The ratio of the total and incident electric-field intensity,

$$\eta(\mathbf{r}) = |\mathbf{E}_{tot,0}(\mathbf{r};\omega)|/E_0, \tag{2.4}$$

defines the plasmonic electric-field enhancement. By calculating the total electric field within Mie theory [80, 81], we find the largest electric-field enhancement $\eta(\mathbf{r}_p)$ at the electric-field 'poles' $[\mathbf{r}_p = (0, 0, z_p)]$ of the nanosphere along the IR and XUV polarization direction shown in Fig. 2.1. Figures 2.3(a), 2.4(a), and 2.5(a) show $\eta(\mathbf{r}_p)$ as a function of the incident pulse wavelength $\lambda = 2\pi/k = 2\pi c/\omega$ for 10 to 200 nm diameter Au, Ag, and Cu nanospheres, respectively, where c is the speed of light in vacuum.

For nanosphere diameters smaller or equal to $D = 100$ nm, Au displays a pronounced plasmon resonance at $\lambda = 530$ nm ($\omega = 2.3$ eV) [Fig. 2.3(a)]. In light of the preceding

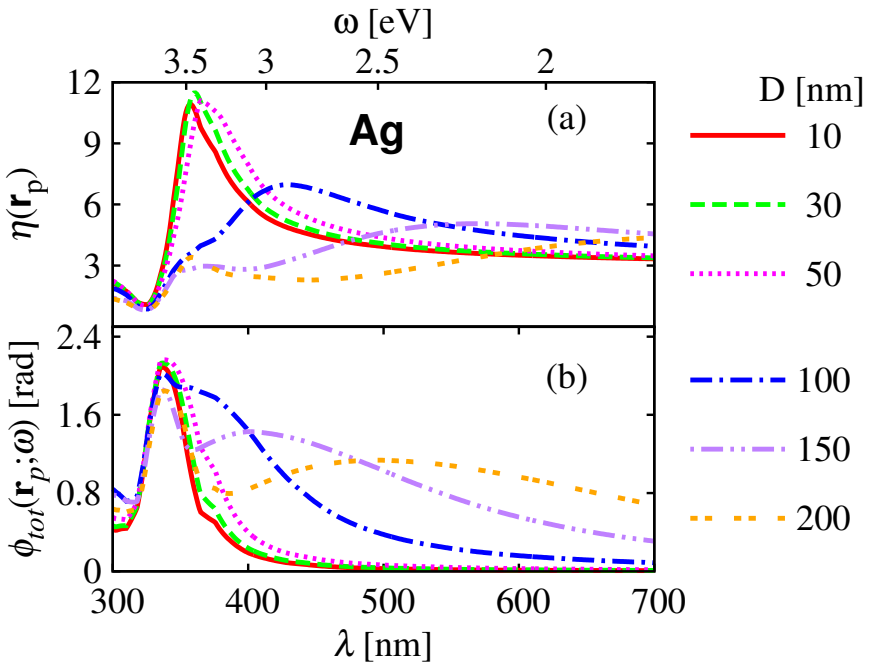


Figure 2.4: *Same as Fig. 2.3 for Ag nanospheres.*

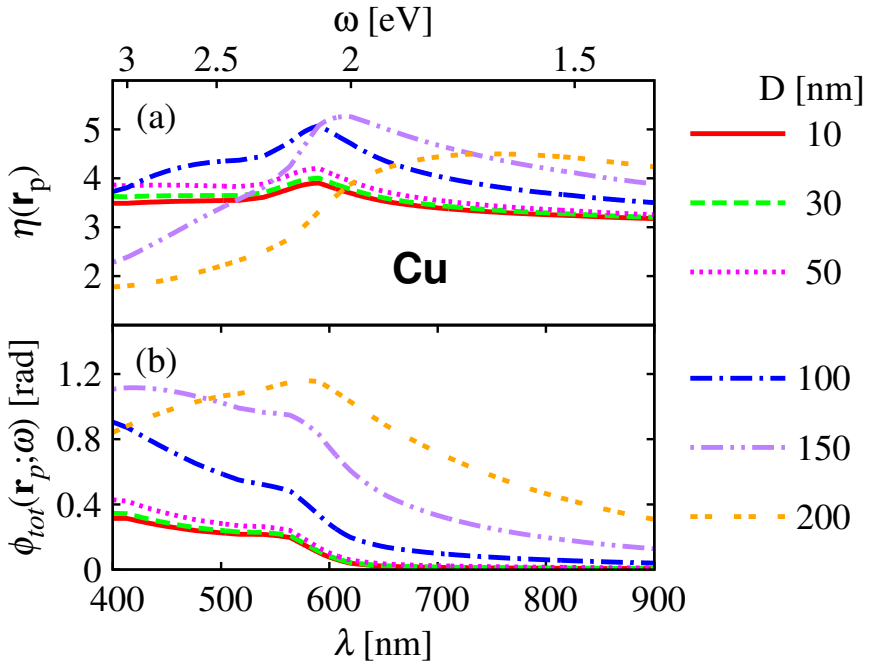


Figure 2.5: *Same as Fig. 2.3 for Cu nanospheres.*

discussion, this can be expected, since ω_D is just at the threshold for interband excitations ω_I. The largest enhancement factor of $\eta(\mathbf{r}_p) \approx 6$ is found for $D = 100$ nm. For Ag, on the other hand, $\omega_D = 3.4$ eV lies within the free-electron region and is well separated from ω_I [Fig. 2.4(a)]. Accordingly, Ag nanoparticles have a comparatively narrow (undamped) plasmon resonance near 360 nm (3.4 eV) with large amplitude enhancement. We find the largest enhancement $\eta(\mathbf{r}_p) \approx 6$ for $D = 30$ nm. Silver has the largest enhancement among the three transition metals compared in this work. For Cu, in sharp contrast to Ag, $\omega_D = 3.3$ eV lies deeply within the interband region. Consequently, the enhancement maximum for Cu nanospheres is strongly red-shifted from ω_D to the interband-transition threshold and appears as a very broad resonance profile in Fig. 2.5(a). The strongest enhancement $\eta(\mathbf{r}_p) \approx 5$ occurs near 580 nm (2.1 eV) for $D = 100$ nm.

For Au, Ag, and Cu nanopheres with diameters larger than $D = 100$ nm, the maximal-enhancement frequencies are strongly red-shifted and the enhancement maxima are smaller as compared to particles with $D < 100$ nm [Figs. 2.3(a), 2.4(a), and 2.5(a)]. This is due to the fact that as D approaches λ, the quasi-static approximation begins to fail, such that Eq. (2.3) is no longer valid. These large size-dependent red-shifts are accounted for by corrections to the Fröhlich condition Eq. (2.3) [85] and are confirmed by strongly red-shifted size-dependent absorption peaks in measured photoabsorption spectra [86]. These size-dependent redshifts are also in full compliance with the intuitively expected redshift of confinement resonances in quantum wells of increasing width [cf. Fig. 2 in Ref. [87]].

The local phase shift $\phi_{tot}(\mathbf{r}_p;\omega)$ at the poles $\mathbf{r}_p$ of the total electric field $\mathbf{E}_{tot}(\mathbf{r}_p,t;\omega)$ (2.2) relative to the incident field $\mathbf{E}_{inc}(\mathbf{r}_p,t;\omega)$ (2.1) is shown in Figs. 2.3(b), 2.4(b), and 2.5(b) for Au, Ag, and Cu nanospheres, respectively. For Au and Ag, the size- and material dependence of the plasmon resonance appears in $\phi_{tot}(\mathbf{r}_p;\omega)$ in the same fashion as in the field enhancement $\eta(\mathbf{r}_p)$, while for Cu the broad plasmon resonance visible in $\eta(\mathbf{r}_p)$ near $\lambda = 580$ nm in Fig. 2.5(a) translates into a more rapid decrease of $\phi_{tot}(\mathbf{r}_p;\omega)$ in Fig. 2.5(b). The maximal phase shifts in Figs. 2.3(b), 2.4(b), and 2.5(b) are $\phi_{tot}(\mathbf{r}_p;\omega) \approx 1.3$ rad for Au, 2.1 rad for Ag, and 1.2 rad for Cu. These phase shifts correspond to time delays of the wavefronts of the plasmonically enhanced spectral components Eq. (2.2) relative to the

plane waves Eq. (2.1) of 360 as for Au, 400 as for Ag, and 370 as for Cu. For $\lambda >> D$ the phase shift vanishes, as expected, since conduction electrons respond adiabatically to sufficiently slow external field oscillations.

The plasmonically enhanced streaking pulse is given by the superposition of its spectral components Eq. (2.2),

$$\mathbf{E}_{tot}(\mathbf{r},t) = \int d\omega\ \mathbf{E}_{tot,0}(\mathbf{r};\omega)\ e^{i\phi_{tot}(\mathbf{r};\omega)}\ e^{-i\omega t}. \tag{2.5}$$

In our numerical applications below, we consider incident streaking pulses

$$\mathbf{E}_{inc}(\mathbf{r},t) = \int d\omega\ \mathbf{E}_{inc}(\mathbf{r};\omega) \tag{2.6}$$

with Gaussian temporal profiles, 2.47 fs full width at half intensity maximum (FWHIM), corresponding to a spectral width of $\Gamma_{inc} = 0.73$ eV, and a peak intensity of 10^{12} W/cm^2.

2.1.2 Quantum-mechanical photoemission amplitude

In typical streaking experiments, electrons are emitted upon absorption of a single photon of the ionizing isolated XUV pulse [38]. We assume XUV pulses with a Gaussian temporal profile,

$$\mathbf{E}_X(\mathbf{r},t) = \hat{\mathbf{z}} E_X \exp\left[-2\ln 2\Big(\frac{t-t_x}{\tau_X}\Big)^2 \right] e^{-i\omega_X(t-t_x)}, \tag{2.7}$$

a central photon energy of $\omega_X = 105$ eV, and (unless specified otherwise) a pulse length (FWHIM) of $\tau_X = 200$ as, where $t_x = x/c$. We further may assume that the nanosphere is transparent to the XUV pulses, since $\tilde{n}(\omega_X) \approx 1$ at XUV frequencies [82]. Thus, the vector potential of the XUV pulse can be written in Coulomb gauge as

$$\mathbf{A}_X(\mathbf{r},t) = \int_t^\infty dt'\ \mathbf{E}_X(\mathbf{r},t'). \tag{2.8}$$

The quantum-mechanical transition amplitude for single-XUV-photon emission of an

electron from an initial state Ψ_i into the final state $\Psi^{\tau}_{\mathbf{k}_f}$ in the velocity gauge as a function of the final photoelectron momentum $\mathbf{k}_f$ and time delay τ is given by [6, 58, 88],

$$T_i(\mathbf{k}_f, \tau) = i \int dt \int d\mathbf{r} \Psi^{\tau *}_{\mathbf{k}_f}(\mathbf{r}, t) \mathbf{A}_X(\mathbf{r}, t) \cdot \hat{\mathbf{p}} \Psi_i(\mathbf{r}, t), \tag{2.9}$$

where $\hat{\mathbf{p}} = -i\nabla$ is the electron momentum operator. We model initial conduction-band states,

$$\Psi_i(\mathbf{r}, t) = \Psi_i(\mathbf{r}) e^{-i\omega_i t}, \tag{2.10}$$

as bound states of a spherical square well of radius $D/2$ and set the depth of the spherical square-well potential equal to the sum of the work function and conduction-band width. The work function and conduction-band width used in our numerical simulations for Au, Ag, and Cu are listed in Tab. 2.1.2.

We represent the final continuum state as the exponentially damped 'Volkov' continuum wave function [6, 58]

$$\Psi^{\tau}_{\mathbf{k}_f}(\mathbf{r}, t) = \frac{1}{\sqrt{2\pi}} f[l(\mathbf{r}); \lambda_i)] e^{i\mathbf{k}_f \cdot \mathbf{r}} e^{i\phi^{\tau}_{\mathbf{k}_f}(\mathbf{r}, t)} \tag{2.11}$$

with the position-dependent generalized Volkov phase

$$\phi^{\tau}_{\mathbf{k}_f}(\mathbf{r}, t) = \int_t^{\infty} dt' \mathbf{p}^2(\mathbf{r}, t'; \tau)/2. \tag{2.12}$$

The damping factor $f(l; \kappa) = exp[-l/(2\kappa)]$ accounts for inelastic scattering of the photoelectron inside the nanoparticle after being excited ('born') by the XUV pulse at position $\mathbf{r}$. Due to scattering, photoelectrons born inside the nanosphere are less likely to be registered by the detector (Fig. 2.1). In addition to the inelastic mean free path (MFP) κ, the damping factor depends on the path length $l(\mathbf{r})$ of photoelectrons inside the nanosphere. κ changes by about 2% for the energy range and pulse parameters and for each of the three transition metals considered in this work. We can therefore neglect its dependence on the photoelectron kinetic energy and consider it as constant. The MFPs used for our numerical simulations are listed in Tab. 2.1.2. We calculate the path length $l(\mathbf{r})$ numerically, based on

classical photoelectron trajectories $\tilde{\mathbf{r}}_\tau(t')$ for each given XUV-IR time delay τ, with initial positions $\tilde{\mathbf{r}}_\tau(t) = \mathbf{r}$ at time t and initial momenta

$$\mathbf{p}(\mathbf{r}, t; \tau) = \mathbf{k}_f + \int_t^\infty dt' \, \mathbf{E}_{tot}[\tilde{\mathbf{r}}_\tau(t'), t' + \tau]. \tag{2.13}$$

Table 2.1: *Workfunctions, conduction-band widths, and mean-free-paths (MFP) for Au, Ag, and Cu.*

	Work function [eV]	Bandwidth [eV]	MFP [Å]
Au	5.1 [89]	8 [90]	4.4 [91]
Ag	4.5 [89]	8 [90]	4.9 [91]
Cu	4.7 [89]	6 [92]	5.1 [91]

2.1.3 Evaluation of the photoemission amplitude

The central energy of the XUV pulses (2.7) assumed in this work (105 eV) corresponds to an optical period of 39.39 as. This period being significantly shorter than the XUV-pulse duration ($\tau_X = 200$ as) allows the representation of the XUV-pulse vector potential (2.8) in slowly-varying-amplitude approximation as the Gaussian pulse

$$\begin{aligned} \mathbf{A}_X(\mathbf{r}, t) &= \int_t^\infty dt' \, \mathbf{E}_X(\mathbf{r}, t') \\ &\approx -\hat{\mathbf{z}} \frac{i E_X}{\omega_X} \exp\left[-2 \ln 2 \Big(\frac{t - t_x}{\tau_X} \Big)^2 \right] e^{-i\omega_X (t - t_x)}. \end{aligned} \tag{2.14}$$

Thus, even though the time integral in Eq. (2.9) extends over the entire real axis, noticeable contributions to it only arise near the center of the XUV pulse at $t = t_X$.

The visible and IR streaking pulses we consider have wavelengths between 350 and 800 nm. Their corresponding optical cycles lie between 1.06 and 2.66 fs and are significantly longer than the XUV pulse duration. Compared to the envelope of the XUV pulse, the temporal variation of the streaking field and generalized Volkov phase (2.12) is thus very slow. Consistent with the remark following Eq. (2.14), we therefore Taylor expand Eq. (2.12)

as a function of time about t_x,

$$\phi^{\tau}_{\mathbf{k}_f}(\mathbf{r},t) = \phi^{\tau}_{\mathbf{k}_f}(\mathbf{r},t_x) + \phi^{\tau}_{\mathbf{k}_f}{}'(\mathbf{r},t_x)(t-t_x) + \frac{1}{2}\phi^{\tau}_{\mathbf{k}_f}{}''(\mathbf{r},t_x)(t-t_x)^2 + O\big((t-t_x)^3\big), \tag{2.15}$$

where the primes refer to time derivatives. Equation (2.9) then becomes

$$T_i(\mathbf{k}_f,\tau) = -\frac{iE_X}{\omega_X}\hat{\mathbf{z}}\cdot\int d^3\mathbf{r}\,\Big[\nabla\Psi_i(\mathbf{r})\Big]\,\Psi^{\tau *}_{\mathbf{k}_f}(\mathbf{r},t_x)e^{-i\omega_i t_x} \times \int dt\;\exp\left[-\Big(\frac{2\ln 2}{\tau_X^2}+\frac{i}{2}\phi^{\tau}_{\mathbf{k}_f}{}''(\mathbf{r},t_x)\Big)(t-t_x)^2\right] \times e^{-i\left(\phi^{\tau}_{\mathbf{k}_f}{}'(\mathbf{r},t_x)+\omega_X+\omega_i\right)(t-t_x))}. \tag{2.16}$$

The time integral now represents the Fourier transformation of a Gaussian function and can be performed analytically with the result

$$T_i(\mathbf{k}_f,\tau) = \frac{\sqrt{\pi}E_X}{i\omega_X}\hat{\mathbf{z}}\cdot\int d^3\mathbf{r}\,\Big[\nabla\Psi_i(\mathbf{r})\Big]\,\Psi^{\tau *}_{\mathbf{k}_f}(\mathbf{r},t_x)e^{-i\omega_i t_x} \times \frac{1}{b^{\tau}_{\mathbf{k}_f}(\mathbf{r})}\exp\left[-\left(\frac{\phi^{\tau *}_{\mathbf{k}_f}{}'(\mathbf{r},t_x)+\omega_X+\omega_i}{2b^{\tau}_{\mathbf{k}_f}(\mathbf{r})}\right)^2\right], \tag{2.17}$$

where

$$b^{\tau}_{\mathbf{k}_f}(\mathbf{r}) = \sqrt{\frac{2\ln 2}{\tau_X^2}+\frac{i}{2}\phi^{\tau *}_{\mathbf{k}_f}{}''(\mathbf{r},t_x)}. \tag{2.18}$$

We perform the three remaining integrations in Eq. (2.17) numerically. In numerical tests we confirmed that the approximation Eq. (2.16) to the amplitude Eq. (2.9) does not induce noticeable changes in any of the numerical results shown and discussed in Sec. 2.2 below.

2.1.4 Summation over initial states

Equation (2.17) gives the transition amplitude for photoemission out of a particular initial state Ψ_i. Allowing for photoelectron emission from any occupied conduction-band state,

we incoherently add contributions to the total photoelectron yield from initial states with energies ε_i at and below the Fermi energy,

$$P(E_f,\tau) = \sum_{i\in occ} |T_i(\mathbf{k}_f,\tau)|^2. \tag{2.19}$$

Electronic confinement in nm-size objects results in a very large number of energetically very narrowly spaced initial conduction-band states. For example, a D=10 nm Au nanosphere, the smallest diameter considered in our numerical applications below, contains 26,551 bound states with maximal angular-momentum quantum number $l_{max} = 65$ below the Fermi level, and this number increases with the size of the nanosphere. We therefore carried out the summation in Eq. (2.19) by dividing the conduction band into m equal segments, $S_j = 1, ...m$, each segment having $n(j)$ occupied states. Equation (2.19) can then be rewritten as

$$\begin{aligned} P(E_f,\tau) &= \sum_{j=1}^{m} n(j) \times \left[\frac{1}{n(j)} \sum_{i\in S_j} |T_i(\mathbf{k}_f,\tau)|^2\right] \\ &= \sum_{j=1}^{m} n(j) \times P_j(E_f,\tau), \end{aligned} \tag{2.20}$$

where $P_j(E_f,\tau)$ is the average yield in segment S_j.

For numerical efficiency, we evaluated Eq. (2.20) approximately by replacing $P_j(E_f,\tau)$ with the averaged yield in segment S_j,

$$P_j^{ave}(E_f,\tau) = \frac{1}{q} \sum_{i=1}^{q} |T_{[N(i)*n(j)]}(\mathbf{k}_f,\tau)|^2. \tag{2.21}$$

We obtained $P_j^{ave}(E_f,\tau)$ by calculating the transition amplitude for q randomly sampled occupied states in S_j, with the sampling function $N(i)$ returning uniformly distributed random numbers in the interval $[0, 1]$. For $m = 10$ and $q = 10$ and all numerical examples discussed in this work, we found Eq. (2.21) to approximate the photoemission yields Eq. (2.19) with a relative error below 5%.

2.2 Streaked photoelectron spectra

In this section, we discuss our simulated streaked photoelectron spectra for Au, Ag, and Cu nanospheres with diameters of 10 and 50 nm. For each material, we consider two streaking-pulse wavelengths of 720 nm and the respective plasmonic-enhancement-resonance wavelength (530 nm for Au, 360 nm for Ag, and 580 nm for Cu).

2.2.1 Size and streaking-wavelength dependence

Figures 2.6 - 2.8 show our numerical results for streaked photoemission spectra from Au, Ag, and Cu nanospheres, respectively. The streaking traces oscillate with amplitudes $\delta\varepsilon_f(D,\lambda)$ due to the XUV-IR-pulse-delay-dependent energy shift imposed by the total electric field $\mathbf{E}_{tot}$ (2.5) on the emitted electron. Their delay-dependence thus resembles the temporal profile of $\mathbf{E}_{tot}$ as explained above, relative to which they are phase shifted. $\delta\varepsilon_f(D,\lambda)$ varies with the size of the nanosphere and the center wavelength of the streaking pulse. Independent of the transition metal investigated, $\delta\varepsilon_f(D,\lambda)$ increases with the size of the nanosphere for a given streaking-pulse wavelength, consistent with and proportional to the respective size-dependent plasmonic enhancements shown in Figs. 2.3(a), 2.4(a), and 2.5(a).

With regard to the streaking-pulse-wavelength dependence, $\delta\varepsilon_f(D,\lambda)$ remains approximately the same for 720 and 530 nm Au nanospheres of a given diameter, as the comparison of Fig. 2.6(a) with Fig. 2.6(b) and of Fig. 2.6(c) with Fig. 2.6(d) demonstrates. This wavelength-independence of the streaking amplitude disagrees with a well-known common feature of streaked photoelectron spectra from gaseous atomic targets [38], for which the streaking-oscillation amplitude,

$$\delta\varepsilon_f(D,\lambda) \sim \lambda E_0, \tag{2.22}$$

is proportional to the incident wavelength and incident streaking field amplitude, resulting in larger oscillation amplitudes for larger wavelength. The approximate λ-independence of $\delta\varepsilon_f(D,\lambda)$ for Au nanospheres is due to the cancelation of two effects: while the λ-dependence in Eq. (2.22) carries over from gaseous atoms to nanospheres, the incident-streaking-pulse

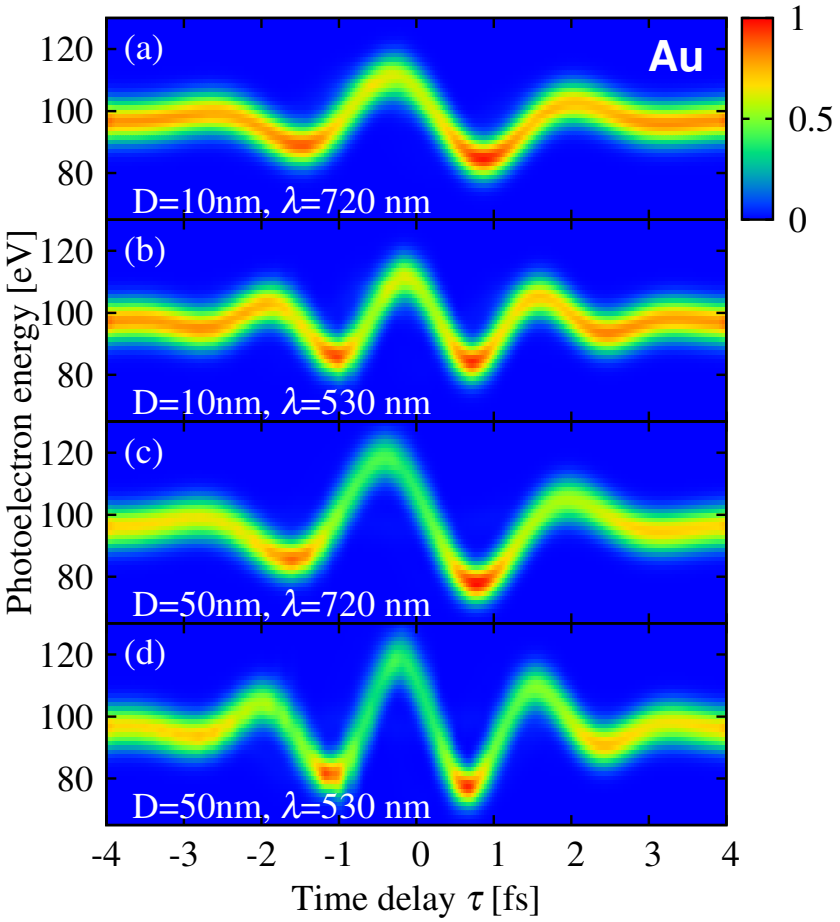


Figure 2.6: *Quantum-mechanically calculated streaked XUV photoemission spectra for 10 and 50 nm diameter Au nanospheres and streaking-field wavelengths of 720 and 530 nm. The linear color/gray scale gives the photoemission yield separately normalized to the maximal yields in (a)-(d).*

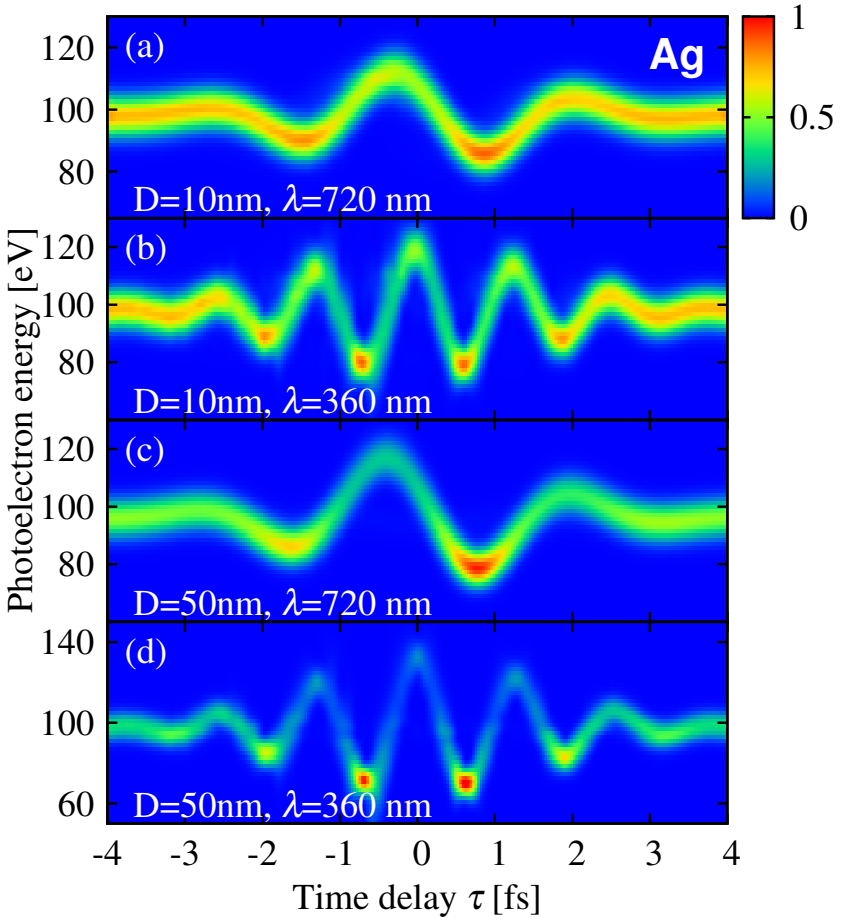


Figure 2.7: *Same as Fig. 2.6 for Ag nanospheres and streaking-field wavelengths of 720 and 360 nm.*

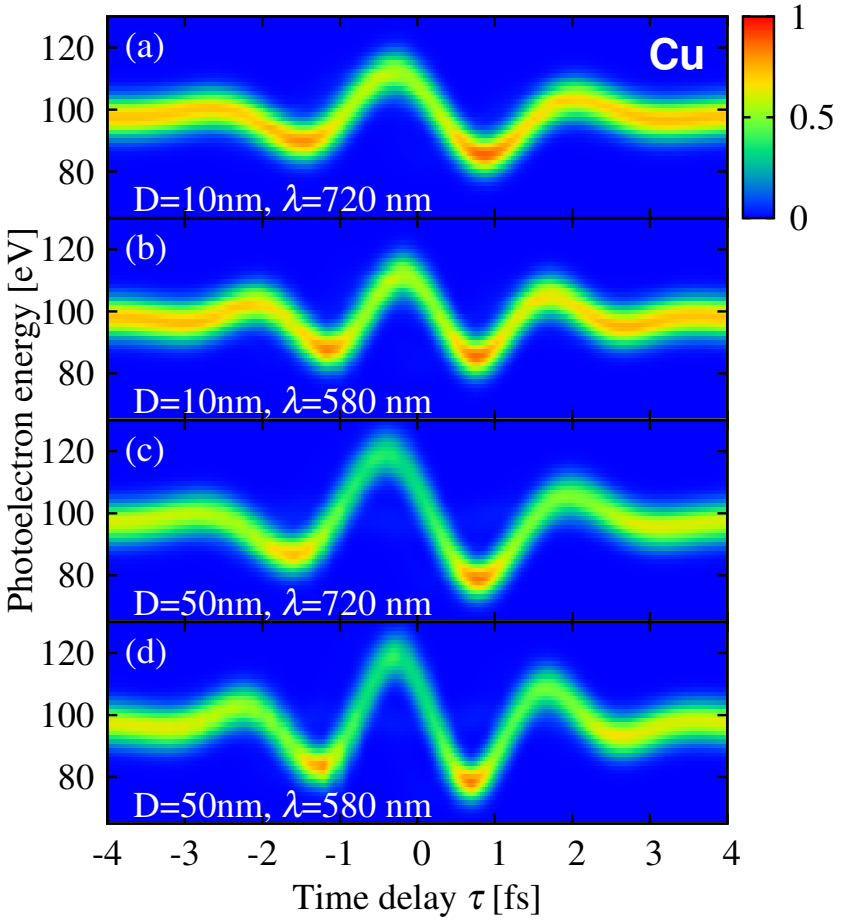


Figure 2.8: *Same as Fig. 2.6 for Cu nanospheres and streaking-field wavelengths of 720 and 580 nm.*

amplitude E_0 needs to be replaced by the amplitude of the plasmonically enhanced streaking field (2.5) at the nanoparticle surface,

$$\delta\varepsilon_f(D,\lambda) \sim \lambda|\mathbf{E}_{tot,0}|. \tag{2.23}$$

According to Fig. 2.6, the plasmonic-field enhancement at 720 nm is weaker than for 530 nm (Fig. 2.3) and (accidentally) happens to balance the increase of $\delta\varepsilon_f(D,\lambda)$ with λ found for gaseous atomic targets. The degree of sensitivity of the streaking-trace amplitude to the nanoparticle size is thus indicative for plasmonic-field enhancement at the nanoparticle surface.

We find the same approximate independence of the streaking amplitude on the streaking wavelength for 10 and 50 nm Cu nanospheres (Fig. 2.8). For a given diameter, Cu nanospheres reveal approximately the same streaking-oscillation amplitude $\delta\varepsilon_f(D,\lambda)$ as Au nanospheres, both on resonance (580 nm) and off-resonance (720 nm). In contrast, the apparent streaking amplitude for 10 and 50 nm Ag nanospheres is noticeably larger near the plasmon-resonance wavelength (360 nm) than off-resonance at 720 nm (Fig. 2.7). The less-then-perfect cancelation of the λ dependence of the two factors in Eq. (2.23) for Ag nanospheres is an expression of the (i) polarizability of Ag being much larger than the polarizability of Au and Cu and (ii) strong material dependence of the streaking amplitude.

Figures 2.6 - 2.8 show a pronounced difference in photoemission yield for different photoelectron energies. This energy-dependence of photoemission yield is due to the photoemission cross section $\sigma(\epsilon_f)$, which strongly emphasizes the yield at lower energies,as shown in Fig. 2.9(e). The difference in photoemission yield increases with the energy span of the streaked photoelectron spectra, thus directly depends to the streaking amplitude, and indirectly depends on the incident wavelength, the size, and the material of nanospheres, as discussed above.

2.2.2 Comparison with classical calculations

In Fig. 2.9 we compare streaked photoelectron spectra for 10 nm diameter Au nanospheres and 720 nm streaking-field wavelength, resulting from independently performed classical-trajectory Monte-Carlo simulations of Süßmann and Kling [19] and Saydanzad *et al.* [57], with our quantum-mechanical simulation. For this comparison only, we changed the XUV-pulse length from 200 to 287 as, in order to employ the same XUV parameters as in the two classical calculations. The classical spectra in Figs. 2.9(b) and 2.9(c) are calculated for the same streaking and XUV parameters used in our numerical model [Fig. 2.9(a)]. At a first glance, the classical and quantum-mechanical results in Figs. 2.9(a-c) appear to be in good agreement, however, examination of their centers of energy (CoE) reveals three noticeable differences:

First, the CoE in the classical simulation by Süßmann and Kling lies approximately 4 eV higher than in the two other calculations. This is a result of the classical model in Ref. [19] being restricted to photoemission from the Fermi level only, while both our quantum-mechanical model and the classical model in Ref. [57] allow for photoemission from all occupied conduction-band states.

Second, the energy-dependence of the photoemission-yield as a function of the XUV-IR-pulse delay is different for all three simulations. Consistent with the photoelectron-energy-dependence of the quantum-mechanically calculated XUV-photoemission cross section $\sigma(\varepsilon_f)$ [88] shown in Fig. 2.9(e), the energy dependence of the quantum-mechanical streaking spectrum in Fig. 2.9(a) strongly emphasizes photoemission at lower energies. This effect is absent in both classically calculated spectra.

Third, streaking amplitudes and streaking phases predicted by all three calculations are noticeably different, as shown for the CoE of all spectra in Fig. 2.9(d). The quantum-mechanical model predicts the largest and the classical model in Ref. [19] the smallest oscillation amplitude. The difference between the two classical calculations appears to be due to different model assumptions. While the classical calculations of Saydanzad *et al.* [57] allow for photoelectron release from inside the nanoparticle with a dipolar angular distribution

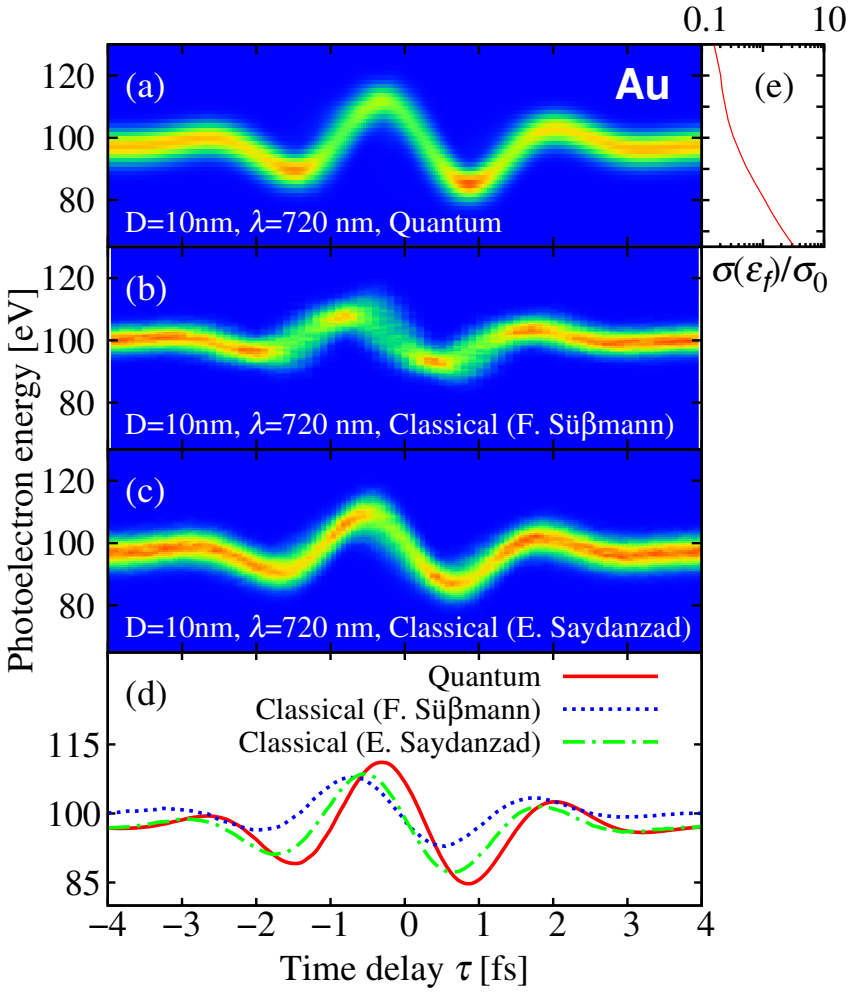


Figure 2.9: *Calculated streaked XUV photoemission spectra for 10 nm diameter Au nanospheres and streaking-field wavelengths of 720 nm according to (a) our quantum-mechanical model, (b) the classical model of Süßmann and Kling (adapted from Ref. [19]), and (c) the classical model of Saydanzad* et al. *(adapted from Ref. [57]). The linear color/gray scale gives the photoemission yield normalized to the maximal yield for each plot. (d) Centers of energy of the spectra in (a)-(c). (e) XUV-photoionization cross section $\sigma(\varepsilon_f)$, normalized at $\sigma_0 = \sigma(80\ eV)$.*

and include electron scattering of released photoelectrons inside the nanosphere, the classical model of Ref. [19] restricts conduction-band-electron release to the surface, does not allow for scattering of photo-released electrons inside the nanoparticle, and assumes photoemission probabilities that do not depend on the emission location on the sphere. To some extent the differences in the classical and quantum mechanical CoE streaking amplitudes and phases are due to fundamental dissimilarities of classical and quantum-mechanical dynamics, such as the inclusion/absence of coherence in quantum/classical calculations.

2.2.3 Plasmonic-field-information retrieval

In order to investigate the extent to which plasmonic field information is imaged in streaked photoelectron spectra, we calculated streaked spectra with and without including the induced plasmonic field $\mathbf{E}_{plas}(\mathbf{r}, t)$ in Eq. (2.2), while leaving all nanosphere, XUV-, and IR-pulse parameters unchanged. The CoE of these spectra for 10 nm Au, Ag, and Cu nanospheres and various wavelengths are shown in Fig. 2.10. They reveal a significant increase and phase shift of the streaking amplitude due to the induced plasmonic field.

In order to retrieve the plasmonic-field enhancement and phase shift, we fit our numerically calculated CoE to a sinusoidal function with Gaussian envelope,

$$\varepsilon(\tau) = \varepsilon_0 + A \exp\left[-2 \ln 2 \left(\frac{\tau}{\sigma}\right)^2 \right] \cos(\omega\tau + \phi), \tag{2.24}$$

and adjust the values of $\varepsilon_0, A, \sigma, \omega, \phi$. To quantify the effects of the plasmonic-field enhancement on streaked spectra, we introduce the *wave-length-resolved* (spectral) streaking-oscillation-amplitude-enhancement factor

$$\eta_{streak}(\lambda) = \left. \frac{A_w}{A_{w/o}} \right|_{\lambda}, \tag{2.25}$$

where A_w and $A_{w/o}$ are the oscillation amplitudes adjusted according to Eq. (2.24) with and without including the induced plasmonic field, respectively. We further define the spectral

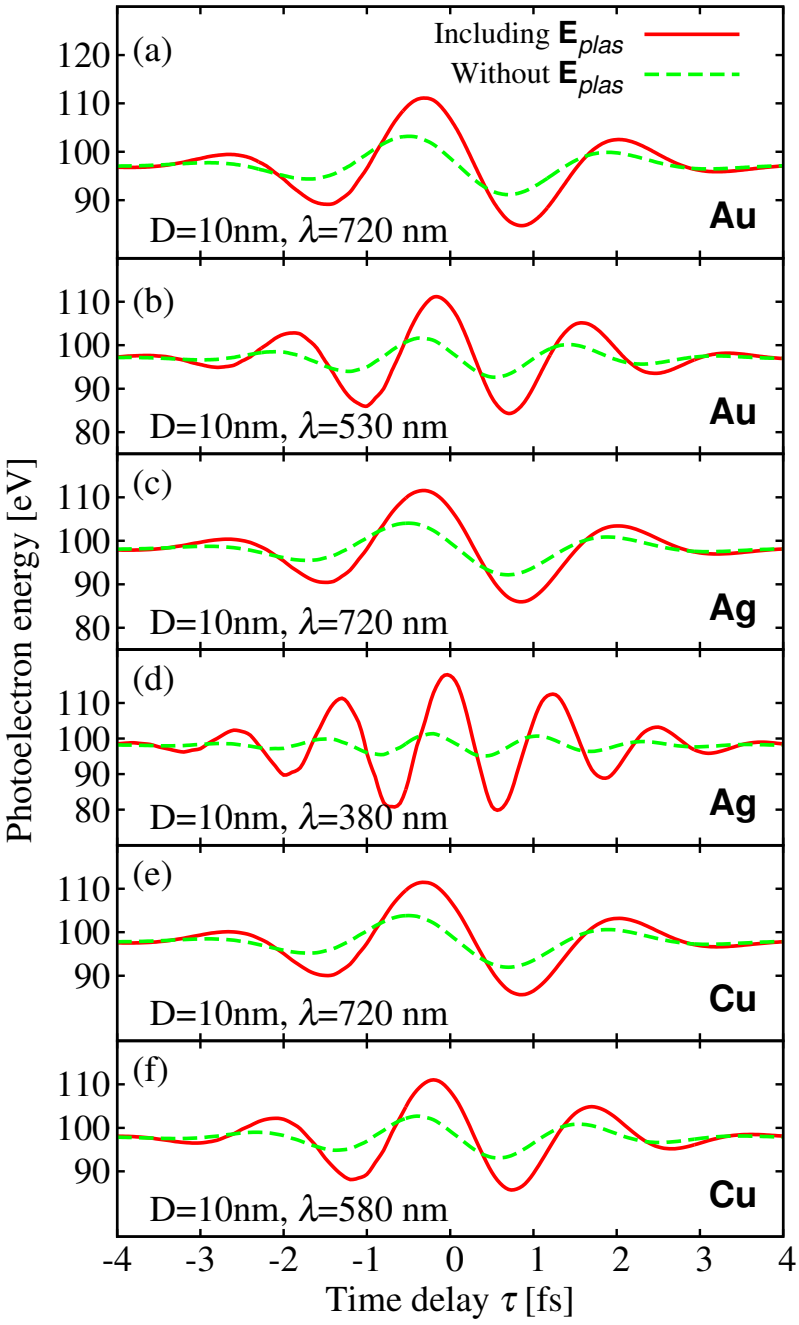


Figure 2.10: *Centers-of-energy of streaked XUV photoemission spectra for 10 nm diameter (a),(b) Au, (c),(d) Ag, and (e),(f) Cu nanospheres, including (red solid line) and excluding (green dashed line) the induced plasmonic field* $\boldsymbol{E}_{plas}$ *in Eq. (2.2).*

phase-shift difference

$$\Delta\phi_{streak}(\lambda) = \left(\phi_w - \phi_{w/o}\right)\Big|_{\lambda}, \tag{2.26}$$

where ϕ_w and $\phi_{w/o}$ are the phases in Eq. (2.24), adjusted with and without including the induced plasmonic field, respectively.

Figures 2.11(a), 2.12(a), and 2.13(a) show the retrieval of the plasmonic field enhancement η defined in Eq. (2.4) and plotted in Fig. 2.3(a), 2.4(a), and 2.5(a), respectively, as a function of the streaking-pulse wavelength λ for 10 nm diameter Au, Ag, and Cu nanospheres, respectively. The solid red lines show the electric field-strength enhancement $\eta(\mathbf{r}_p)$ obtained using Mie theory at the poles $\mathbf{r}_p$ of the nanospheres. The dashed red lines show the field-strength enhancement $\overline{\eta(\mathbf{r})}$, averaged over the nanosphere surface with the weight factor $|\cos\theta|^2$, approximating the relative contributions of photoelectrons emitted at different angles as dipolar. The blue markers show the streaking-oscillation-amplitude enhancement η_{streak} we retrieved from our calculated spectra by using Eqs. (2.24) and (2.25). The retrieved streaking-oscillation amplitude enhancement is in good agreement with the averaged plasmonic field-strength enhancement $\overline{\eta(\mathbf{r})}$. It not only (i) correctly reproduces the shape of the field-enhancement factor for each element as a function of streaking-pulse wavelength, (ii) matches the enhancement maxima at 530 nm for Au, 360 nm for Ag, and 580 nm for Cu, but also (iii) quantitatively reproduces the numerical value of the averaged enhancement $\overline{\eta(\mathbf{r})}$. Ag nanospheres yields the highest averaged amplitude enhancement $\overline{\eta(\mathbf{r})} \approx 8$, while for Au and Cu nanospheres we find $\overline{\eta(\mathbf{r})} \approx 3$.

Figures 2.11(b), 2.12(b), and 2.13(b) show the retrieval of the plasmonic phase shifts as a function of the streaking-pulse wavelength for 10 nm diameter Au, Ag, and Cu nanosphere, respectively. The red solid lines show the relative plasmonic phase shift

$$\varphi_{Mie}(\lambda) = \phi_{tot}(\mathbf{r}_p)\big|_{\lambda} - \phi_{tot}(\mathbf{r}_p)\big|_{720\ \mathrm{nm}}, \tag{2.27}$$

obtained using Mie theory at the nanosphere poles $\mathbf{r}_p$ and defined as the phase shift caused by the induced plasmonic field for a central streaking-field wavelength λ, $\phi_{tot}(\mathbf{r}_p)\big|_{\lambda}$, relative to

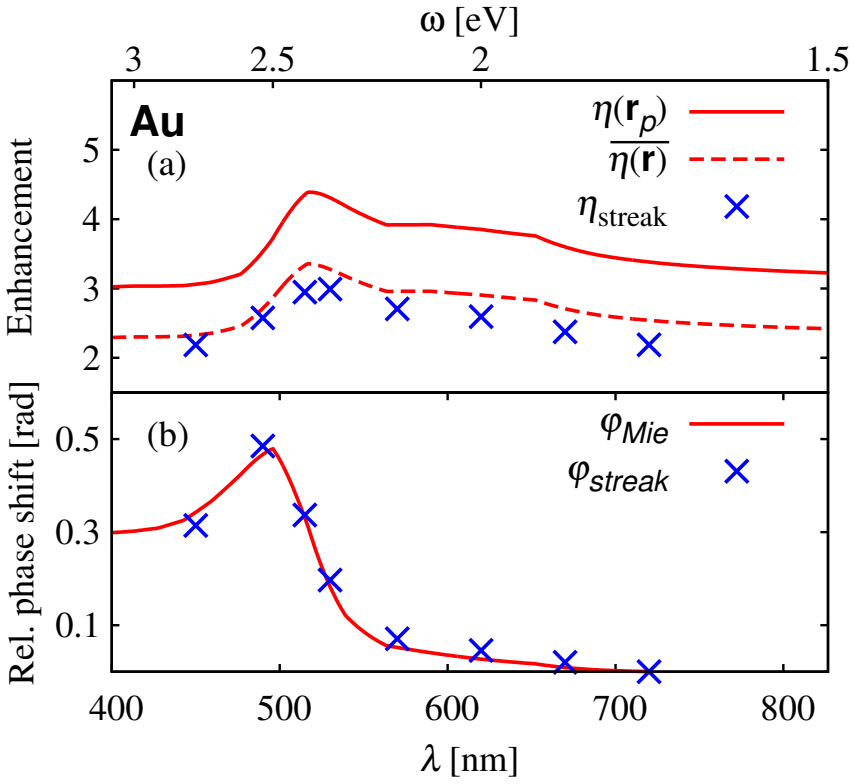


Figure 2.11: *Plasmonic amplitude-enhancement and phase-shift retrieval for 10 nm diameter Au nanospheres from streaked photoemission spectra. (a) Plasmonic field enhancement η defined in Eq. (2.4), as predicted by classical electrodynamics: $\eta(\boldsymbol{r}_p)$ (solid red line) gives values at the nanosphere poles; $\overline{\eta(\boldsymbol{r})}$ (dashed red line) gives the field-strength enhancement, dipole-averaged over the nanosphere surface. Blue markers indicate the retrieved field-strength enhancement $\eta_{streak}(\lambda)$ defined in Eq. (2.25). (b) Plasmonic phase shift $\varphi_{Mie}(\lambda)$ according to Eq. (2.27) as predicted by classical electrodynamics at the nanosphere poles (solid red line). Blue markers show the retrieved plasmonic phase-shift difference $\varphi_{streak}(\lambda)$ defined in Eq. (2.26) as a function of the streaking-pulse wavelength.*

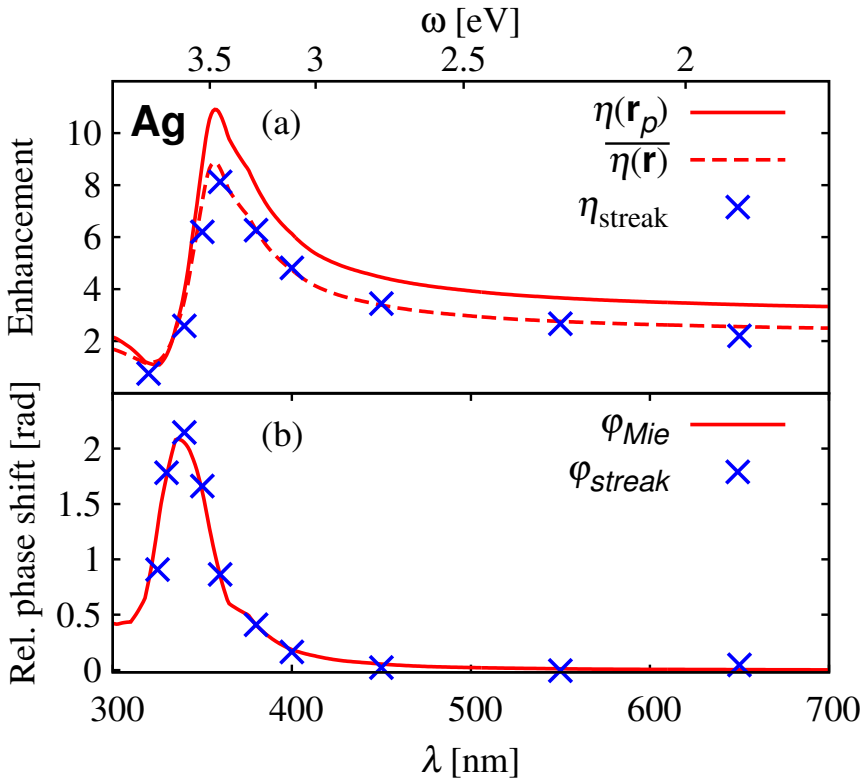


Figure 2.12: *Same as Fig. 2.11 for Ag nanospheres.*

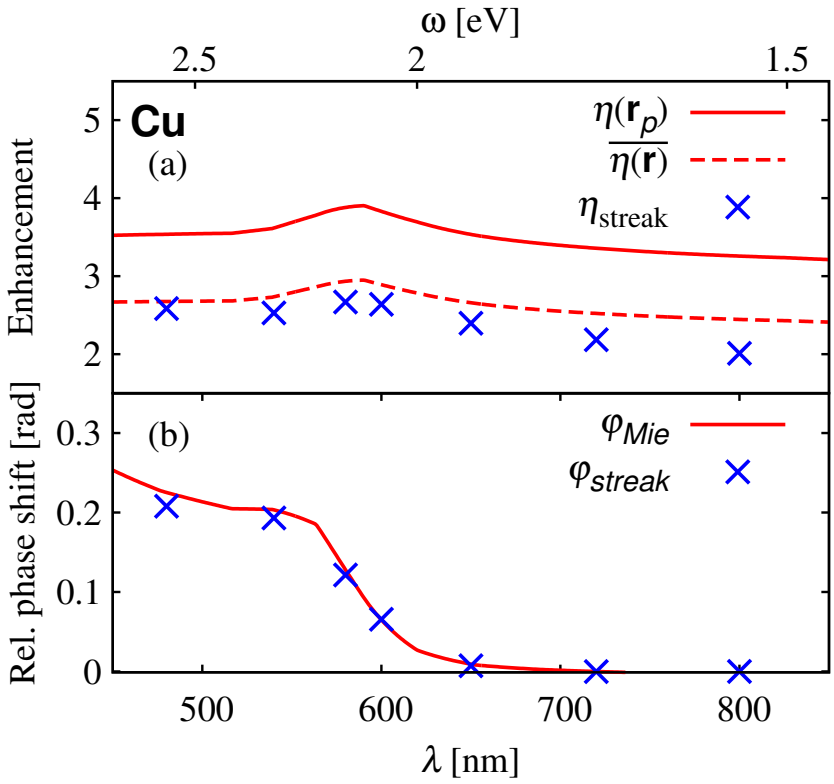


Figure 2.13: *Same as Fig. 2.11 for Cu nanospheres.*

the induced plasmonic phase shift at $\lambda = 720$ nm [cf. Eq. (2.2)]. In contrast to the averaged field-strength enhancement, averaging the phase shift over the surface with the same weight factor $|\cos\theta|^2$ does not have a noticeable effect on φ_{Mie}. This is due to the fact that as long as the nanosphere is sufficiently small compared to the streaking-pulse wavelength, the phase shift is approximately homogeneous near the nanosphere surface.

The blue markers in Figs. 2.11(b), 2.12(b), and 2.13(b) show

$$\varphi_{streak}(\lambda) = \Delta\phi_{streak}(\lambda) - \Delta\phi_{streak}(720\text{ nm}), \tag{2.28}$$

that is, the streaking-phase shifts $\Delta\phi_{streak}(\lambda)$ defined in Eq. (2.26) relative to their values at $\lambda = 720$ nm. We retrieved φ_{streak} by fitting Eq. (2.24) to our calculated streaked spectra. For all three materials, the retrieved relative phase shifts are in excellent agreement with the prediction of classical electrodynamics ('Mie theory'). In particular, the retrieved phase differences accurately reproduce (i) the distinct plasmon resonance peak for Ag [Fig. 2.12(b)], (ii) the step-like shape of the relative phase shift as a function of streaking-pulse wavelength for Cu [Fig. 2.13(b)], and a (iii) combination of both, step and peak structure, for Au [Fig. 2.11(b)].

The successful retrieval of the plasmonic phase shifts for all three materials provides strong evidence for the accumulation of streaking-wavelength-independent contributions $\Delta\phi_{prop}$ during the propagation of photoelectrons, leaving the plasmonic phase shift in the electric field, $\phi_{tot}(\mathbf{r}_p, \omega)$, as the only λ-dependent component. Writing the net accumulated phase difference in streaked photoelectron spectra as

$$\Delta\phi_{streak}(\lambda) = \phi_{tot}(\mathbf{r}_p)\big|_\lambda + \Delta\phi_{prop}, \tag{2.29}$$

and taking the difference of Eq. (2.29) for any given λ and $\lambda = 720$ nm yields,

$$\varphi_{streak}(\lambda) = \varphi_{Mie}(\lambda). \tag{2.30}$$

This confirms our numerical evidence presented above that induced plasmonic-field information can be reconstructed from streaked photoelectron spectra.

The plasmonic streaking phase shift $\varphi_{streak}(\lambda)$ can be assigned to the photoemission time delay $\varphi_{streak}(\lambda)/\omega$ induced by the collective electronic response of the nanoparticle to the streaking pulse. Maximal streaking phase shifts of 0.5 rad for Au, 2 rad for Ag, and 0.2 rad for Cu correspond to streaking time delays of 140 as, 380 as, and 60 as, respectively.

In Sec. 2.1.1 we demonstrated that the magnitude of the plasmonic field enhancement and phase shift are related to the dipole surface plasmon-resonance and interband transitions. The reconstruction of plasmonic field enhancements and phase shifts from attosecond streaked photoelectron spectroscopy may thus provide a not-yet-explored way of studying not only the dielectric response of nanoparticles, but also more intricate properties of their electronic structure, such as interband transitions.

2.3 Summary

We developed a quantum-mechanical model to numerically simulate streaked photoelectron emission from metallic nanospheres and used this method to simulate streaked photoelectron spectra from Au, Ag, and Cu nanospheres. Our study of plasmonic streaking-oscillation-amplitude enhancements and phase shifts revealed in streaked photoemission spectra, relative to simulated spectra that exclude the induced plasmonic field, show how plasmonic near-field information of metallic nanospheres can be retrieved from streaked electron spectra. Our comparative study of element-specific differences in streaking-oscillation-amplitude enhancements and phase shifts reveals the different dielectric properties of the three transition metals. This further substantiates the potential of streaked photoelectron spectroscopy for imaging plasmonic near fields, as well as the dielectric response, surface plasmon resonances, and interband transitions of different materials.

Chapter 3

Imaging plasmonic fields with atomic spatiotemporal resolution

In Chapter 2, we demonstrate that the plasmonic near-field information of metallic nanospheres is embedded and can be retrieved from streaked photoelectron spectra. Yet complete spatiotemporal imaging of the plasmonic fields near metallic nanostructures has not been achieved. The detailed analysis of spatiotemporally-resolved photoemission experiments at the sub-fs and nm scales and the exploration of novel nanoplasmonic applications rely on discipline-transcending numerical modeling within the emerging field of quantum plasmonics [6, 38, 57, 58, 93–95].

In this chapter, based on the theoretical study of streaked photoemission in Chapter 2, we propose a scheme for the reconstruction of plasmonic near-fields of isolated nanoparticles from IR-streaked XUV photoemission spectra with sub-fs temporal and nm spatial resolution [60]. We first present our proposed experimental setup in Sec. 3.1. Then in Sec. 3.2, we summarize the numerical model of simulating the streaked photoelectron spectra within this setup (Sec. 3.2.1), and present the simulated spectra containing the spatiotemporal information (Sec. 3.2.2). In Sec. 3.3, we develop the method to reconstruct the spatiotemporally-resolved plasmonic field from the streaked photoelectron spectra, which is subdivided into three subsections. The mathematical derivation of the reconstruction method is presented

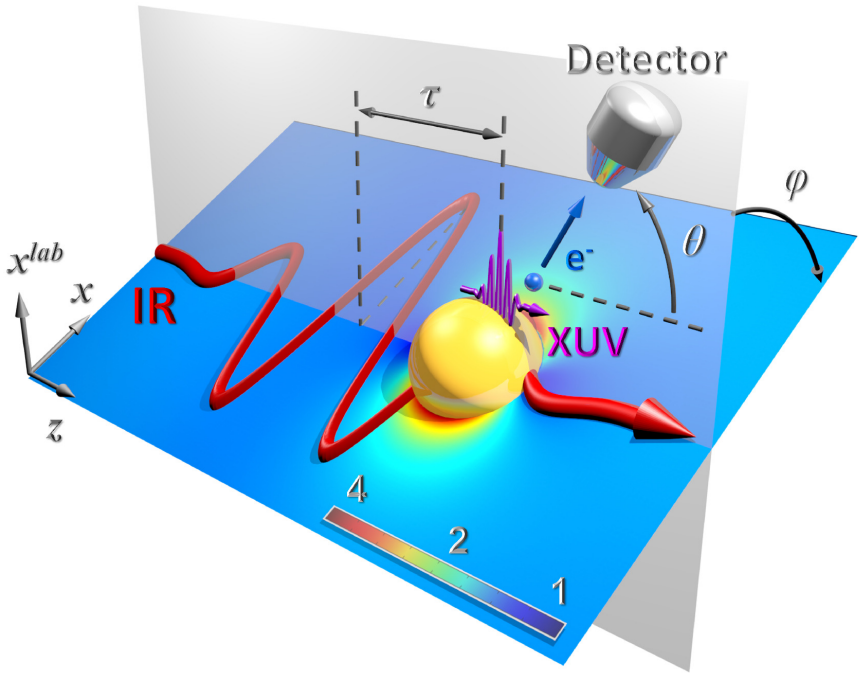


Figure 3.1: *Schematic of attosecond nanoplasmonic imaging. An attosecond XUV pulse emits electrons into the field of a delayed IR streaking laser pulse, whose polarization direction can be rotated by a variable angle φ relative to the XUV-pulse polarization. The linear color/gray scale represents the electric-field-strength enhancement for 50 nm radius Au nanospheres in 720 nm incident IR pulses.*

in Sec. 3.3.1. Then we demonstrate the validation of this method by reconstructing the spatiotemporally-resolved plasmonic field at the surface of an Au nanosphere (Sec. 3.3.2) and an Au nanoshell (Sec. 3.3.3), before summarizing this chapter in Sec. 3.4.

3.1 Suggested experimental setup

In order to image the plasmonic field with spatiotemporal resolution, we employed a modified setup from Chapter 2 (Fig. 2.1). Figure 3.1 shows the proposed experimental setup using streaked photoemission [60]. Both XUV and IR pulses propagate along the z-axis of the laboratory-fixed $x^{lab}yz$ coordinate system that is centered in the nanosphere. The XUV and IR pulse are linearly polarized along the x^{lab}- and x-axis, respectively, with adjustable relative polarization direction φ. Their time delay τ is assumed positive if the IR pulse precedes the XUV pulse. Photoelectrons are detected in the $x^{lab}z$-plane under the angle

θ with respect to the z-axis, i.e., in direction $\hat{\mathbf{n}} = (\theta, \varphi)$. Adjusting the direction $\hat{\mathbf{n}}$ and time delay τ allows for the characterization of the spatiotemporal plasmonic field $\mathbf{E}_{tot}(\mathbf{r}, t)$, induced by the IR pulse.

In this work, the XUV pulse is a Gaussian pulse with central photon energy $\omega_X = 50$ eV and FWHIM $\tau_X = 200$ as. The IR streaking pulse has 720 nm central wavelength, 2.47 fs FWHIM, and 10^{10} W/cm^2 peak intensity. Under those laser parameters, two conditions are implied which are crucial in the later discussion of this chapter.

1) The Au nanosphere has a radius $R = 50$ nm. The large streaking pulse wavelength compared to the size of the nanosphere implies *"quasi-static" conditions* for which Mie calculations show the net IR field to be efficiently screened inside and oriented perpendicular to the metallic nanoparticle surface, as for static external fields [80, 81].

2) For the assumed XUV and IR pulse parameters, photoelectrons are exposed to the streaking field over less than 10 nm. Since the field strength of the IR-pulse-induced nanoplasmonic field decays outside the particle as $\sim (R/r)^3$, the spatial range of the enhancement is $\sim R$ [19]. The streaking pulse length is therefore short compared to the time it takes photoelectrons to escape the plasmonic near-field. The *"slow-escape" condition* [5] is thus met, under which photoelectrons do not experience the spatial variation of the streaking field after being emitted from nanoparticle surface.

3.2 Simulation of photoelectron spectra

3.2.1 Numerical model

We simulate the streaked photoelectron spectra following the quantum-mechanical model in Sec. 2.1 by calculating the transition amplitude using Eq. (2.9),

$$T_i(\mathbf{k}_f, \tau) = i \int dt \int d\mathbf{r} \Psi^{\tau *}_{\mathbf{k}_f}(\mathbf{r}, t) \mathbf{A}_X(\mathbf{r}, t) \cdot \hat{\mathbf{p}} \Psi_i(\mathbf{r}, t), \qquad \text{(2.9 revisited)}$$

with XUV pulse in the new coordinates,

$$\mathbf{E}_X(\mathbf{r},t) = \hat{\mathbf{x}}^{lab} E_X \exp\left[-2\ln 2\Big(\frac{t-t_z}{\tau_X}\Big)^2 \right] e^{-i\omega_X(t-t_z)}, \tag{3.1}$$

where the retardation $t_z = z/c$, and vector potential $\mathbf{A}_X(\mathbf{r},t) = \int_t^\infty dt'\ \mathbf{E}_X(\mathbf{r},t')$.

The initial conduction-band states,

$$\Psi_i(\mathbf{r},t) = \Psi_i(\mathbf{r}) e^{-i\omega_i t}, \tag{2.10 revisited}$$

are modeled as bound states of a spherical square well of radius $R = 50$ nm and depth $V_0 = -W_f - \sigma_c = -13.1$ eV, given by adding the work function $W_f = 5.1$ eV and conduction-band width $\sigma_c = 8$ eV (Tab. 2.1.2).

The final continuum states are modeled as the exponentially damped 'Volkov' continuum wave function,

$$\Psi^\tau_{\mathbf{k}_f}(\mathbf{r},t) = \frac{1}{\sqrt{2\pi}} f[l(\mathbf{r});\lambda_i)] e^{i\mathbf{k}_f\cdot\mathbf{r}} e^{i\phi^\tau_{\mathbf{k}_f}(\mathbf{r},t)}, \tag{2.11 revisited}$$

which is calculated following Sec. 2.1.2 with the presence of the IR-induced inhomogeneous streaking field $\mathbf{E}_{tot}(\mathbf{r},t)$, simulated by employing Mie theory [80, 81] within the new coordinates in Fig. 3.1.

The total photoemission yield from all occupied conduction-band states is then calculated by incoherently adding contributions from initial states with energies ε_i at and below the Fermi energy,

$$P(\mathcal{E}_f)\big|_{\tau,\hat{\mathbf{n}}} = \frac{1}{\sqrt{2\mathcal{E}_f}} \sum_{i\in occ} |T_i(\mathbf{k}_f,\tau)|^2 = \frac{1}{\sqrt{2\mathcal{E}_f}} \sum_{i\in occ} |T_i(k_f\hat{\mathbf{n}},\tau)|^2, \tag{3.2}$$

where the photoemission yield is obtained as photoelectron kinetic energy spectra for various XUV-IR time delays τ and detection directions $\hat{\mathbf{n}}$.

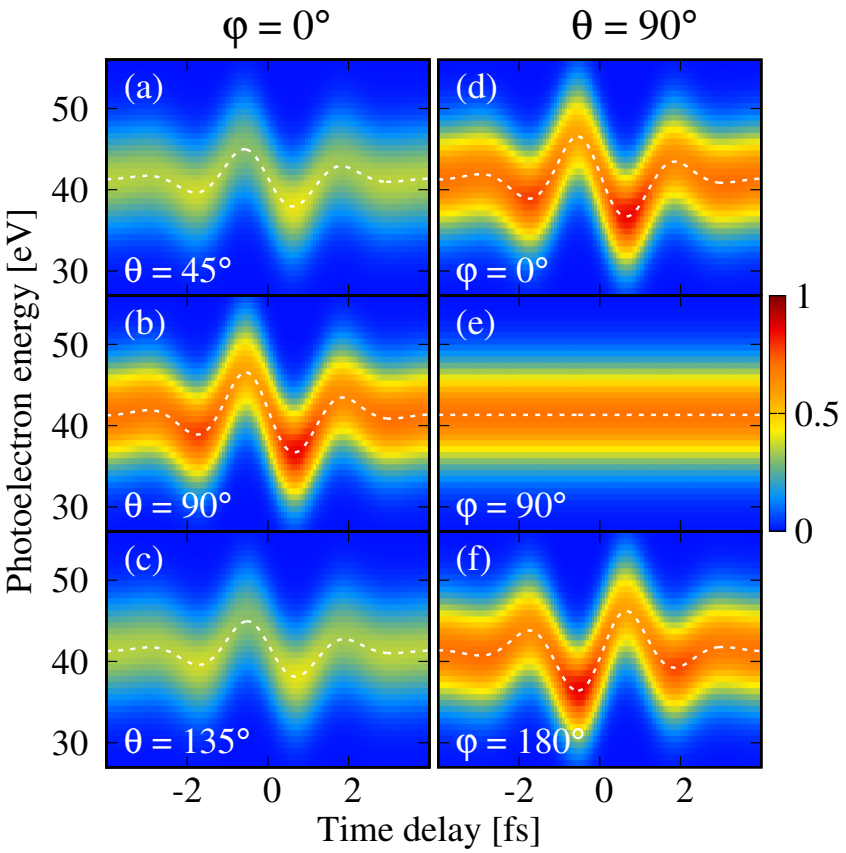


Figure 3.2: *Simulated streaked photoelectron spectra for 50 nm radius Au nanospheres at detection angles (a)-(c) $\varphi = 0°$ and (a) $\theta = 45°$, (b) 90°, (c) 135°, and (d)-(f) $\theta = 90°$ and (d) $\varphi = 0°$, (e) 90°, (f) 180°. The linear color/gray scale gives the photoemission yield normalized to the maximum yields in (a)-(f).*

3.2.2 Simulated spectra

Figure 3.2 shows streaked photoelectron spectra for various detection angles (θ, φ). For a given relative polarization direction φ, the detected peak photoemission yield is largest along the XUV polarization direction ($\theta = 90°$) and decreases proportional to $\cos^2(\theta - 90°)$, following a dipole-emission pattern [Figs. 3.2(a)-3.2(c)]. The streaking-oscillation amplitude also reaches its maximum at $\theta = 90°$, due to emission across the maximally enhanced plasmonic near-field (Fig. 3.1). For the same detection angle θ, streaking oscillations for emission in forward $\varphi = 0°$ and backward $\varphi = 180°$ direction have opposite phase due to the dipole character of the induced plasmonic field [Figs. 3.2(d)-3.2(f)]. Streaking traces calculated according to Sec. 3.2.1 follow the instantaneous net electric IR field $\mathbf{E}_{tot}$, in the same way

as streaked spectra from atoms [33, 38] and surfaces [41, 42], retracing the instantaneous electric-field velocity potential of the incident streaking pulse.

3.3 Plasmonic field reconstruction

3.3.1 Mathematical derivation

The reconstruction of the net electric field $\mathbf{E}_{tot}$ at the nanoparticle surface constitutes a challenging inversion problem, primarily since the spatial inhomogeneity of $\mathbf{E}_{tot}$ prevents the separation of Eq. (2.13) in spatial and temporal terms. However, as will be shown next, the accurate imaging of $\mathbf{E}_{tot}$ becomes possible since both the *quasi-static* and *slow-escape conditions* addressed earlier are met in Sec. 3.1. Following the mathematical derivation in Sec. 2.1.3, evaluation of the time integral in Eq. (2.9) at $\hat{\mathbf{n}} = (\theta, \varphi)$ yields,

$$T_i(\mathbf{k}_f, \tau) = \frac{\sqrt{\pi} E_X}{i\omega_X} \hat{\mathbf{x}}^{lab} \cdot \int d^3\mathbf{r} \left[\nabla \Psi_i(\mathbf{r})\right] \Psi^{\tau *}_{\mathbf{k}_f}(\mathbf{r}, t_z) e^{-i\omega_i t_z} \times \frac{1}{b^{\tau}_{\mathbf{k}_f}(\mathbf{r}, t_z)} \exp\left\{ - \left[\frac{\frac{\partial}{\partial t_z}\phi^{\tau}_{\mathbf{k}_f}(\mathbf{r}, t_z) + \omega_X + \omega_i}{2 b^{\tau}_{\mathbf{k}_f}(\mathbf{r}, t_z)} \right]^2 \right\}, \tag{3.3}$$

where,

$$b^{\tau}_{\mathbf{k}_f}(\mathbf{r}, t) = \sqrt{\frac{2\ln 2}{\tau_X^2} + \frac{i}{2}\frac{\partial^2}{\partial t^2}\phi^{\tau}_{\mathbf{k}_f}(\mathbf{r}, t)}. \tag{3.4}$$

In spherical-wave approximation, the spatial integral in Eq. (3.3) can be approximated as (see Sec. A.1 for mathematical derivation),

$$T_i(\mathbf{k}_f, \tau) \approx C_i \frac{\sqrt{2}\pi E_X R\, e^{-ik_f R - i\phi^{\tau}_{\mathbf{k}_f}(\hat{\mathbf{n}}R, \tilde{t}_z)}}{\omega_X k_f\; b^{\tau}_{\mathbf{k}_f}(\hat{\mathbf{n}}R, \tilde{t}_z)} \times \exp\left\{ - \left[\frac{\frac{\partial}{\partial t_z}\phi^{\tau}_{\mathbf{k}_f}(\hat{\mathbf{n}}R, \tilde{t}_z) + \omega_X + \omega_i}{2 b^{\tau}_{\mathbf{k}_f}(\hat{\mathbf{n}}R, \tilde{t}_z)} \right]^2 \right\}, \tag{3.5}$$

where $\tilde{t}_z = R\cos\theta/c$ and

$$C_i = \int dr \Big[\hat{\mathbf{x}}^{lab} \cdot \nabla\Psi_i(\hat{\mathbf{n}}r)\Big] \cdot f[l(\hat{\mathbf{n}}r);\kappa)]. \tag{3.6}$$

Compliance with the *slow-escape* condition justifies the approximation,

$$\begin{aligned}\frac{\partial}{\partial\tilde{t}_z}\phi^{\tau}_{\mathbf{k}_f}(\hat{\mathbf{n}}R,\tilde{t}_z) &\approx -\mathcal{E}_f - \sqrt{2\mathcal{E}_f}\hat{\mathbf{n}}\int_{\tilde{t}_z}^{\infty} dt'\ \mathbf{E}_{tot}(\hat{\mathbf{n}}R,t'+\tau)\\ &= -\mathcal{E}_f - \sqrt{2\mathcal{E}_f}\hat{\mathbf{n}}\cdot\mathbf{A}_{tot}(\hat{\mathbf{n}}R,\tilde{t}_z+\tau),\end{aligned} \tag{3.7}$$

where $\mathbf{A}_{tot}(\hat{\mathbf{n}}R,\tilde{t}_z+\tau)$ is the vector potential, whose quadratic (ponderomotive) term can be neglected at typical streaking-IR-field intensities [38]. Since $\mathbf{E}_{tot}$ can be assumed perpendicular to the nanoparticle surface (*quasi-static condition*), $\hat{\mathbf{n}}\cdot\mathbf{A}_{tot} = A_{tot}$, and thus,

$$\frac{\partial}{\partial\tilde{t}_z}\phi^{\tau}_{\mathbf{k}_f}(\hat{\mathbf{n}}R,\tilde{t}_z) \approx -\mathcal{E}_f - \sqrt{2\mathcal{E}_f}A_{tot}(\hat{\mathbf{n}}R,\tilde{t}_z+\tau) \tag{3.8}$$

$$\frac{\partial^2}{\partial\tilde{t}_z^2}\phi^{\tau}_{\mathbf{k}_f}(\hat{\mathbf{n}}R,\tilde{t}_z) \approx \sqrt{2\mathcal{E}_f}\ E_{tot}(\hat{\mathbf{n}}R,\tilde{t}_z+\tau). \tag{3.9}$$

The photoemission probability can now be written integral-free as,

$$\begin{aligned}P(\mathcal{E}_f)\big|_{\tau,\hat{\mathbf{n}}} \approx \sum_{i\in occ} &\frac{\left|\pi C_i E_X R/\omega_X\right|^2 \mathcal{E}_f^{-3/2}}{\sqrt{8\ln^2 2/\tau_X^4 + \mathcal{E}_f E_{tot}^2(\hat{\mathbf{n}}R,\tilde{t}_z+\tau)}}\\ &\times\exp\left\{-\frac{\left[\mathcal{E}_f+\sqrt{2\mathcal{E}_f}A_{tot}(\hat{\mathbf{n}}R,\tilde{t}_z+\tau)-\omega_X-\omega_i\right]^2}{\sqrt{16\ln^2 2/\tau_X^4 + 2\mathcal{E}_f E_{tot}^2(\hat{\mathbf{n}}R,\tilde{t}_z+\tau)}}\right\},\end{aligned} \tag{3.10}$$

revealing that, despite being excited at different locations in the nanosphere, photoelectrons emerging at the surface in detection direction dominate the spectrum. This lays the foundation for retrieving plasmonically enhanced electric fields using streaked photoelectron spectra.

For the numerical application in this work, the XUV-pulse spectral range is limited by $2ln2/\tau_X = 4.56$ eV, such that the center of energy (CoE) can be approximated as (see

Sec. A.2 for mathematical derivation),

$$\overline{\mathcal{E}_f}(\tau)\big|_{\hat{\mathbf{n}}} = \frac{\int d\mathcal{E}_f \; \mathcal{E}_f P(\mathcal{E}_f)}{\int d\mathcal{E}_f \; P(\mathcal{E}_f)}\bigg|_{\tau,\hat{\mathbf{n}}} \approx \omega_X + V_0 + (3/5)\sigma_c - A_{tot}(\hat{\mathbf{n}}R, \tilde{t}_z + \tau)\sqrt{2\overline{\mathcal{E}_f}(\tau)} \;\Big|_{\hat{\mathbf{n}}}. \quad (3.11)$$

This enables the inversion of Eq. (3.11) to an analytical expression for the net electric field at position $\hat{\mathbf{n}} = (\theta, \varphi)$ on the surface and time t,

$$E_{tot}(\hat{\mathbf{n}}R, t) = \frac{\partial}{\partial t}\frac{\overline{\mathcal{E}_f}(t - R\cos\theta/c) - \omega_X - (3/5)\sigma_c - V_0}{\sqrt{2\overline{\mathcal{E}_f}(t - R\cos\theta/c)}}\bigg|_{\hat{\mathbf{n}}}. \quad (3.12)$$

Applying Eq. (3.12) allows for the spatiotemporal reconstruction of the surface plasmonic field from obtained streaked photoelectron spectra.

3.3.2 Plasmonic field reconstruction of Au nanospheres

Figure 3.3 shows the reconstruction of the time-dependent electric fields at the nanosphere surface from the streaked photoelectron spectra in Fig. 3.2. The time derivative in Eq. (3.12) is calculated using B-spline interpolation. The exact and retrieved electric fields are in excellent agreement. As observed in Fig. 3.2, (i) for given φ, maximum plasmonic enhancement occurs at the IR electric-field poles at $\theta = 90°$, and (ii) for given θ, the electric fields in forward ($\phi = 0°$) and backward ($\phi = 180°$) directions have opposite phases.

For the spatiotemporal reconstruction of $E_{tot}(\hat{\mathbf{n}}R, t)$ only angles θ for which the maximum photoemission yield is no less than half of the maximum yield obtained at $\theta = 90°$ are included. While not mandatory, this restriction improves the accuracy of the field retrieval since the photoemission yield decreases with θ proportional to $\cos^2(\theta - 90°)$. We assume a uniformly spaced angular grid with $(n_\theta \times n_\varphi)$ points for $\theta \in [45°, 135°]$ and $[0°, 360°)$. Figure 3.4(a)-(e) show the spatiotemporal profiles of the incident pulse and the reconstructed plasmonically enhanced electric field at the nanosphere surface at the times t indicated in Fig. 3.4(f). The field is provided on an $(n_\theta \times n_\varphi) = (6 \times 8)$ angular grid and B-spline interpolated over the entire $\theta \in [0°, 180°]$ angular range. Both the temporal oscillation and

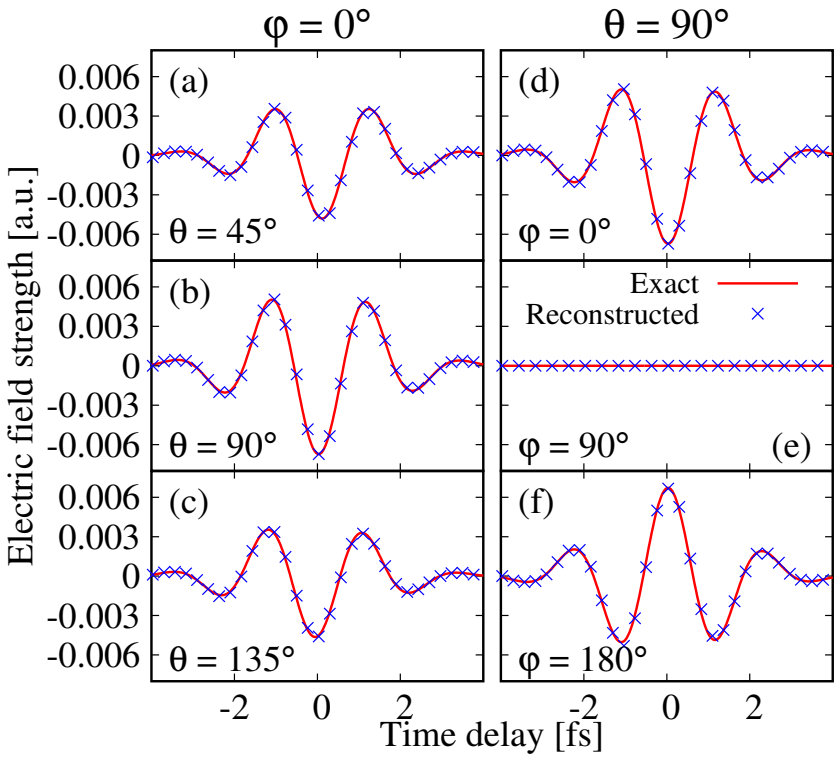


Figure 3.3: *Time-resolved reconstruction of the net plasmonic field* $E_{tot}(\hat{\boldsymbol{n}}R, t)$ *at the surface of 50 nm radius Au spheres from the streaked photoelectron spectra in Fig. 3.2. Red solid lines show surface electric fields calculated within Mie theory. Positive values indicate fields pointing outward. Blue markers represent the electric-field reconstruction according to Eq. (3.12).*

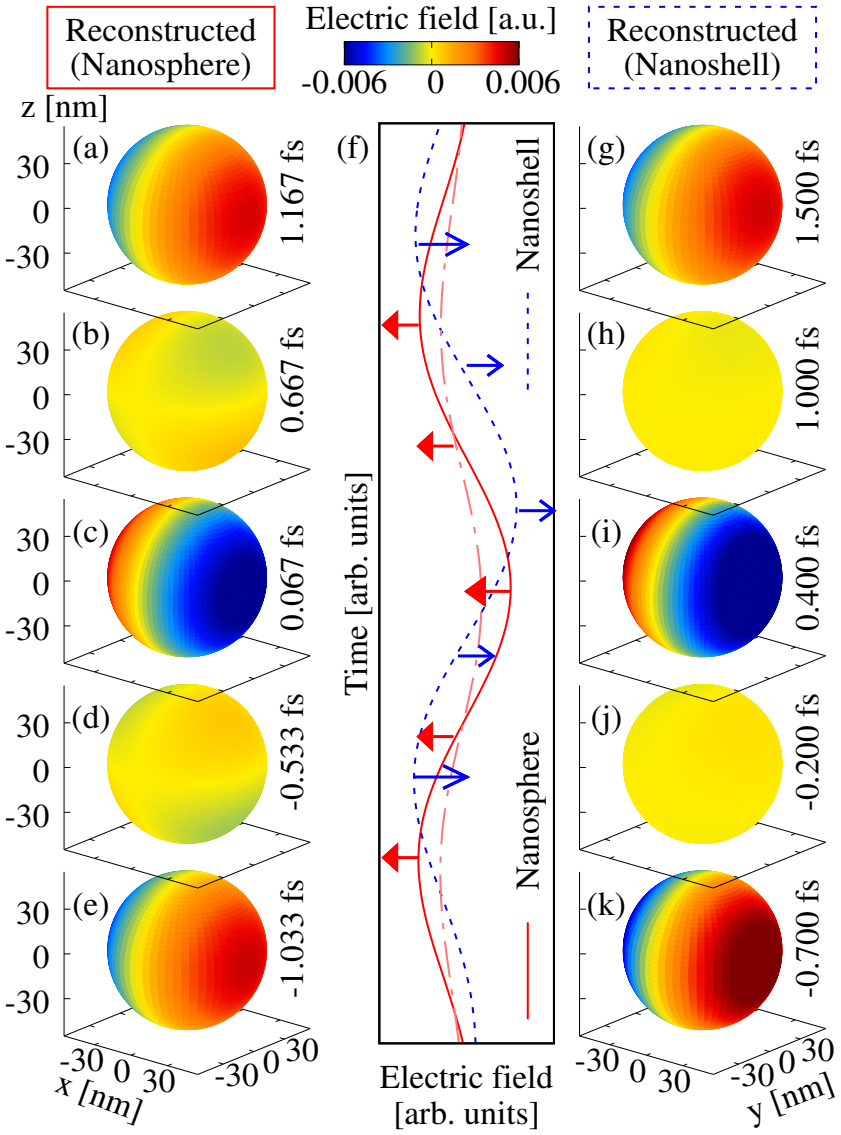


Figure 3.4: *Spatiotemporal reconstruction of the net plasmonic field* $E_{tot}(\hat{\boldsymbol{n}}R, t)$ *at the surface of 50 nm radius Au (a)-(e) spheres and (g)-(k) shells with 45 nm inner radius at times indicated by arrows in (f). (f)* $E_{tot}(\hat{\boldsymbol{n}}R, t)$ *at the poles [*$\hat{\boldsymbol{n}} = (90°, 0°)$*] of the spheres (red solid) and shells (blue dashed line). Incident IR pulses with peak intensities of* 10^{11} *(thin red dot-dashed line) and* 10^{10} W/cm^2 *(not shown) are applied to spheres and shells, respectively.*

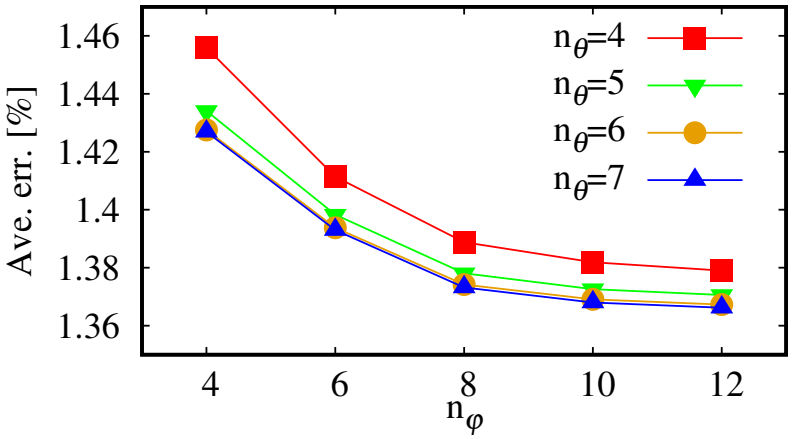


Figure 3.5: *Average field-reconstruction error for different numbers of grid points n_θ and n_φ.*

spatial propagation are observed in the reconstructed fields. A comparative animation of the spatiotemporally-resolved exact and reconstructed electric field at the surface of the nanosphere is found in the Supplementary Material of [60].

The plasmonic-field-retrieval accuracy for Au nanospheres is quantified in Fig. 3.5 in terms of the average error (including all times and the entire nanoparticle surface)

$$Err = \frac{\int d\hat{\mathbf{n}} \int dt \left| E_{tot}(\hat{\mathbf{n}}R,t) - E_{exa}(\hat{\mathbf{n}}R,t) \right|}{\max\left\{ |E_{exa}(\hat{\mathbf{n}}R,t)| \right\} \int d\hat{\mathbf{n}} \int dt} \tag{3.13}$$

as a function of the angular grid size. The error does not exceed 1.5%, and quickly converges in n_θ and n_φ. The 1.36% residual (systematic) error cannot be reduced by further increasing the number of angular grid points, due to the physical and mathematical approximations introduced in our reconstruction method.

3.3.3 Plasmonic field reconstruction of Au nanoshells

Plasmonic nanoshells are attracting increasing research interest due to promising applications in controlled drug release, biosensing, and imaging [96, 97]. As a second demonstration of our imaging method, we therefore investigated plasmonically enhanced electric fields near Au nanoshells with 50 nm outer radius and 45 nm inner radius. The plasmonic response of

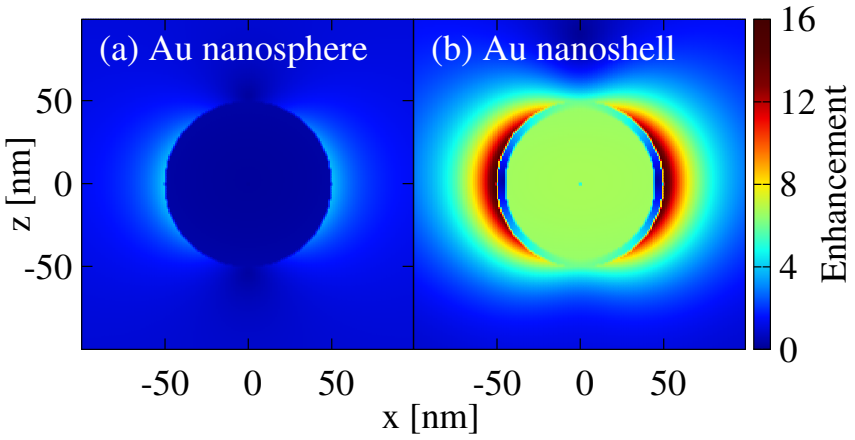


Figure 3.6: *Mie-theory simulated electric field-strength distribution of 50 nm radius Au (a) nanospheres and (b) nanoshells with 45 nm inner radius. The driving field has a wavelength of 720 nm.*

nanoshells differs from the plasmonic response of nanospheres of equal outer radius and is tunable by variation of the shell thickness. For appropriate sizes and thicknesses, metallic nanoshells reach larger plasmonic-field enhancements and resonate at a longer wavelength in the experimentally more convenient near IR range.

Figure 3.6 shows the Mie-theory-calculated electric near-field-strength distribution of 50 nm radius Au nanospheres and nanoshells with 50 nm outer and 45 nm inner radius in response to a 720 nm wavelength driving field. While exhibiting a similar quasi-dipole distribution as nanospheres, the maximum field-strength plasmonic enhancement of the spheres is $\sim$16, dramatically exceeding the factor $\sim$4 enhancement of the solid spheres.

Figure 3.7 shows the maximum plasmonic field-strength enhancement, found at the electric-field poles $\hat{\mathbf{n}} = (90°, 0°)$ as a function of the driving-field wavelength. In addition to the higher enhancement compared with nanospheres of the same size, the nanoshell plasmonic resonance is red-shifted to $\sim$710 nm, close to the 720 nm wavelength assumed in our work and in Ref. [96].

Since the Au nanoshells used here also satisfy the quasi-static and slow-escape conditions, our imaging method, without significant modification, is equally applicable to Au nanoshells by changing the initial-state potential from a spherical square well to the spherical-shell

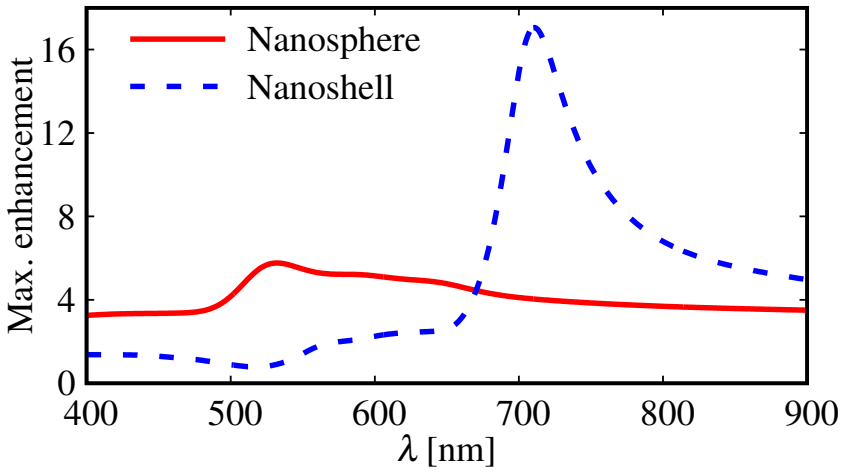


Figure 3.7: *Mie-theory simulated maximum plasmonic field-strength enhancement as a function of the driving-field wavelength for 50 nm radius Au nanospheres (red solid) and nanoshells with 45 nm inner radius (blue dashed line).*

square well potential,

$$V(r) = \begin{cases} V_0 = -13.1 \text{ eV} & 45 \text{ nm} < r < 50 \text{ nm} \\ 0 & r < 45 \text{ nm or } r > 50 \text{ nm}. \end{cases} \tag{3.14}$$

Additionally, since the plasmon resonance of the nanoshells is near the streaking-pulse wavelength, leading to a large plasmonic field enhancement, we reduced the IR-pulse intensity to 10^{10} W/cm^2 for the investigation of nanoshells, in order to yield comparable peak field strengths for spheres and shells for the purpose of demonstration.

Applying the same procedure, Fig. 3.8 shows the time-dependent net plasmonic electric fields at the surface of Au nanoshells for various detection angles (θ, φ), reconstructed from simulated streaked photoelectron spectra from Au nanoshells. The reconstructed fields are in excellent agreement with directly Mie-calculated plasmonic fields. The spatiotemporal reconstruction of the shell-plasmonic-field distribution is shown in Fig. 3.4(g)-(k). Compared to the results of Au nanospheres, a phase shift equivalent to ∼0.33 fs time-delay is observed in the reconstructed field at the surface of the Au nanoshell, due to the incident wavelength near the plasmonic resonance. An animation of the comparison among reconstructed and

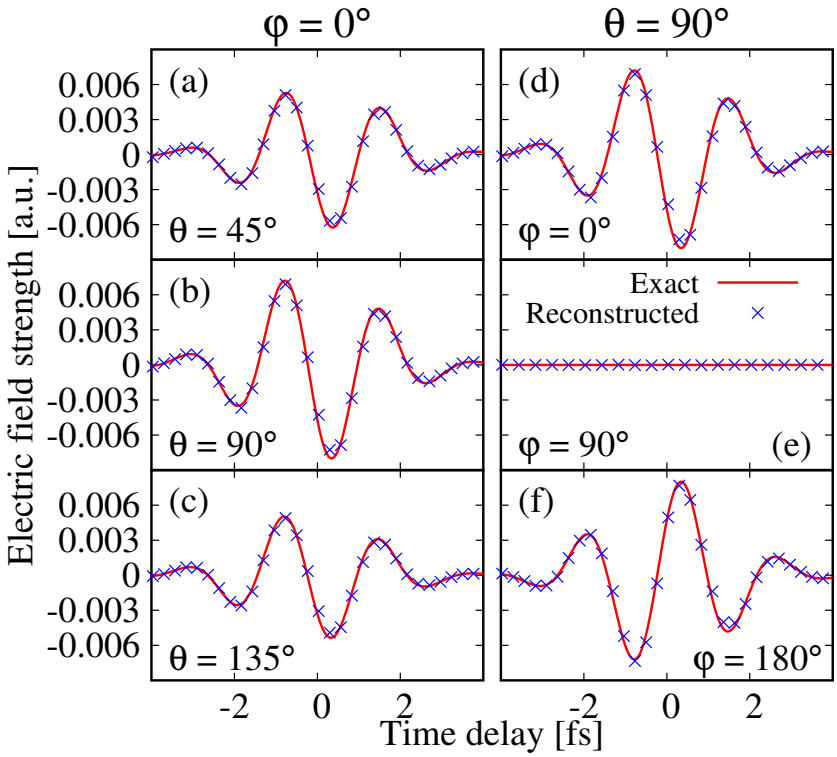


Figure 3.8: *Time-resolved reconstruction of the net plasmonic field $E_{tot}(\hat{\boldsymbol{n}}R, t)$ at the surface of 50 nm outer radius Au shells with 45 nm inner radius. Red solid lines show surface electric fields calculated within Mie theory. Positive values indicate fields pointing outward. Blue markers represent the reconstructed electric-field.*

exact electric fields at the surface of Au nanospheres and nanoshells is found in the Supplementary Material of [60], demonstrating the excellent agreement between reconstructed and exact fields, and the time delay between the reconstructed fields of the Au nanosphere and nanoshell.

3.4 Summary

Based on the quantum-mechanical model developed in Chapter 2, we show that under *quasi-static* and *slow-escape conditions*, the spatiotemporally-resolved plasmonically enhanced electric field at the surface of metallic nanospheres and nanoshells can be reconstructed with high accuracy from streaked photoelectron spectra based on a simple analytical expression. This suggests the usage of streaked photoelectron spectroscopy to image the spatiotemporally resolved electric fields at nanoparticles and nanostructured surfaces.

Chapter 4

A semi-classical approach for solving the time-dependent Schrödinger equation in spatially inhomogeneous electromagnetic pulses

In the previous chapters, we employ heuristically generalized Volkov states to model photoemission from plasmonic nanoparticles,

$$\Psi^{\tau}_{\mathbf{k}_f}(\mathbf{r},t) = \frac{1}{\sqrt{2\pi}} f[l(\mathbf{r});\lambda_i)] e^{i\mathbf{k}_f\cdot\mathbf{r}} e^{i\phi^{\tau}_{\mathbf{k}_f}(\mathbf{r},t)}. \qquad \text{(2.11 revisited)}$$

While this allows us to numerically model streaked photoemission spectra and to reconstruct plasmonic fields near Au nanospheres, a systematic mathematical solution of the time-dependent Schrödinger (TDSE) for a single active electron exposed to inhomogeneous external fields remains to be explored. In this chapter, we discuss a semiclassical model for obtaining such solutions [98]. While being approximate, our complex-phase Wentzel-Kramer-Brillouin (WKB)-type approach lends itself to systematic iterative refinement. Our proposed method, termed ACCTIVE (Action Calculation by Classical Trajectory Integration

in Varying Electromagnetic fields), employs complex classical trajectories to solve the TDSE in the presence of spatially inhomogeneous electromagnetic pulses that are represented by time-dependent inhomogeneous scalar and vector potentials. Our approach is inspired by the semiclassical complex-trajectory method for solving the TDSE with time-independent scalar interactions of Boiron and Lombardi [99] and its adaptation to time-dependent scalar interactions by Goldfarb, Schiff, and Tannor [100].

Following the mathematical formulation of ACCTIVE in Sec. 4.1, we validate this method by discussing five examples in Sec. 4.2. We first compare ACCTIVE calculations with *ab initio* numerical solutions by scrutinizing electronic states in a (i) homogeneous laser field (Sec. 4.2.1), (ii) Coulomb field (Sec. 4.2.2), and (iii) combination of laser and Coulomb fields (Sec. 4.2.3). Next, we apply ACCTIVE to streaked photoemission from (iv) hydrogen atoms (Sec. 4.2.4) and (v) plasmonic nanoparticles (Sec. 4.2.5). In the application to Au nanospheres, we examine final states for the simultaneous interaction of the photoelectron with the spatially inhomogeneous plasmonically enhanced field induced by the streaking infrared (IR) laser pulse and demonstrate the improved reconstruction of the induced nanoplasmonic IR field from streaked photoemission spectra. Section 4.3 contains our summary.

4.1 Theory

We seek approximate solutions of the TDSE for a particle of (effective) mass m and charge q in an inhomogeneous time-dependent electro-magnetic field given by the scalar and vector potentials $\phi(\mathbf{r},t)$ and $\mathbf{A}(\mathbf{r},t)$ and an additional scalar potential $V(\mathbf{r},t)$,

$$i\hbar\frac{\partial}{\partial\Psi}(\mathbf{r},t) = \left\{\frac{1}{2m}\Big[i\hbar\nabla + q\mathbf{A}(\mathbf{r},t)\Big]^2 + \varphi(\mathbf{r},t)\right\}\Psi(\mathbf{r},t), \tag{4.1}$$

where $\varphi(\mathbf{r},t) = q\phi(\mathbf{r},t) + V(\mathbf{r},t)$ and $V(\mathbf{r},t)$ is any scalar potential. Representing the wavefunction in eikonal form, $\Psi(\mathbf{r},t) = e^{iS(\mathbf{r},t)/\hbar}$, Eq. (4.1) can be rewritten in terms of the

complex-valued quantum-mechanical action $S(\mathbf{r},t)$,

$$\frac{\partial}{\partial S}(\mathbf{r},t)+\frac{1}{2m}\Big[\nabla S(\mathbf{r},t)-q\mathbf{A}(\mathbf{r},t)\Big]^2+\varphi(\mathbf{r},t)=\frac{i\hbar}{2m}\nabla\cdot\Big[\nabla S(\mathbf{r},t)-q\mathbf{A}(\mathbf{r},t)\Big]. \tag{4.2}$$

Expanding the action in powers of $\hbar$ [99, 100],

$$S(\mathbf{r},t)=\sum_{n=0}^{\infty}\hbar^n S_n(\mathbf{r},t), \tag{4.3}$$

substituting Eq. (4.3) into Eq. (4.2), and comparing terms of equal order, results in the set of coupled partial differential equations

$$\frac{\partial}{\partial S_0}(\mathbf{r},t)+\frac{\big[\nabla S_0(\mathbf{r},t)-q\mathbf{A}(\mathbf{r},t)\big]^2}{2m}+\varphi(\mathbf{r},t) = 0 \tag{4.4a}$$

$$\frac{\partial}{\partial S_1}(\mathbf{r},t)+\left[\frac{\nabla S_0(\mathbf{r},t)-q\mathbf{A}(\mathbf{r},t)}{m}\right]\cdot\nabla S_1(\mathbf{r},t) = \frac{i}{2}\nabla\cdot\left[\frac{\nabla S_0(\mathbf{r},t)-q\mathbf{A}(\mathbf{r},t)}{m}\right] \tag{4.4b}$$

$$\frac{\partial}{\partial S_n}(\mathbf{r},t)+\left[\frac{\nabla S_0(\mathbf{r},t)-q\mathbf{A}(\mathbf{r},t)}{m}\right]\cdot\nabla S_n(\mathbf{r},t) = -\frac{1}{2m}\sum_{j=1}^{n-1}\nabla S_j(\mathbf{r},t)\cdot\nabla S_{n-j}(\mathbf{r},t)+\frac{i}{2m}\nabla^2 S_{n-1}(\mathbf{r},t) \qquad (n\geq 2), \tag{4.4c}$$

where the lowest-order contribution $S_0(\mathbf{r},t)$ is the classical action of a charged particle moving in the electromagnetic field given by $\mathbf{E}(\mathbf{r},t)=-\nabla\varphi(\mathbf{r},t)/q-\partial\mathbf{A}(\mathbf{r},t)/\partial t$ and $\mathbf{B}(\mathbf{r},t)=\nabla\times\mathbf{A}(\mathbf{r},t)$.

Solving the classical Hamilton-Jacobi equation (HJE) Eq. (4.4a) leads to Newton's Second Law,

$$\frac{d}{dt}\mathbf{v}(\mathbf{r},t)=\frac{q}{m}\Big[\mathbf{E}(\mathbf{r},t)+\mathbf{v}(\mathbf{r},t)\times\mathbf{B}(\mathbf{r},t)\Big], \tag{4.5}$$

where the classical velocity field $\mathbf{v}(\mathbf{r},t)$ and kinetic momentum,

$$\mathbf{p}(\mathbf{r},t)\equiv m\mathbf{v}(\mathbf{r},t)\equiv\nabla S_0(\mathbf{r},t)-q\mathbf{A}(\mathbf{r},t), \tag{4.6}$$

are given in terms of the canonical momentum $\nabla S_0(\mathbf{r},t)$ [101]. The combination of the HJE

(4.4a) and Eq. (4.6) provides the Lagrangian $L\big[\mathbf{r},\mathbf{v}(\mathbf{r},t),t\big]$ as a total time differential of $S_0(\mathbf{r},t)$,

$$\begin{aligned}\frac{d}{dt}S_0(\mathbf{r},t) &= L\big[\mathbf{r},\mathbf{v}(\mathbf{r},t),t\big] \\ &= \frac{1}{2}m\mathbf{v}^2(\mathbf{r},t) + q\mathbf{v}(\mathbf{r},t)\cdot\mathbf{A}(\mathbf{r},t) - \varphi(\mathbf{r},t).\end{aligned} \tag{4.7}$$

Similarly, by substituting Eq. (4.6) into Eqs. (4.4b) and (4.9), we find the total time derivatives of the first-order contribution to $S(\mathbf{r},t)$,

$$\frac{d}{dt}S_1(\mathbf{r},t) = \frac{i}{2}\nabla\cdot\mathbf{v}(\mathbf{r},t), \tag{4.8}$$

and of all higher order terms,

$$\frac{d}{dt}S_n(\mathbf{r},t) = -\frac{1}{2m}\sum_{j=1}^{n-1}\nabla S_j(\mathbf{r},t)\cdot\nabla S_{n-j}(\mathbf{r},t) + \frac{i}{2m}\nabla^2 S_{n-1}(\mathbf{r},t) \qquad (n\geq 2). \tag{4.9}$$

Approximate solutions to $S(\mathbf{r},t)$ can be obtained by iteration of Eq. (4.9), after integrating the total time derivatives in Eqs. (4.7), (4.8), and (4.9) along classical trajectories $\tilde{\mathbf{r}}(t)$ that are defined by

$$\frac{d}{dt}\tilde{\mathbf{r}}(t) \equiv \mathbf{v}\big[\tilde{\mathbf{r}}(t),t\big] \tag{4.10}$$

with respect to a reference time (integration constant) t_r. The wavefunction at t_r, $\Psi_r(\mathbf{r}) = \Psi(\mathbf{r},t_r)$, provides initial ($t_r \ll 0$) or asymptotic ($t_r \gg 0$) conditions in terms of the action

$$S(\mathbf{r},t_r) = -i\hbar\ln[\Psi_r(\mathbf{r})] \tag{4.11}$$

and the velocity field

$$\begin{aligned}\mathbf{v}(\mathbf{r},t_r) &= -\frac{1}{m}\nabla S_0(\mathbf{r},t_r) - \frac{q}{m}\mathbf{A}(\mathbf{r},t_r) \\ &\approx -\frac{1}{m}\nabla S(\mathbf{r},t_r) - \frac{q}{m}\mathbf{A}(\mathbf{r},t_r) \\ &= -\frac{i\hbar\nabla\Psi_r(\mathbf{r})}{m\Psi_r(\mathbf{r})} - \frac{q}{m}\mathbf{A}(\mathbf{r},t_r). \end{aligned} \tag{4.12}$$

The semiclassical solution of Eqs. (4.7), (4.8), and (4.9) requires an appropriate classical trajectory $\tilde{\mathbf{r}}(t')$ - for any given "current" event $(\mathbf{r},t)$ - that connects the 'current' coordinate and velocity,

$$\mathbf{r} = \tilde{\mathbf{r}}(t), \qquad \mathbf{v} = \left.\frac{d\tilde{\mathbf{r}}(t')}{dt'}\right|_t, \tag{4.13}$$

to the proper coordinate and velocity at t_r,

$$\mathbf{r}_r = \tilde{\mathbf{r}}(t_r), \tag{4.14a}$$

$$\mathbf{v}_r = \left.\frac{d\tilde{\mathbf{r}}(t')}{dt'}\right|_{t_r} = -\frac{i\hbar\nabla\Psi_r(\mathbf{r}_r)}{m\Psi_r(\mathbf{r}_r)} - \frac{q}{m}\mathbf{A}(\mathbf{r}_r,t_r). \tag{4.14b}$$

The known quantities in Eqs. (4.13) and (4.14) are $\mathbf{r}$, t, and t_r, while $\mathbf{v}$, $\mathbf{r}_r$, and $\mathbf{v}_r$ are to be determined. To numerically calculate the undetermined quantities, we employ a shooting method, starting with a "trial" velocity $\mathbf{v}^{trial}$ at position $\mathbf{r}$ and time t. Propagating $\mathbf{r}$ to the reference time according to Eq. (4.5) results in $\mathbf{r}_r^{trial} = \tilde{\mathbf{r}}^{trial}(t_r)$ and $\mathbf{v}_r^{trial} = d\tilde{\mathbf{r}}^{trial}(t')/dt'\,|_{t_r}$ (Fig. 4.1).

The velocity field $\mathbf{v}$ that satisfies Eq. (4.5) can now be found numerically by finding the roots of the function

$$f(\mathbf{v}^{trial}) = \left|\mathbf{v}_r^{trial} + \frac{i\hbar\nabla\Psi_r(\mathbf{r}_r^{trial})}{m\Psi_r(\mathbf{r}_r^{trial})} + \frac{q}{m}\mathbf{A}(\mathbf{r}_r^{trial},t_r)\right| \tag{4.15}$$

for an appropriate range of start trial velocities. In our numerical applications this is accomplished by an efficient multi-dimensional quasi-Newton root-finding algorithm (Broyden's method) [102, 103]. Once the correct trajectories $\tilde{\mathbf{r}}(t')$ are determined by finding the roots of

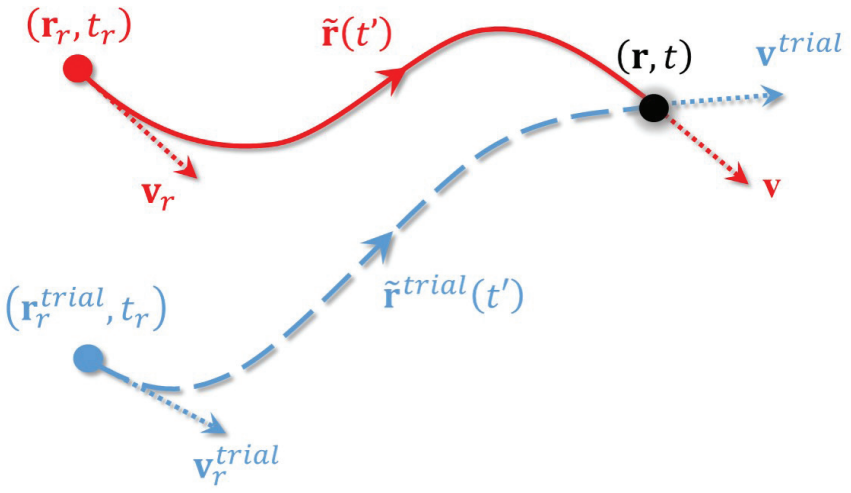


Figure 4.1: *Illustration of the shooting method used for determining classical trajectories. For any given event* $(\boldsymbol{r}, t)$ *and a predetermined reference time* t_r*, trajectories are classically propagated from trial points in phase space,* $(\boldsymbol{r}, \boldsymbol{v}^{trial})$*, at time* t *along trial trajectories* $\tilde{\boldsymbol{r}}^{trial}(t')$*. The velocity field* $\boldsymbol{v}$ *and appropriate trajectory* $\tilde{\boldsymbol{r}}(t')$ *are determined by iterating the trial velocity* $\boldsymbol{v}^{trial}$*, in order to find the roots of* $f(\boldsymbol{v}^{trial})$ *in Eq. (4.15).*

Eq. (4.15), the actions in Eqs. (4.7), (4.8), and (4.9) are integrated along these trajectories and composed - by truncating Eq. (4.3) - into an approximate solution of Eq. (4.1).

Since each term $S_n(\mathbf{r}, t)$ in Eq. (4.3) depends only on terms of lower orders, ACCTIVE enables, in principle, the systematic iterative refinement of approximate solutions of Eq. (4.1) by including successively higher orders n. The iteration is started with $S_0(\mathbf{r}, t)$, which is determined by the velocity field $\mathbf{v}(\mathbf{r}, t)$, and continued by integrating Eqs. (4.8) and (4.9).

In the numerical examples discussed in Sec. 4.2 below, we find that retaining only the zeroth- and first-order terms, $S_0(\mathbf{r}, t)$ and $S_1(\mathbf{r}, t)$, provides sufficiently accurate and physically meaningful solutions at modest numerical expense. Thus, according to Eqs. (4.7) and (4.8), we apply

$$\begin{aligned}\Psi(\mathbf{r}, t) &\approx \exp\left\{iS_0(\mathbf{r}, t)/\hbar + iS_1(\mathbf{r}, t)\right\} \\ &= e^{iS(\mathbf{r}_r, t_r)/\hbar} \exp\left\{ -\frac{1}{2}\int_{t_r}^{t} \nabla \cdot \mathbf{v}\Big(\tilde{\mathbf{r}}(t'), t'\Big)\, dt' + \frac{i}{\hbar}\int_{t_r}^{t} L\Big[\tilde{\mathbf{r}}(t'), \mathbf{v}\Big(\tilde{\mathbf{r}}(t'), t'\Big), t'\Big]\, dt' \right\}.\end{aligned} \tag{4.16}$$

For real classical trajectories and potentials, the integral of $S_0(\mathbf{r},t)$ is real, representing a local phase factor, while $S_1(\mathbf{r},t)$ is purely imaginary and defines the wavefunction amplitude, as in the standard WKB approach [88]. The quantum-mechanical probability density $\rho(\mathbf{r},t)$ then satisfies the continuity equation,

$$\frac{d\rho(\mathbf{r},t)}{dt} = \frac{d}{dt}|\Psi(\mathbf{r},t)|^2 = -\rho(\mathbf{r},t)\nabla\cdot\mathbf{v}(\mathbf{r},t), \tag{4.17}$$

for the classical probability flux $\rho(\mathbf{r},t)\,\mathbf{v}(\mathbf{r},t)$ [104].

4.2 Examples

We validate the ACCTIVE method by discussing five applications to electron wavefunctions in Coulomb and laser fields.

4.2.1 Volkov wavefunction

For the simple example of an electron in a time-dependent, spatially homogeneous laser field, the potentials in Eq. (4.1) and reference wavefunction are (in the Coulomb electromagnetic gauge [88])

$$\mathbf{A}(\mathbf{r},t) = \mathbf{A}(t), \quad \varphi(\mathbf{r},t) = 0, \quad \Psi_r(\mathbf{r}) = e^{i\mathbf{p}\cdot\mathbf{r}/\hbar}, \tag{4.18}$$

and the first-order wavefunction in Eq. (4.16) reproduces the well-known analytical Volkov solution [78],

$$\Psi^V(\mathbf{r},t) = \exp\left\{\frac{i\ \mathbf{p}\cdot\mathbf{r}}{\hbar} - \frac{i}{2m\hbar}\int_{t_r}^{t}\left[\mathbf{p} - q\mathbf{A}(t')\right]^2 dt'\right\}. \tag{4.19}$$

For details of the derivation of Eq. (4.19) within ACCTIVE see Appendix B.1.

4.2.2 Coulomb wavefunction

As a second simple example and limiting case, we consider an unbound electron in the Coulomb field of a proton. In this case the potentials in Eq. (4.1) are

$$\mathbf{A}(\mathbf{r},t) = 0, \quad \varphi(\mathbf{r},t) = -k_e \frac{e^2}{r}, \tag{4.20}$$

where e is the elementary charge and k_e the electrostatic constant. Assuming outgoing-wave boundary conditions, we define the reference wavefunction at a sufficiently large reference time t_r as the 'outgoing' Coulomb wave

$$\Psi_r(\mathbf{r},t_r) \xrightarrow{t_r\to\infty,\ z\to+\infty} e^{i\left(kz-\frac{\hbar k^2}{2m}t_r\right)}. \tag{4.21}$$

Here $\mathbf{r} = (x,y,z)$ and $p = \hbar k > 0$ is the final electron momentum. In this case the TDSE is solved exactly by the well-known Coulomb wavefunction

$$\Psi_k^C(\mathbf{r},t) = \frac{e^{\frac{\pi}{2k}}\Gamma(1-i/k)}{(2\pi)^{3/2}} {}_1F_1(i/k,1,ikr-ikz)e^{i\left(kz-\frac{\hbar k^2}{2m}t\right)} \tag{4.22}$$

in terms of the confluent hypergeometric function ${}_1F_1$. Note that for finite distances from the z-axis (i.e., for finite coordinates x and y), the asymptotic form of the Coulomb continuum wavefunction for $z \to +\infty$ is just a plane wave (without a logarithmic phase term) [88, 105].

Applying ACCTIVE to the outgoing-wave Coulomb problem, t_r must be chosen sufficiently long after t, so that each classical trajectory $\tilde{\mathbf{r}}(t')$ propagates far enough towards the $z \to +\infty$ asymptotic limit for the reference velocity to become

$$\mathbf{v}_r \xrightarrow{t_r\to\infty,\ z\to+\infty} \hat{\mathbf{z}}p/m, \tag{4.23}$$

in compliance with Eq. (4.14b). In this and for the following numerical example, we use as reference velocity the initial trial velocity for points of the spatial numerical grid that are sufficiently far away from the Coulomb singularity at the origin. The correct 'current'

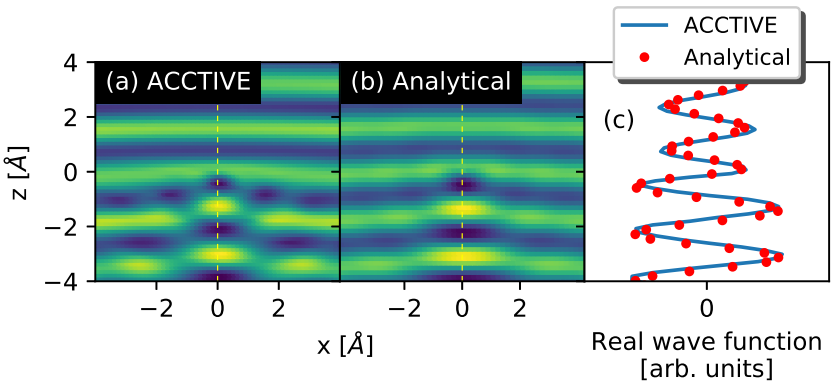


Figure 4.2: *Real part of an unbound Coulomb wavefunction, subject to the boundary condition given by an outgoing wave propagating along the z-axis. (a) Numerically calculated semi-classical 1st order ACCTIVE wavefunction. (b) Analytical Coulomb wavefunction in the $y = 0$ plane. (c) Real part of the wavefunctions in (a) and (b) along the z-axis for $x = y = 0$.*

velocities, $\mathbf{v}(\mathbf{r}, t)$ at the most distant coordinates are subsequently used as trial velocities at the nearest neighbor spatial grid points. This scheme is continued until classical trajectories for the entire spatiotemporal numerical grid are calculated. Further details of the numerical calculation of Coulomb wavefunctions within ACCTIVE are given in Appendix B.2.

Figure 4.2 shows the very good agreement between the numerically calculated 1st order ACCTIVE wavefunction (4.16) and the analytical Coulomb wavefunction (4.22) for a final electron kinetic energy of $p^2/2m = 50$ eV. The color/gray scale represents the real part of the wavefunction in the $x-z$ plane. Figures 4.2(a) and 4.2(b) show the same scattering pattern. Good quantitative agreement of the 1st order ACCTIVE wavefunction and the analytical Coulomb wavefunction is demonstrated in Fig. 4.2(c).

4.2.3 Coulomb-Volkov wavefunction

A more challenging third example is given by the motion of an electron under the combined influence of a point charge (proton), located at the coordinate origin, and a spatially homogeneous laser pulse, subject to the boundary condition Eq. (4.21). In this case, the

potentials in Eq. (4.1) are (in Coulomb gauge [88])

$$\mathbf{A}(\mathbf{r},t) = \mathbf{A}(t), \quad \varphi(\mathbf{r},t) = -k_e \frac{e^2}{r}. \tag{4.24}$$

Considering a laser pulse of finite duration, t_r must be chosen such that the laser electric field vanishes at t_r. This combination of the two previous examples in Secs. 4.2.1 and 4.2.2 constitutes the Coulomb-Volkov problem, for which merely approximate solutions [106–109], but no analytical wavefunction are known. We assume a laser pulse with 15 eV central photon energy, a cosine-square temporal intensity envelope with a pulse length of 0.5 fs full width at half intensity maximum (FWHIM), and 3×10^{15} W/cm^2 peak intensity. At time $t = 0$, the temporal pulse profile is centered at $z = 0$. We enforce the outgoing-wave boundary condition (4.21) for an asymptotic photoelectron kinetic energy of $p^2/2m = 50$ eV. This energy is reached at a sufficiently large distance of the outgoing electron from the proton and long after the pulse has vanished.

In Fig. 4.3 we compare the ACCTIVE-calculated Coulomb-Volkov wavefunction with Coulomb and Volkov wavefunctions for identical outgoing-wave boundary condition and 50 eV asymptotic photoelectron kinetic energy. The Coulomb and Volkov wavefunctions are given for a positive elementary charge and the same laser parameters as the Coulomb-Volkov wave, respectively. The color/gray scale represents the real part of the wavefunctions. We determined all numerical parameters (numerical grid size, spacing and propagation time step) to ensure convergence of the wavefunctions.

Figures 4.3(a), 4.3(b), and 4.3(c), display snapshots at time $t = 0$ of the Coulomb, ACCTIVE-calculated Coulomb-Volkov, and Volkov wavefunctions, respectively. The Coulomb-Volkov wavefunction shows a similar (inverse) Coulomb scattering pattern for the incident wave ($z < 0$) as the Coulomb wave. Its outgoing part ($z > 0$) closely matches the phase of the Volkov wave. On the other hand, the time-dependent evolution of the Coulomb-Volkov wavefunction in the $y = 0$ plane in Fig. 4.3(e) shows laser-induced wavefront distortions - similar to the Volkov wave in Fig. 4.3(f). The time evolution of the ACCTIVE-calculated Coulomb-Volkov wavefunction reveals the acceleration of the incoming and deceleration of

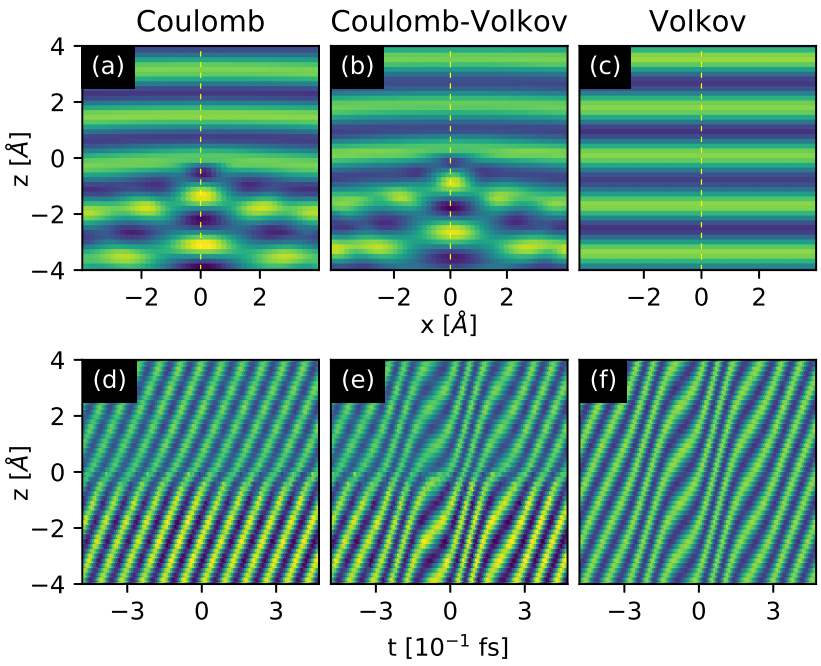


Figure 4.3: *Real parts of (a,d) Coulomb, (b,e) ACCTIVE-calculated Coulomb-Volkov, and (c,f) Volkov wavefunctions in the $y = 0$ plane. (a-c) Snapshots at time $t = 0$, when the laser-pulse center is at $z = 0$. (d-f) Time evolution along the z-axis.*

the outgoing wave near the proton at $z = 0$ of the pure Coulomb wave in Fig. 4.3(d).

4.2.4 Streaked photoemission from hydrogen atoms

As a fourth example, we employ ACCTIVE final-state wavefunctions to calculate IR-streaked XUV photoelectron spectra from ground-state hydrogen atoms [38]. We assume the ionizing XUV and streaking IR pulse as linearly polarized along the z axis. The relative time delay between the centers of the two pulses, τ, is assumed positive in case the IR precedes XUV pulse. The electric field $E_X(t)$ of the XUV pulse is characterized by a Gaussian temporal profile, 55 eV central photon energy, and a pulse length of 200 as (FWHIM). The IR pulse has a cosine-squared temporal profile, 720 nm central wavelength, pulse duration of 2 fs FWHIM, and 10^{11} W/cm^2 peak intensity.

We model streaked photoemission from the ground state of hydrogen, $|\Psi_i\rangle$, based on the

quantum-mechanical transition amplitude [38, 71, 88]

$$T(\mathbf{k}_f, \tau) \sim \int dt \, \langle \Psi^{C-V}_{\mathbf{k}_f,\tau} | z E_X(t) | \Psi_i \rangle, \tag{4.25}$$

where the IR-pulse-dressed final state of the photoelectron, $|\Psi^{C-V}_{\mathbf{k}_f,\tau}\rangle$, is a Coulomb-Volkov wavefunction [77] that we evaluate numerically using the ACCTIVE method. In a comparison calculation, we replace the Coulomb-Volkov state by the Volkov state $|\Psi^{V}_{\mathbf{k}_f,\tau}\rangle$ and assume otherwise identical physical conditions. As mentioned in the Introduction, the use of Volkov states [78] in photoionization calculations is referred to as SFA [38] and amounts to neglecting the interaction of the released photoelectron with the residual ion (proton in the present case). We scrutinize streaked photoemission spectra obtained with ACCTIVE-calculated Coulomb-Volkov final states and in SFA against *ab initio* bench-mark calculations. In these exact numerical calculations we directly solve the three-dimensional TDSE using the SCID-TDSE time-propagation code [110].

Numerical results are shown in Fig. 4.4. The streaked photoemission spectra obtained with ACCTIVE-calculated Coulomb-Volkov final states [Fig. 4.4(a)], in SFA [Fig. 4.4(b)], and by direct numerical solution of the TDSE [Fig. 4.4(c)] show very similar 'streaking traces', i.e., oscillations of the asymptotic photoelectron energy with delay τ. For a quantitative comparison, we plot in Fig. 4.4(d) the centers of energy (CoEs) of the spectra in Figs. 4.4(a-c). While the three calculations result in identical photoemission phase shifts (streaking time delays) relative to the streaking IR field, within the resolution of the graph, the ACCTIVE-calculated spectra agree with the exact TDSE calculation, while the SFA calculation predicts noticeably smaller CoEs due to the neglect of the Coulomb potential in the final photoelectron state [6].

4.2.5 Streaked photoemission from metal nanospheres

As a final, fifth, example, we apply the ACCTIVE method to model photoelectron states in *spatially inhomogeneous*, plasmonically enhanced IR electromagnetic fields. For this purpose,

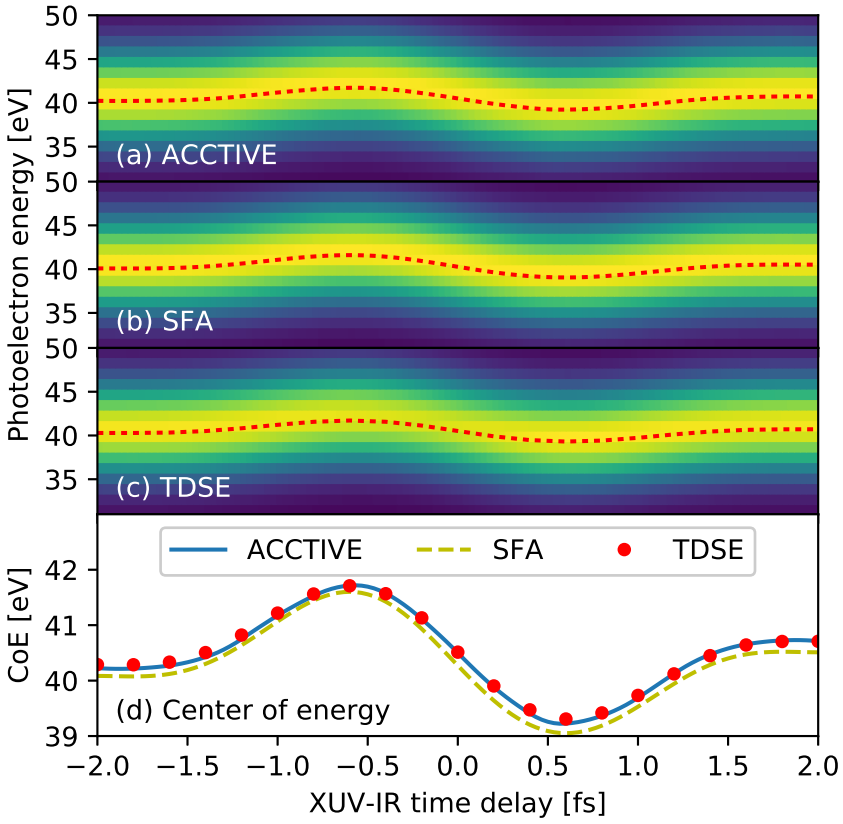


Figure 4.4: *IR-streaked XUV photoelectron spectra from hydrogen, (a) based on ACCTIVE-calculated Coulomb-Volkov final states, (b) in SFA, and (c) obtained by direct numerical solution of the TDSE. Red dotted lines in (a-c) indicate the respective centers of energy (CoE). The spectral yields in (a-c) are normalized separately, to their respective maxima. (d) Comparison of the delay-dependent CoE for the spectra in (a-c).*

we investigate streaked photoemission and the reconstruction of plasmonic near-fields for Au nanospheres with a radius of $R = 50$ nm, as proposed in Chapter 3. We calculate the transition amplitude following the theory in Sec. 3.2.1, with the important difference of employing numerically calculated semiclassical ACCTIVE final photoelectron wavefunctions, while SFA is used in Sec. 3.2.1, applying heuristically generalized Volkov final states and thus neglecting of the photoelectron interactions with the residual nanoparticle.

For the ACCTIVE calculation we thus solve the TDSE (4.1) with the potentials

$$\mathbf{A}(\mathbf{r},t) = \int_t^\infty \mathbf{E}_{\mathrm{tot}}(\mathbf{r},t')\,dt' \tag{4.26a}$$

$$\varphi(\mathbf{r},t) = \begin{cases} V_0 & r < R \\ 0 & r \geq R \end{cases}, \tag{4.26b}$$

and the boundary condition Eq. (4.21). Here, the asymptotic wavefunction in Eq. (4.21) also serves as reference wavefunction for the classical trajectory computation. The net time-dependent inhomogeneous field $\mathbf{E}_{\mathrm{tot}}(\mathbf{r},t)$ is given by the superposition of the homogeneous IR field of the incident streaking pulse and the inhomogeneous plasmonic field produced by the nanoparticle in response to the incident IR pulse Sec. 2.1.1. For the streaking calculation, we assume an XUV pulse with 30 eV central photon energy and Gaussian temporal profile with a width of 200 as (FWHIM). We further suppose a delayed Gaussian IR pulse with 720 nm central wavelength, 2.47 fs (FWHIM) pulse length, and 5×10^{10} W/cm^2 peak intensity.

Figure 4.5 shows simulated streaked photoelectron spectra obtained with ACCTIVE-calculated and Volkov final states for electron emission along the XUV-pulse polarization direction. In this direction, the effect of the induced plasmonic field on the photoelectron is strongest (See Sec. 3.3.2). The corresponding spectra in Figs. 4.5(a) and 4.5(b) show very similar temporal oscillations of the photoelectron yield and CoE as a function of both asymptotic photoelectron energy and XUV-IR pulse delay τ. As for streaked photoemission from hydrogen atoms discussed in Sec 4.2.4 above, we find that the SFA shifts the CoE to lower kinetic energies [Fig. 4.5(b), cf. Fig. 4.4(d)]. Here, the SFA results in an approximately

1.5 eV lower CoE than the ACCTIVE calculation. This energy shift is due to the fact that the SFA, by neglecting the potential well of the nanosphere in the final photoelectron state, leads to an unphysical enhancement of the photoemission cross section at lower photoelectron kinetic energies, thereby increasing the weight of low energy yields in the CoE average.

Additional comments on the comparison of streaked photoelectron spectra within either ACCTIVE or based on Volkov wavefunctions can be found in Appendix B.3.

From streaked photoemission spectra the plasmonic near-field at the nanoparticle surface can be reconstructed, as detailed in Sec. 3.3.1. Figure 4.5(d) shows the reconstructed net electric field $\mathbf{E}_{\mathrm{tot}}$ along the XUV-pulse polarization direction, i.e., at the surface and on the positive z axis of the nanosphere. The reconstruction of net plasmonically enhanced near-fields from the simulated spectra in Figs. 4.5(a) and 4.5(b) was performed using Eq. (3.12). The obtained reconstructed fields are compared in Fig. 4.5(d) with the net electric IR near-field obtained within Mie theory [80] and used as input in the streaking calculations. As is seen in Fig. 4.5(d), the ACCTIVE method improves the near-field reconstruction in comparison with the SFA calculation. The least-square deviation between the reconstructed and Mie-theory calculated fields, assembled over the entire IR pulse length, amounts to 1.62% using the ACCTIVE wavefunction and 3.05% using the SFA. The ACCTIVE method thus extends the applicability of the plasmonic near-field reconstruction scheme in Chapter 3 to lower XUV photon energies.

4.3 Summary

In summary, we propose a semi-classical method, ACCTIVE, to solve the TDSE for one active electron exposed to any spatially inhomogeneous time-dependent external force field. We validate this method by comparing ACCTIVE-calculated electronic wavefunctions with known Coulomb and Volkov wavefunctions for the electronic dynamics in Coulomb and intense laser fields, respectively, and by scrutinizing ACCTIVE-calculated final-state wavefunctions in streaked photoemission (i) from hydrogen atoms against *ab initio* numerical solutions of the TDSE, and (ii) from metallic nanospheres in plasmonic-field imaging.

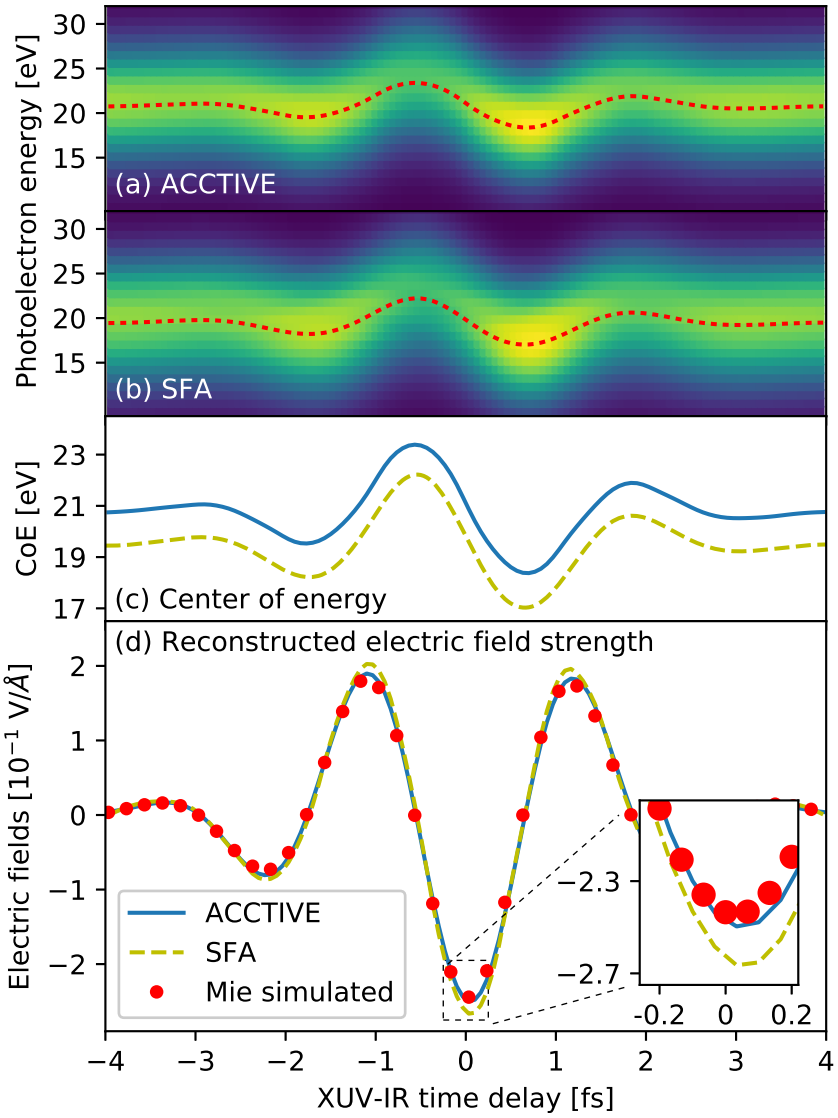


Figure 4.5: *Simulated IR-streaked XUV photoelectron spectra for photoemission along the XUV-pulse polarization direction (a) using ACCTIVE final-states and (b) in SFA. (c) Corresponding delay-dependent centers of energy. (d) Comparison of the corresponding reconstructed plasmonic electric near-fields at the point* $(x, y, z) = (0, 0, R)$ *on the nanoparticle surface with the Mie-theory-calculated electric field.*

For streaked photoemission from hydrogen atoms, we demonstrate excellent agreement of our ACCTIVE calculation with a benchmark *ab initio* TDSE calculation, while a comparative calculation using the SFA systematically deviates from the exact TDSE solution. For streaked photoemission from Au nanospheres we find that ACCTIVE final-state wavefunctions improve the reconstruction of plasmonic near-fields over SFA calculations (based on Volkov final states) at comparatively low photoelectron energies.

Chapter 5

Tracking the non-linear optical response in plasmonic nanoparticles with strong-field photoemission spectroscopy

In previous chapters, streaked photoemission is studied with the plasmonically enhanced net field $\mathbf{E}_{tot}$ simulated using Mie theory. However, only linear optical response is considered for these simulations. This approximation is valid as long as the external fields have low intensities. Since high-intensity lasers are made available in modern experiments, as well as nanostructures with high plasmonic enhancement (such as nanoshells discussed in Chapter 3.3.3), non-linear optical response can also impact the photoemission processes. Studying such effect thus becomes increasingly important in both theoretical and experimental research of strong-field photoemission [111–113].

In this chapter, in contrast to the streaked photoemission setup up used in previous chapters, we use high-energy velocity map imaging (VMI) as a tool to analyze the optical response of nanoparticles. The experiments are performed in James R. MacDonald laboratory. In Sec. 5.1 we describe the experimental setup of this study. We then use the VMI

spectrometer to study the size-dependent photoelectron cut-off energy in Sec. 5.2, demonstrating the usage of VMI photoelectron cut-off energy as a probe of near-field enhancement of nanoparticles. Based on this knowledge, in Sec. 5.3, we discuss in detail the intensity dependence of photoelectron spectra, both experimentally and theoretically, to demonstrate the effects of non-linear optical response in strong-field photoemission from SiO_2-core-Au-shell nanostructures, before we summarize this chapter in Sec. 5.4.

5.1 Experimental setup

The experiments carried out by Dr. Jeffrey Powell at James R. Macdonald Laboratory make use of intense 25 fs, $\lambda = 780$ nm laser pulses produced with a chirped pulse amplification (CPA) Ti:Sapphire laser system coupled to a VMI spectrometer to measure energy- and angle-resolved photoelectron emission. A custom-built nanoparticle source delivers a continuous nanoparticle beam of nanoparticles to the vacuum. The overall configuration of the experiment is described in [114] and similar to [19].

A colloid of Au nanoparticles are aerosolized and subsequently dried by a solid-state counter-flow membrane dryer to remove the solvent (water) from the carrier gas (N_2). The in-vacuum beam density is increased using an aerodynamic lens system to focus the gas-phase nanoparticles while a three-stage differentially pumped arrangement removes excess carrier gas. Two types of spherical Au nanoparticles with diameters ranging from 5 nm to 400 nm are selected for their narrow size distribution (<12%), solvent choice and overall purity. Solid Au nanoparticles, stabilized with citric acid, are customized products of Cytodiagnostics, Inc, while SiO_2-core-Au-shell structures (addressed as "core-shell structures"), stabilized with polyethylene glycol (PEG, 5kDa), are products of nanoComposix, Inc.

Angle and energy resolved photoelectron spectra are acquired using a thick-lens, high-energy VMI spectrometer paired with a microchannel plate (MCP) and phosphor assembly capable of imaging up to 350 eV electron energy. The use of a fast, single-shot CCD camera coupled with a real-time hit finding software routine allow for the electron spectra to be captured for each laser shot. The highest observable energy photoelectrons, or "cut-off"

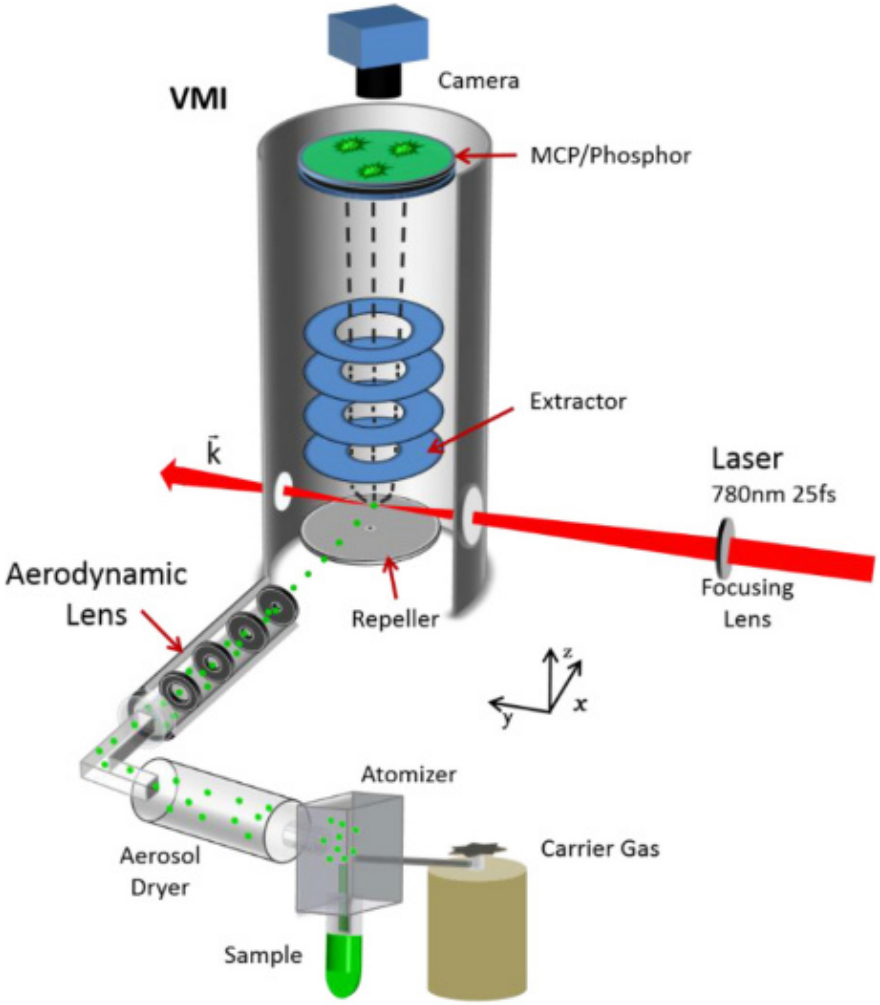


Figure 5.1: *High energy velocity map imaging (VMI) spectrometer coupled to nanoparticle source. The dilute beam of isolated gas-phase nanoparticles is injected into the vacuum and focused by an aerodynamic lens to interact with a 780 nm, 25 fs laser source. Emitted electrons are focused onto the MCP/phosphor assembly where a single-shot camera records the electron spectra for each laser shot. (Figure from [114])*

electrons, can be obtained from the non-inverted VMI images where the upper energy boundaries of the full 3D momentum sphere and the 2D projection are essentially the same as in [114].

The peak laser intensity is determined by analyzing the above-threshold (ATI) photoelectron energy distribution of atomic Xe with the aforementioned VMI under the exact experimental parameters. The ponderomotive shift of the Xe ATI comb is measured as a function of the input laser pulse energy in order to derive the ponderomotive energy $U_p \propto I_0\lambda^2$ and thus, the peak laser intensity I_0.

5.2 Size-dependent photoelectron cut-off energies

We first investigate the optical response of nanoparticles by studying the size-dependent photoelectron cut-off energy for different nanoparticles. Figures 5.2(a) and 5.2(b) show the size-dependent photoelectron cut-off energies for Au and SiO_2 nanospheres, respectively, for diameters D ranging from 5 nm to 400 nm at various intensities between 2.7 and 17.6 TW/cm^2. Here, in units of electron volts, the maximum detected photoelectron energy is plotted with respect to particle size and peak laser intensity. It can clearly be seen that the photoelectrons from Au nanoparticles are significantly faster than for their SiO_2 counterparts. By normalizing the measured cut-off energy to U_p, Fig. 5.2(c) allows for a comparison independent of laser intensity (as $U_p \propto I_0\lambda^2$ is proportional to the laser intensity). As can be seen for both the Au and SiO_2 samples, the electron cut-off energy scales linearly with peak driving laser intensity, within the diameter and intensity range studied here. The electron cut-off energy increases monotonically for both samples up to D = 200 nm, where the Au particle energy decreases.

We attribute this change in cut-off energies to the size dependence of the near-field enhancement, as addressed in Sec. 2.1.1. Figure 5.2(d) shows the Mie-simulated plasmonic field enhancement $|\eta|^2$ as a function of nanosphere diameter, where

$$|\eta|^2 = \max\left[\ |\eta(\mathbf{r})|^2\ \right] \tag{5.1}$$

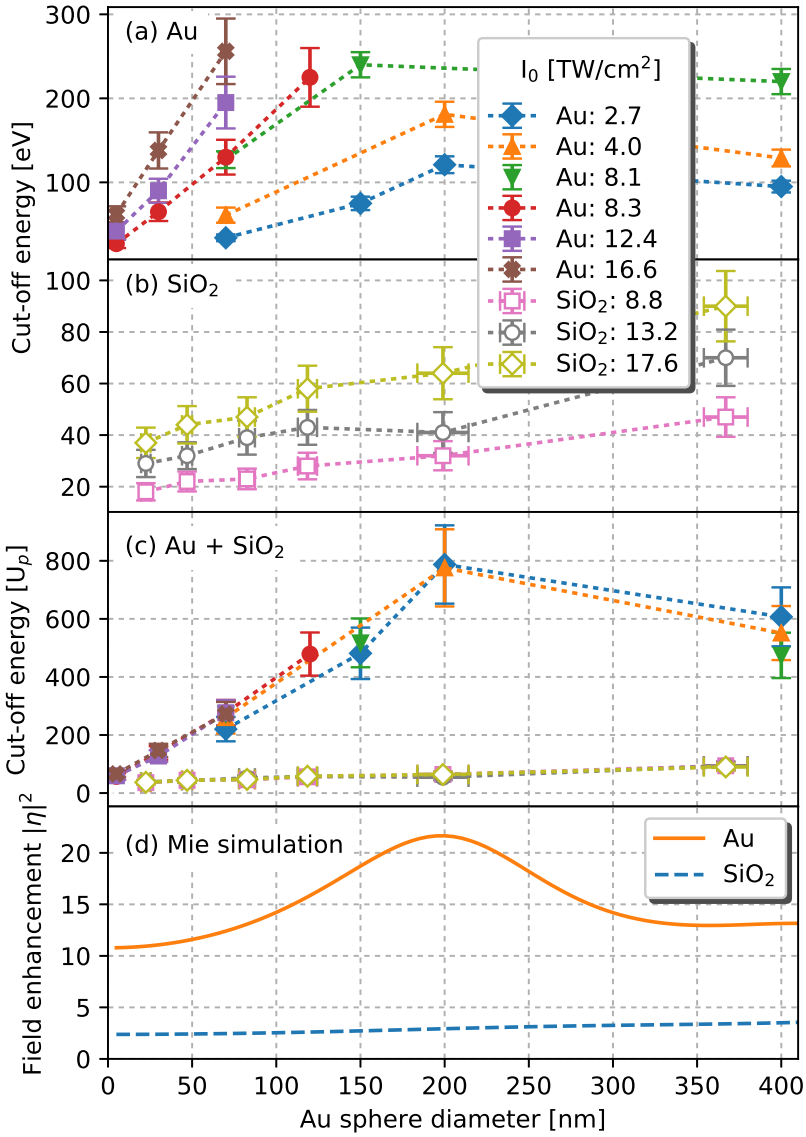


Figure 5.2: *Size-dependent maximum cut-off energies from experimental VMI spectra under various laser intensities for (a) Au, and (b) SiO_2 nanospheres, in units of eV. (c) The same cut-off energies as in (a) and (b), but on the scale of incident-field ponderomotive energy U_p. (d) Mie simulated field-intensity enhancement $|\eta|^2$ near Au and SiO_2 nanospheres.*

is the maximum field enhancement near the nanoparticles, and $\eta(\mathbf{r})$ is defined in Eq. (2.4). A qualitative similarity in Fig. 5.2(d) can be seen in the shape of the respective curves in Fig. 5.2(c). The SiO_2 nanosphere cut-offs show a slow monotonic increase mimicked in the near-field calculations. For the Au nanospheres, the Mie simulation of the near-field predicts a maximum at d = 200 nm, followed by a drop in the local intensity for larger sizes. The experimental data in Fig. 5.2(c) follow this same trend, suggesting that the electron cut-off energy is proportional to the magnitude of the respective near-field. An increase in the near-field intensity reasonably leads to higher electron energies as the photoelectron will experience this enhanced field in the continuum. Photoelectrons are therefore a sensitive probe of the near-field enhancement of their parent nanoparticle.

5.3 Intensity-dependent photoelectron cut-off energies

In the previous section, we established the relation between cut-off energy and near-field enhancement. Based on this knowledge, we now discuss the intensity-dependent photoelectron cut-off energy for different nanoparticles. Figure 5.3(a) shows the intensity-dependent photoelectron cut-off energies in eV, at 780 nm incident wavelength, of three independent experimental measurements of SiO_2-core-Au-shell structures, and two independent measurements of solid Au nanospheres. The core-shell structures have an outer diameter of $D_2 = 147 \pm 7$ nm and an inner diameter of $D_1 = 118 \pm 4$ nm. The solid Au nanospheres have a diameter of 150 ± 5 nm. All measurements show an overall increase in photoelectron cut-off energy with incident-field intensity. At very low intensities (~ 0.1 TW/cm^2), the electromagnetic field is too weak for solid Au nanospheres to induce any photoemission. However, a significant amount of photoelectrons with approximately 10 eV cut-off energy are still observed from core-shell structures, as annotated in Fig. 5.3(a), indicating that a large field enhancement is induced by core-shell structures at this intensity. As the intensity increases, photoemission starts to appear for solid Au nanospheres at approximately 0.5 TW/cm^2, and increases with incident-field intensity. However, the photoelectron cut-off energies are still significantly smaller than for core-shell structures at this intensity. This difference in cut-off energies be-

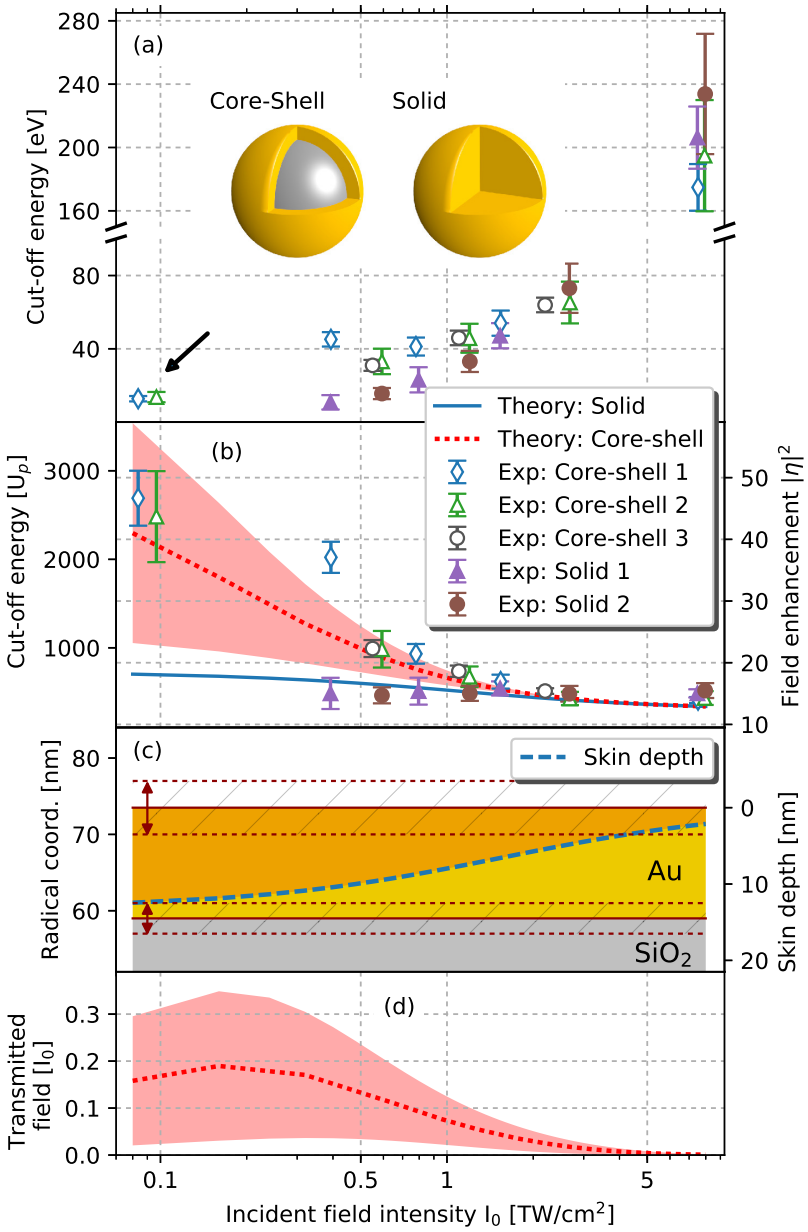


Figure 5.3: *Maximum photoelectron cut-off energies from multiple independent experiments, in units of (a) eV, and (b) incident-field ponderomotive energy U_p, using SiO_2-core-Au-shell structures (hollow markers) and solid Au nanospheres (solid markers), as a function of incident-field intensity I_0. (b) the Mie simulated field enhancement $|\eta|^2$ (scale on the right) for core-shell structures (red dotted line) and solid Au nanospheres (blue solid line). (c) the sketch of the Au-SiO_2 interface in radial coordinates, and an estimated IR skin depth (blue dashed line and darkened area, scale on the right). (d) shows the transmitted-electric-field intensity at the Au-SiO_2 interface, in units of incident-field intensity I_0. The red shaded area in (b) and (d) are the uncertainty caused by the manufacturing dispersity of the inner and outer radii of the core-shell structures, shown as the hatched area in (c). All taken at wavelength $\lambda = 780$ nm.*

tween core-shell structures and solid Au nanospheres decreases and becomes less significant when incident-field intensity exceeds 1 TW/cm^2.

This effect can again be further investigated by re-scaling the cut-off energy in units of incident-field ponderomotive energy U_p, which is shown with the same markers in Fig. 5.3(b). The re-scaled cut-off energy for solid Au nanospheres remains approximately unchanged ($\sim$ 500 U_p) for different incident-field intensities, indicating that the field enhancement near solid Au nanospheres is nearly independent of incident-field intensity. The same cut-off energy for core-shell structures, however, is significantly larger (2000 $\sim$ 3000 U_p) at low incident intensities, but drops rapidly as the intensity increases and converges to that of solid Au nanospheres beyond 1 TW/cm^2. This indicates the plasmonic field enhancement near core-shell structures is significantly larger than for solid Au spheres at low intensities. However, as the intensity increases, this difference in field enhancement drops rapidly, and vanishes above 1 TW/cm^2.

The explanation of this effect must take the non-linear optical response of the material into consideration. In previous chapters, the plasmonically enhanced electromagnetic fields are simulated with Mie theory [80, 81] and only including the linear optical response, by considering the complex index of refraction of Au and SiO_2 based on the experimental data [82, 115]. To introduce the non-linear response, we now consider the intensity dependence of the complex index of refraction n for Au [112],

$$n = n_0 + n_2 I_0, \tag{5.2}$$

where $n_0 = 0.15 + 4.74i$ is the complex index of refraction for the linear response at 780 nm, taken from Ref. [115], and I_0 is the intensity of the incident pulse. n_2 is related to the third-order susceptibility $\chi^{(3)}$, and given, in SI units, by [111],

$$n_2(\mathrm{m}^2/\mathrm{W}) = \frac{283}{n_0 \Re(n_0)} \chi^{(3)}(\mathrm{m}^2/\mathrm{V}^2), \tag{5.3}$$

where $\Re(n_0)$ is the real part of n_0, and $|\chi^{(3)}| = 7.71 \times 10^{-19}$ m^2/V^2, according to Bloem-

bergen's measurement [116]. We determine the complex phase of $\chi^{(3)}$ so that n_2 is purely imaginary, since it is known that the real part of n_2 is negligible compared to the imaginary part [111]. Therefore, Eq. (5.2) can be rewritten as,

$$n = n_R + in_I \tag{5.4}$$

where $n_R = \Re(n_0)$ is the real part, and $n_I = \Im(n_0) + \Im(n_2) * \mathrm{I}_0$ is the imaginary part. At low intensity, particularly when $\Im(n_2) * \mathrm{I}_0 \to 0$, we obtain $n \approx n_0$. Therefore the optical response is mostly linear. As intensity increases, n_I starts to increase, and the non-linear effect can become significant.

We can estimate the normal-incident IR skin depth σ using [117],

$$\sigma = \frac{c}{2\omega n_I} = \frac{c}{2\omega\big[\Im(n_0) + \Im(n_2) * \mathrm{I}_0\big]}, \tag{5.5}$$

where c is the speed of light, and $\omega = 2\pi c/\lambda$ is the IR angular frequency. Thus, the IR skin depth decreases with external field intensity. Figure 5.3(c) shows a sketch of Au-SiO_2 interface and the intensity-dependent IR skin depth. At low intensities (< 0.1 TW/cm^2), the skin depth is approximately 13 nm, comparable to the Au-shell thickness used in our experiments, suggesting a considerable amount of IR field should reach the SiO_2 core. However, as the intensity increases, σ quickly drops and approaches 2 nm at 10 TW/cm^2, well below the Au-shell thickness, preventing the IR field from penetrating the Au shell, i.e., shielding the SiO_2 core.

A more quantitative investigation of the intensity dependence can be done by employing Mie theory [80, 81] to simulate the electric field inside and outside the nanoparticles, using the intensity-dependent Au index of refraction in Eq. (5.2). We neglect the non-linear response of the SiO_2 core in the core-shell structures in this study, because the field near the SiO_2 core is shown to be greatly dampened by the Au shell, thus too weak to induce any significant non-linear response. Therefore only the index of refraction for the linear response is considered for SiO_2, shown to be 1.45 [82]. Figure 5.3(d) shows the maximum field intensity at the

Au-SiO_2 interface (transmitted field) with respect to the incident field intensity I_0, with an uncertainty range as a result of the dispersity of the inner and outer radii. The transmitted field intensity reaches up to 0.3 times the incident field at low intensities, but rapidly drops and nearly vanishes as the intensity increases. Thus, at low intensities, since a considerable amount of the field reaches the Au-SiO_2 interface for core-shell structures, the boundary conditions at both inner and outer surfaces significantly affect the optical response, causing it to respond drastically different from solid Au nanospheres of the same diameter. But at high intensities, the IR field is nearly totally screened by the Au shell and does not reach the SiO_2 core. Thus the optical response of core-shell structures appears to be indistinguishable to solid Au nanospheres of the same sizes.

To compare with the experimental results, Figure 5.3(b) also shows the Mie simulated field-intensity enhancement $|\eta|^2$ for core-shell structures and solid Au nanospheres at 780 nm incident wavelength, with scales on the right. The enhancement of solid Au nanospheres only decreases slightly from 18 to 14 as I_0 increases, indicating that the effect of the non-linear response, while presents in solid Au nanospheres, is insignificant. The core-shell structures, on the other hand, start with a field enhancement up to 60 at 780 nm wavelength and low intensities, where the linear response dominates. This large enhancement is responsible for the photoemission observed from core-shell structures at low intensities, which does not occur in solid Au nanospheres. As I_0 increases, the non-linear response starts to become significant, and the field-intensity enhancement decreases drastically, eventually converging with the solid Au nanospheres at $|\eta|^2 = 14$. The intensity dependence of the theoretically simulated field-intensity enhancements is in excellent agreement with the behavior of the experimentally measured cut-off energies for core-shell structures relative to solid Au nanospheres. This provides evidence that the measured photoelectron cut-off energy carries a signature of the changing field enhancement. While Coulomb interactions definitely play an important role in determining the absolute values, the cut-off energy is shown to be sensitive to the magnitude of the near-field enhancement. This enables us to track the non-linear optical response of the core-shell structures as a function of incident-field intensity.

We further investigate the intensity dependence by studying the wavelength-dependent

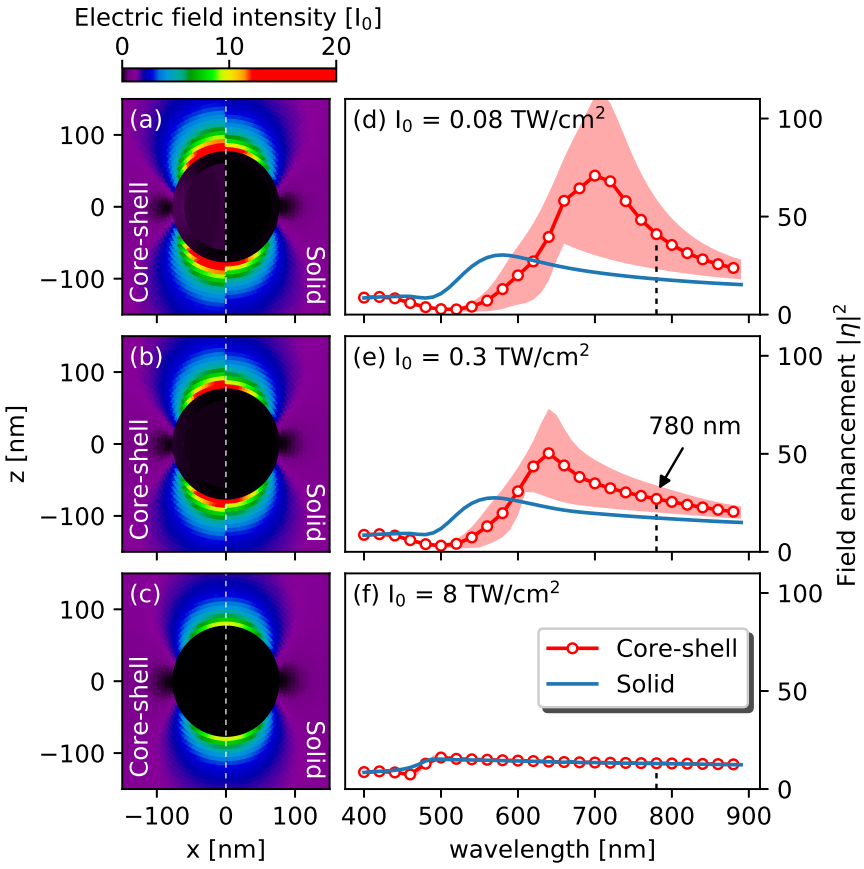


Figure 5.4: *Mie simulated spatial distribution of electric field intensity, shown as side-by-side comparison between core-shell structures (left half) and solid Au nanospheres (right half), for the incident-field wavelength of 780 nm and intensities of (a) 0.08 TW/cm^2, (b) 0.3 TW/cm^2, and (c) 8 TW/cm^2. (d-f) Simulated field enhancement $|\eta|^2$ as a function of incident wavelength, under the same respective incident-field intensities, for core-shell (red circled lines) and solid Au nanospheres (blue solid lines). The red shaded areas are the uncertainty range caused by the manufacturing dispersity of the inner and outer radii of the core-shell structures.*

dielectric response of these two nanostructures. Figure 5.4(a)-(c) compare the Mie simulated electric-field-intensity distribution between core-shell structures (left half) and solid Au nanospheres (right half) for an incident field of 780 nm wavelength. Figure 5.4(d)-(f) show the corresponding wavelength-dependent field enhancements. Both columns are simulated at three different incident-field intensities, 0.08, 0.3, and 8 TW/cm^2. At 0.08 TW/cm^2, the distribution pattern of a core-shell structure is considerably different from a solid Au nanosphere, where a weak, yet noticeable, field penetrates the Au shell to reach the SiO_2 core. Therefore, matching the boundary conditions at both inner and outer surfaces, even for field penetration, results in drastically different dielectric responses. The core-shell structures shows a significantly higher and red-shifted enhancement resonance. Such pronounced differences in the linear responses are responsible for the observed difference in cut-off energies between these two structures at low intensities, indicating that the dielectric response of core-shell structures can be greatly changed by tailoring its geometry without changing its material properties. As the incident-field intensity increases, due to the increasing non-linear effect response screening the field inside the shell, the differences between core-shell structures and solid Au nanospheres in both the electric-field-intensity distribution and the wavelength-dependent field enhancement vanish and become indistinguishable.

5.4 Summary

In this chapter, we demonstrated the first successful study of VMI spectra on isolated, gas-phase nanoparticles. We studied the size-dependent photoelectron cut-off energy of Au and SiO_2 nanospheres, and demonstrated the relationship between the cut-off energy and the simulated plasmonic field enhancement. Based on this knowledge, we then studied the intensity-dependent photoelectron cut-off energy of SiO_2-core-Au-shell structures and solid Au nanospheres, including the non-linear optical response. Our results suggest that, within the linear optical response, layered nanostructures such as Au nanoshells can be manipulated with tailored optical properties. By changing the size of the core and the thickness of the shell, the absorption spectra can be tuned across the visible and infrared range. This modifi-

cation of optical properties also indicates the ability to tune and control the magnitude of the near-field of the nanostructures. Furthermore, we found that, depending on the layer thickness, the non-linear optical response may have a significant impact on thin layered structures as the intensity increases, causing them to become indistinguishable to corresponding solid nanostructures of the same sizes. This effect can occur for typical laser parameters, thus must be taken into consideration in theoretical and experimental intense-field studies. This effect, however, by properly tailoring the geometry of the layered nanostructures, can also be used as a method to measure the third-order susceptibility $\chi^{(3)}$ of non-bulk material.

Chapter 6

Conclusion and outlook

In this chapter, we will summarize the main conclusions of this dissertation, and present a brief outlook.

6.1 Streaked photoemission from plasmonic nanoparticles

We developed a quantum-mechanical model to numerically simulate streaked photoelectron emission from metallic nanospheres, and used this method to simulate streaked photoelectron spectra from Au, Ag, and Cu nanospheres. Our study of plasmonic streaking-oscillation-amplitude enhancements and phase shifts revealed in streaked photoemission spectra, relative to simulated spectra that exclude the induced plasmonic field, suggests plasmonic near-field information of metallic nanospheres can be retrieved from streaked electron spectra. Our comparative study of element-specific differences in streaking-oscillation-amplitude enhancements and phase shifts also reveals the different dielectric properties of the three transition metals.

With proper modeling of the band structure, this method can be further improved to quantum-mechanically simulate streaked photoemission from nanostructures with different geometries (*i.e.* non-spherical nanoparticles, nanowires, nanotips, and nanostructured sur-

faces) and different materials (*i.e.* dielectric nanoparticles).

6.2 Plasmonic field imaging

Based on the previously developed quantum-mechanical model, we showed that under *quasi-static* and *slow-escape conditions*, the spatiotemporally-resolved plasmonically enhanced electric field at the surface of metallic nanospheres and nanoshells can be reconstructed with high accuracy from streaked photoelectron spectra based on a simple analytical expression. This suggests the usage of streaked photoelectron spectroscopy to image the spatiotemporally resolved electric fields at nanoparticles and nanostructured surfaces.

This imaging technique can be applied to accurately probe the optical response of nanoparticles in the presence of external fields, providing a way to study the dielectric properties, bandstructures, geometry defects, and electronic dynamics, *etc.* The idea of this reconstruction method can also be further applied to imaging plasmonic near field of different nanostructures, such as nanowires, nanotips, and nanostructured surfaces [22].

6.3 ACCTIVE method

We proposed a semi-classical method, ACCTIVE, to solve the TDSE for one active electron exposed to any spatially inhomogeneous time-dependent external force field, as an improvement of the model in Chapter 2. We validated this method by comparing ACCTIVE-calculated electronic wavefunctions with known Coulomb and Volkov wavefunctions for the electronic dynamics in Coulomb and intense laser fields, respectively, and by scrutinizing ACCTIVE-calculated final-state wavefunctions in streaked photoemission (i) from hydrogen atoms against *ab initio* numerical solutions of the TDSE, and (ii) from metallic nanospheres in plasmonic-field imaging (Chapter 3).

The applications of this method transcend the study of photoemission, giving it the potential to become a general method of solving the TDSE in spatially inhomogeneous time-dependent external force field, especially when large targets such as nanostructures

are involved or when dipole approximation fails, in which cases traditional methods become increasingly difficult. With further development, it also has the potential to be generalized to solve the TDSE of many-body systems.

6.4 Non-linear optical response in nanoparticles

Employing VMI technique, we studied the size-dependent photoelectron cut-off energy of Au and SiO_2 nanospheres, and the intensity-dependent photoelectron cut-off energy of SiO_2-core-Au-shell structures and solid Au nanospheres, including the non-linear optical response.

Our results suggest that, within linear optical response, layered nanostructures such as Au nanoshells can be manipulated with tailored optical properties. We also find that, depending on the layer thickness, the non-linear optical response may have a significant impact on thin layered structures with typical experimentally used laser intensity, causing them to become indistinguishable to corresponding solid nanostructures of the same sizes, which must be taken into consideration in theoretical and experimental intense-field studies. This effect, however, can also be used as a method to measure the third order susceptibility $\chi^{(3)}$ of non-bulk materials.

Publications

1. **J. Li**, E. Saydanzad, and U. Thumm, *Imaging Plasmonic Fields with Atomic Spatiotemporal Resolution*, Phys. Rev. Lett. **120**, 223903 (2018), URL: https://link.aps.org/doi/10.1103/PhysRevLett.120.223903

2. **J. Li**, E. Saydanzad, and U. Thumm, *Retrieving plasmonic near-field information: A quantum-mechanical model for streaking photoelectron spectroscopy of gold nanospheres*, Phys. Rev. A **94**, 051401(R) (2016), URL: http://link.aps.org/doi/10.1103/PhysRevA.94.051401

3. E. Saydanzad, **J. Li**, and U. Thumm, *Spatiotemporal imaging of plasmonic fields near nanoparticles below the diffraction limit*, Phys. Rev. A **98**, 063422 (2018), URL: https://link.aps.org/doi/10.1103/PhysRevA.98.063422

4. E. Saydanzad, **J. Li**, and U. Thumm, *Characterization of induced nanoplasmonic fields in time-resolved photoemission: A classical trajectory approach applied to gold nanospheres*, Phys. Rev. A **95**, 053406 (2017), URL: https://link.aps.org/doi/10.1103/PhysRevA.95.053406

5. **J. Li**, E. Saydanzad, and U. Thumm, *Attosecond time-resolved streaked photoelectron spectroscopy of transition-metal nanospheres*, Phys. Rev. A **95**, 043423 (2017), URL: https://link.aps.org/doi/10.1103/PhysRevA.95.043423

6. **J. Li** and U. Thumm, *A semi-classical approach for solving the time-dependent Schrödinger equation in spatially inhomogeneous electromagnetic pulses*, Submitted to Phys. Rev. A (2019)

7. J. Powell, **J. Li**, C. M. Sorensen, C. Trallero-Herrero, A. Rudenko, and U. Thumm, *Tracking the non-linear optical response in plasmonic nanoparticles with strong-field photoemission spectroscopy*, (In preparation)

Bibliography

[1] M. I. Stockman, *Nanoplasmonics: The physics behind the applications*, Phys. Today **64**, 39 (2011), URL http://scitation.aip.org/content/aip/magazine/physicstoday/article/64/2/10.1063/1.3554315.

[2] S. Law, L. Yu, A. Rosenberg, and D. Wasserman, *All-semiconductor plasmonic nanoantennas for infrared sensing*, Nano Letters **13**, 4569 (2013), pMID: 23987983, URL https://doi.org/10.1021/nl402766t.

[3] F. Krausz and M. I. Stockman, *Attosecond metrology: from electron capture to future signal processing*, Nat. Photon. **8**, 205 (2014), URL https://doi.org/10.1038/nphoton.2014.28.

[4] S. Zherebtsov, T. Fennel, J. Plenge, E. Antonsson, I. Znakovskaya, A. Wirth, O. Herrwerth, F. Süßmann, C. Peltz, I. Ahmad, et al., *Controlled near-field enhanced electron acceleration from dielectric nanospheres with intense few-cycle laser fields*, Nature Physics **7**, 656 (2011), ISSN 1745-2481, URL https://doi.org/10.1038/nphys1983.

[5] F. Kelkensberg, A. F. Koenderink, and M. J. J. Vrakking, *Attosecond streaking in a nano-plasmonic field*, New Journal of Physics **14**, 093034 (2012), URL http://stacks.iop.org/1367-2630/14/i=9/a=093034.

[6] J. Li, E. Saydanzad, and U. Thumm, *Retrieving plasmonic near-field information: A quantum-mechanical model for streaking photoelectron spectroscopy of gold nanospheres*, Phys. Rev. A **94**, 051401 (2016), URL http://link.aps.org/doi/10.1103/PhysRevA.94.051401.

[7] M. I. Stockman, M. F. Kling, U. Kleineberg, and F. Krausz, *Attosecond nanoplasmonic-*

field microscope, Nature Photonics **1**, 539 (2007), ISSN 1749-4893, URL https://doi.org/10.1038/nphoton.2007.169.

[8] A. Kinkhabwala, Z. Yu, S. Fan, Y. Avlasevich, K. Müllen, and W. E. Moerner, *Large single-molecule fluorescence enhancements produced by a bowtie nanoantenna*, Nature Photonics **3**, 654 (2009), ISSN 1749-4893, URL https://doi.org/10.1038/nphoton.2009.187.

[9] S. L. Stebbings, F. Süßmann, Y.-Y. Yang, A. Scrinzi, M. Durach, A. Rusina, M. I. Stockman, and M. F. Kling, *Generation of isolated attosecond extreme ultraviolet pulses employing nanoplasmonic field enhancement: optimization of coupled ellipsoids*, New Journal of Physics **13**, 073010 (2011), URL https://doi.org/10.1088%2F1367-2630%2F13%2F7%2F073010.

[10] E. Skopalová, D. Y. Lei, T. Witting, C. Arrell, F. Frank, Y. Sonnefraud, S. A. Maier, J. W. G. Tisch, and J. P. Marangos, *Numerical simulation of attosecond nanoplasmonic streaking*, New Journal of Physics **13**, 083003 (2011), URL https://doi.org/10.1088%2F1367-2630%2F13%2F8%2F083003.

[11] M. Becker, W. C.-W. Huang, H. Batelaan, E. J. Smythe, and F. Capasso, *Measurement of the ultrafast temporal response of a plasmonic antenna*, Annalen der Physik **525**, L6 (2013), URL https://onlinelibrary.wiley.com/doi/abs/10.1002/andp.201200206.

[12] S. Kim, J. Jin, Y.-J. Kim, I.-Y. Park, Y. Kim, and S.-W. Kim, *Kim et al. reply*, Nature **485**, E2 (2012), ISSN 1476-4687, URL https://doi.org/10.1038/nature10979.

[13] P. Dombi, A. Hörl, P. Rácz, I. Márton, A. Trügler, J. R. Krenn, and U. Hohenester, *Ultrafast strong-field photoemission from plasmonic nanoparticles*, Nano Letters **13**, 674 (2013), URL https://doi.org/10.1021/nl304365e.

[14] E. Le Ru and P. Etchegoin, *Principles of Surface-Enhanced Raman Spectroscopy: And Related Plasmonic Effects* (Elsevier, Oxford, 2008).

[15] M. T. Sheldon, J. van de Groep, A. M. Brown, A. Polman, and H. A. Atwater, *Plasmoelectric potentials in metal nanostructures*, Science **346**, 828 (2014), ISSN 0036-8075, URL http://science.sciencemag.org/content/346/6211/828.

[16] X. Zhang, Y. L. Chen, R.-S. Liu, and D. P. Tsai, *Plasmonic photocatalysis*, Reports on Progress in Physics **76**, 046401 (2013), URL https://doi.org/10.1088%2F0034-4885%2F76%2F4%2F046401.

[17] W. Chen, C. Ayala-Orozco, N. C. Biswal, C. Perez-Torres, M. Bartels, R. Bardhan, G. Stinnet, X.-D. Liu, B. Ji, A. Deorukhkar, et al., *Targeting pancreatic cancer with magneto-fluorescent theranostic gold nanoshells*, Nanomedicine **9**, 1209 (2014), URL https://doi.org/10.2217/nnm.13.84.

[18] S. A. Maier and H. A. Atwater, *Plasmonics: Localization and guiding of electromagnetic energy in metal/dielectric structures*, Journal of Applied Physics **98**, 011101 (2005), URL https://doi.org/10.1063/1.1951057.

[19] F. Süßmann and M. F. Kling, *Attosecond nanoplasmonic streaking of localized fields near metal nanospheres*, Phys. Rev. B **84**, 121406 (2011), URL http://link.aps.org/doi/10.1103/PhysRevB.84.121406.

[20] A. G. Borisov, P. M. Echenique, and A. K. Kazansky, *Attostreaking with metallic nanoobjects*, New Journal of Physics **14**, 023036 (2012), URL https://doi.org/10.1088%2F1367-2630%2F14%2F2%2F023036.

[21] J. S. Prell, L. J. Borja, D. M. Neumark, and S. R. Leone, *Simulation of attosecond-resolved imaging of the plasmon electric field in metallic nanoparticles*, Annalen der Physik **525**, 151 (2013), URL https://onlinelibrary.wiley.com/doi/abs/10.1002/andp.201200201.

[22] B. Förg, J. Schötz, F. Süßmann, M. Förster, M. Krüger, B. Ahn, W. A. Okell, K. Wintersperger, S. Zherebtsov, A. Guggenmos, et al., *Attosecond nanoscale near-field sam-*

pling, Nat. Commun. **7**, 11717 (2016), ISSN 2041-1723, URL https://doi.org/10.1038/ncomms11717.

[23] M. L. Juan, M. Righini, and R. Quidant, *Plasmon nano-optical tweezers*, Nature Photonics **5**, 349 (2011), ISSN 1749-4893, URL https://doi.org/10.1038/nphoton.2011.56.

[24] B. H. Bransden and C. J. Joachain, *Physics of atoms and molecules* (Englewood Cliffs, NJ, Prentice–Hall, 2003).

[25] K. T. Kim, D. M. Villeneuve, and P. B. Corkum, *Manipulating quantum paths for novel attosecond measurement methods*, Nature Photonics **8**, 187 (2014), ISSN 1749-4893, URL https://doi.org/10.1038/nphoton.2014.26.

[26] S. R. Leone, C. W. McCurdy, J. Burgdrfer, L. S. Cederbaum, Z. Chang, N. Dudovich, J. Feist, C. H. Greene, M. Ivanov, R. Kienberger, et al., *What will it take to observe processes in 'real time'?*, Nat. Photon. **8**, 162 (2014), URL https://doi.org/10.1038/nphoton.2014.48.

[27] M. Lucchini, A. Ludwig, L. Kasmi, L. Gallmann, and U. Keller, *Semi-classical approach to compute rabbitt traces in multi-dimensional complex field distributions*, Opt. Express **23**, 8867 (2015), URL http://www.opticsexpress.org/abstract.cfm?URI=oe-23-7-8867.

[28] C. Chen, Z. Tao, A. Carr, P. Matyba, T. Szilvási, S. Emmerich, M. Piecuch, M. Keller, D. Zusin, S. Eich, et al., *Distinguishing attosecond electron–electron scattering and screening in transition metals*, Proceedings of the National Academy of Sciences **114**, E5300 (2017), ISSN 0027-8424, URL https://www.pnas.org/content/114/27/E5300.

[29] A. H. Zewail, *Femtochemistry: Atomic-scale dynamics of the chemical bond*, The Journal of Physical Chemistry A **104**, 5660 (2000), URL https://doi.org/10.1021/jp001460h.

[30] U. Thumm, T. Niederhausen, and B. Feuerstein, *Time-series analysis of vibrational nuclear wave-packet dynamics in D_2^+*, Phys. Rev. A **77**, 063401 (2008), URL https://link.aps.org/doi/10.1103/PhysRevA.77.063401.

[31] S. De, M. Magrakvelidze, I. A. Bocharova, D. Ray, W. Cao, I. Znakovskaya, H. Li, Z. Wang, G. Laurent, U. Thumm, et al., *Following dynamic nuclear wave packets in n_2, o_2, and co with few-cycle infrared pulses*, Phys. Rev. A **84**, 043410 (2011), URL https://link.aps.org/doi/10.1103/PhysRevA.84.043410.

[32] R. Kienberger, E. Goulielmakis, M. Uiberacker, A. Baltuska, V. Yakovlev, F. Bammer, A. Scrinzi, T. Westerwalbesloh, U. Kleineberg, U. Heinzmann, et al., *Atomic transient recorder*, Nature **427**, 817 (2004), ISSN 1476-4687, URL https://doi.org/10.1038/nature02277.

[33] M. Schultze, M. Fieß, N. Karpowicz, J. Gagnon, M. Korbman, M. Hofstetter, S. Neppl, A. L. Cavalieri, Y. Komninos, T. Mercouris, et al., *Delay in photoemission*, Science **328**, 1658 (2010), ISSN 0036-8075, URL https://science.sciencemag.org/content/328/5986/1658.

[34] K. Klünder, J. M. Dahlström, M. Gisselbrecht, T. Fordell, M. Swoboda, D. Guénot, P. Johnsson, J. Caillat, J. Mauritsson, A. Maquet, et al., *Probing single-photon ionization on the attosecond time scale*, Phys. Rev. Lett. **106**, 143002 (2011), URL https://link.aps.org/doi/10.1103/PhysRevLett.106.143002.

[35] D. Guénot, K. Klünder, C. L. Arnold, D. Kroon, J. M. Dahlström, M. Miranda, T. Fordell, M. Gisselbrecht, P. Johnsson, J. Mauritsson, et al., *Photoemission-time-delay measurements and calculations close to the 3s-ionization-cross-section minimum in ar*, Phys. Rev. A **85**, 053424 (2012), URL https://link.aps.org/doi/10.1103/PhysRevA.85.053424.

[36] E. Goulielmakis, M. Uiberacker, R. Kienberger, A. Baltuska, V. Yakovlev, A. Scrinzi, T. Westerwalbesloh, U. Kleineberg, U. Heinzmann, M. Drescher, et al., *Direct mea-*

surement of light waves, Science **305**, 1267 (2004), ISSN 0036-8075, URL https://science.sciencemag.org/content/305/5688/1267.

[37] F. Krausz and M. Ivanov, *Attosecond physics*, Rev. Mod. Phys. **81**, 163 (2009), URL https://link.aps.org/doi/10.1103/RevModPhys.81.163.

[38] U. Thumm, Q. Liao, E. M. Bothschafter, F. Süßmann, M. F. Kling, and R. Kienberger, *Photonics, Volume 1: Fundamentals of Photonics and Physics*, D. L. Andrews, ed. (Wiley, 2015), chap. 13.

[39] S. Neppl, R. Ernstorfer, E. M. Bothschafter, A. L. Cavalieri, D. Menzel, J. V. Barth, F. Krausz, R. Kienberger, and P. Feulner, *Attosecond time-resolved photoemission from core and valence states of magnesium*, Phys. Rev. Lett. **109**, 087401 (2012), URL https://link.aps.org/doi/10.1103/PhysRevLett.109.087401.

[40] Q. Liao and U. Thumm, *Attosecond Time-Resolved Photoelectron Dispersion and Photoemission Time Delays*, Phys. Rev. Lett. **112**, 023602 (2014), URL http://link.aps.org/doi/10.1103/PhysRevLett.112.023602.

[41] S. Neppl, R. Ernstorfer, A. L. Cavalieri, C. Lemell, G. Wachter, E. Magerl, E. M. Bothschafter, M. Jobst, M. Hofstetter, U. Kleineberg, et al., *Direct observation of electron propagation and dielectric screening on the atomic length scale*, Nature **517**, 342 (2015), ISSN 1476-4687, URL https://doi.org/10.1038/nature14094.

[42] Q. Liao and U. Thumm, *Attosecond time-resolved streaked photoemission from mg-covered w(110) surfaces*, Phys. Rev. A **92**, 031401 (2015), URL https://link.aps.org/doi/10.1103/PhysRevA.92.031401.

[43] L. Seiffert, Q. Liu, S. Zherebtsov, A. Trabattoni, P. Rupp, M. C. Castrovilli, M. Galli, F. Süßmann, K. Wintersperger, J. Stierle, et al., *Attosecond chronoscopy of electron scattering in dielectric nanoparticles*, Nat. Phys. **13**, 766 (2017), URL https://doi.org/10.1038/nphys4129.

[44] F. Siek, S. Neb, P. Bartz, M. Hensen, C. Strüber, S. Fiechter, M. Torrent-Sucarrat, V. M. Silkin, E. E. Krasovskii, N. M. Kabachnik, et al., *Angular momentum–induced delays in solid-state photoemission enhanced by intra-atomic interactions*, Science **357**, 1274 (2017), ISSN 0036-8075, URL https://science.sciencemag.org/content/357/6357/1274.

[45] R. Locher, L. Castiglioni, M. Lucchini, M. Greif, L. Gallmann, J. Osterwalder, M. Hengsberger, and U. Keller, *Energy-dependent photoemission delays from noble metal surfaces by attosecond interferometry*, Optica **2**, 405 (2015), URL http://www.osapublishing.org/optica/abstract.cfm?URI=optica-2-5-405.

[46] Z. Tao, C. Chen, T. Szilvási, M. Keller, M. Mavrikakis, H. Kapteyn, and M. Murnane, *Direct time-domain observation of attosecond final-state lifetimes in photoemission from solids*, Science **353**, 62 (2016), ISSN 0036-8075, URL http://dx.doi.org/10.1126/science.aaf6793.

[47] V. Loriot, A. Marciniak, G. Karras, B. Schindler, G. Renois-Predelus, I. Compagnon, B. Concina, R. Brédy, G. Celep, C. Bordas, et al., *Angularly resolved RABBITT using a second harmonic pulse*, Journal of Optics **19**, 114003 (2017), URL https://doi.org/10.1088%2F2040-8986%2Faa8e10.

[48] M. Drescher, M. Hentschel, R. Kienberger, M. Uiberacker, V. Yakovlev, A. Scrinzi, T. Westerwalbesloh, U. Kleineberg, U. Heinzmann, and F. Krausz, *Time-resolved atomic inner-shell spectroscopy*, Nature **419**, 803 (2002), ISSN 1476-4687, URL https://doi.org/10.1038/nature01143.

[49] P. Johnsson, J. Mauritsson, T. Remetter, A. L'Huillier, and K. J. Schafer, *Attosecond control of ionization by wave-packet interference*, Phys. Rev. Lett. **99**, 233001 (2007), URL https://link.aps.org/doi/10.1103/PhysRevLett.99.233001.

[50] H. Wang, M. Chini, S. Chen, C.-H. Zhang, F. He, Y. Cheng, Y. Wu, U. Thumm, and Z. Chang, *Attosecond time-resolved autoionization of argon*, Phys. Rev. Lett.

105, 143002 (2010), URL https://link.aps.org/doi/10.1103/PhysRevLett.105.143002.

[51] C. Ott, A. Kaldun, P. Raith, K. Meyer, M. Laux, J. Evers, C. H. Keitel, C. H. Greene, and T. Pfeifer, *Lorentz meets fano in spectral line shapes: A universal phase and its laser control*, Science **340**, 716 (2013), ISSN 0036-8075, URL https://science.sciencemag.org/content/340/6133/716.

[52] B. Bernhardt, A. R. Beck, X. Li, E. R. Warrick, M. J. Bell, D. J. Haxton, C. W. McCurdy, D. M. Neumark, and S. R. Leone, *High-spectral-resolution attosecond absorption spectroscopy of autoionization in xenon*, Phys. Rev. A **89**, 023408 (2014), URL https://link.aps.org/doi/10.1103/PhysRevA.89.023408.

[53] H. Niikura, F. Légaré, R. Hasbani, M. Y. Ivanov, D. M. Villeneuve, and P. B. Corkum, *Probing molecular dynamics with attosecond resolution using correlated wave packet pairs*, Nature **421**, 826 (2003), ISSN 1476-4687, URL https://doi.org/10.1038/nature01430.

[54] M. F. Kling, C. Siedschlag, A. J. Verhoef, J. I. Khan, M. Schultze, T. Uphues, Y. Ni, M. Uiberacker, M. Drescher, F. Krausz, et al., *Control of electron localization in molecular dissociation*, Science **312**, 246 (2006), ISSN 0036-8075, URL https://science.sciencemag.org/content/312/5771/246.

[55] A. Staudte, D. Pavičić, S. Chelkowski, D. Zeidler, M. Meckel, H. Niikura, M. Schöffler, S. Schössler, B. Ulrich, P. P. Rajeev, et al., *Attosecond strobing of two-surface population dynamics in dissociating* H_2^+, Phys. Rev. Lett. **98**, 073003 (2007), URL https://link.aps.org/doi/10.1103/PhysRevLett.98.073003.

[56] J. Schötz, B. Förg, M. Förster, W. A. Okell, M. I. Stockman, F. Krausz, P. Hommelhoff, and M. F. Kling, *Reconstruction of nanoscale near fields by attosecond streaking*, IEEE Journal of Selected Topics in Quantum Electronics **23**, 77 (2017), ISSN 1558-4542, URL https://doi.org/10.1109/JSTQE.2016.2625046.

[57] E. Saydanzad, J. Li, and U. Thumm, *Characterization of induced nanoplasmonic fields in time-resolved photoemission: A classical trajectory approach applied to gold nanospheres*, Phys. Rev. A **95**, 053406 (2017), URL https://link.aps.org/doi/10.1103/PhysRevA.95.053406.

[58] J. Li, E. Saydanzad, and U. Thumm, *Attosecond time-resolved streaked photoelectron spectroscopy of transition-metal nanospheres*, Phys. Rev. A **95**, 043423 (2017), URL https://link.aps.org/doi/10.1103/PhysRevA.95.043423.

[59] E. Saydanzad, J. Li, and U. Thumm, *Spatiotemporal imaging of plasmonic fields near nanoparticles below the diffraction limit*, Phys. Rev. A **98**, 063422 (2018), URL https://link.aps.org/doi/10.1103/PhysRevA.98.063422.

[60] J. Li, E. Saydanzad, and U. Thumm, *Imaging plasmonic fields with atomic spatiotemporal resolution*, Phys. Rev. Lett. **120**, 223903 (2018), URL https://link.aps.org/doi/10.1103/PhysRevLett.120.223903.

[61] L. Kasmi, M. Lucchini, L. Castiglioni, P. Kliuiev, J. Osterwalder, M. Hengsberger, L. Gallmann, P. Krüger, and U. Keller, *Effective mass effect in attosecond electron transport*, Optica **4**, 1492 (2017), URL http://www.osapublishing.org/optica/abstract.cfm?URI=optica-4-12-1492.

[62] M. J. Ambrosio and U. Thumm, *Energy-resolved attosecond interferometric photoemission from ag(111) and au(111) surfaces*, Phys. Rev. A **97**, 043431 (2018), URL https://link.aps.org/doi/10.1103/PhysRevA.97.043431.

[63] M. J. Ambrosio and U. Thumm, *Spatiotemporal analysis of a final-state shape resonance in interferometric photoemission from cu(111) surfaces*, Phys. Rev. A **100**, 043412 (2019), URL https://link.aps.org/doi/10.1103/PhysRevA.100.043412.

[64] M. Ossiander, J. Riemensberger, S. Neppl, M. Mittermair, M. Schäffer, A. Duensing, M. S. Wagner, R. Heider, M. Wurzer, M. Gerl, et al., *Absolute timing of the photo-*

electric effect, Nature **561**, 374 (2018), ISSN 1476-4687, URL https://doi.org/10.1038/s41586-018-0503-6.

[65] C.-H. Zhang and U. Thumm, *Probing dielectric-response effects with attosecond time-resolved streaked photoelectron spectroscopy of metal surfaces*, Phys. Rev. A **84**, 063403 (2011), URL https://link.aps.org/doi/10.1103/PhysRevA.84.063403.

[66] S. H. Chew, F. Süßmann, C. Späth, A. Wirth, J. Schmidt, S. Zherebtsov, A. Guggenmos, A. Oelsner, N. Weber, J. Kapaldo, et al., *Time-of-flight-photoelectron emission microscopy on plasmonic structures using attosecond extreme ultraviolet pulses*, Appl. Phys. Lett. **100**, 051904 (2012), URL https://doi.org/10.1063/1.3670324.

[67] M. Lupetti, J. Hengster, T. Uphues, and A. Scrinzi, *Attosecond photoscopy of plasmonic excitations*, Phys. Rev. Lett. **113**, 113903 (2014), URL https://link.aps.org/doi/10.1103/PhysRevLett.113.113903.

[68] M. Krüger, M. Schenk, M. Förster, and P. Hommelhoff, *Attosecond physics in photoemission from a metal nanotip*, Journal of Physics B: Atomic, Molecular and Optical Physics **45**, 074006 (2012), URL https://doi.org/10.1088%2F0953-4075%2F45%2F7%2F074006.

[69] A. L. Cavalieri, N. Müller, T. Uphues, V. S. Yakovlev, A. Baltuška, B. Horvath, B. Schmidt, L. Blümel, R. Holzwarth, S. Hendel, et al., *Attosecond spectroscopy in condensed matter*, Nature **449**, 1029 (2007), ISSN 1476-4687, URL https://doi.org/10.1038/nature06229.

[70] C. Lemell, B. Solleder, K. Tőkési, and J. Burgdörfer, *Simulation of attosecond streaking of electrons emitted from a tungsten surface*, Phys. Rev. A **79**, 062901 (2009), URL https://link.aps.org/doi/10.1103/PhysRevA.79.062901.

[71] Q. Liao and U. Thumm, *Initial-state, mean-free-path, and skin-depth dependence of attosecond time-resolved ir-streaked xuv photoemission from single-crystalline magne-*

sium, Phys. Rev. A **89**, 033849 (2014), URL https://link.aps.org/doi/10.1103/PhysRevA.89.033849.

[72] L. Miaja-Avila, C. Lei, M. Aeschlimann, J. L. Gland, M. M. Murnane, H. C. Kapteyn, and G. Saathoff, *Laser-assisted photoelectric effect from surfaces*, Phys. Rev. Lett. **97**, 113604 (2006), URL https://link.aps.org/doi/10.1103/PhysRevLett.97.113604.

[73] G. Saathoff, L. Miaja-Avila, M. Aeschlimann, M. M. Murnane, and H. C. Kapteyn, *Laser-assisted photoemission from surfaces*, Phys. Rev. A **77**, 022903 (2008), URL https://link.aps.org/doi/10.1103/PhysRevA.77.022903.

[74] M. J. Ambrosio and U. Thumm, *Comparative time-resolved photoemission from the cu(100) and cu(111) surfaces*, Phys. Rev. A **94**, 063424 (2016), URL https://link.aps.org/doi/10.1103/PhysRevA.94.063424.

[75] A. K. Kazansky and P. M. Echenique, *Time-dependent dynamical image screening at a metal surface*, Phys. Rev. B **81**, 193413 (2010), URL https://link.aps.org/doi/10.1103/PhysRevB.81.193413.

[76] B. Obreshkov and U. Thumm, *Neutralization of H^- near vicinal metal surfaces*, Phys. Rev. A **74**, 012901 (2006), URL https://link.aps.org/doi/10.1103/PhysRevA.74.012901.

[77] C.-H. Zhang and U. Thumm, *Electron-ion interaction effects in attosecond time-resolved photoelectron spectra*, Phys. Rev. A **82**, 043405 (2010), URL https://link.aps.org/doi/10.1103/PhysRevA.82.043405.

[78] D. M. Wolkow, *Über eine klasse von lösungen der diracschen gleichung*, Zeitschrift für Physik **94**, 250 (1935), ISSN 0044-3328, URL https://doi.org/10.1007/BF01331022.

[79] 'Free-Electron Lasers'. A collection of recent articles on FEL generation and characterization and their application in fundamental studies of light-matter interaction.

Nature Photonics Collection (January 23, 2019), URL https://www.nature.com/collections/cssxtbybyl.

[80] G. Mie, *Beiträge zur Optik trüber Medien, speziell kolloidaler Metallösungen*, Annalen der Physik **330**, 377 (1908), ISSN 1521-3889, URL http://dx.doi.org/10.1002/andp.19083300302.

[81] J. Stratton, *Electromagnetic theory*, vol. 33 (Wiley, 2007).

[82] E. Palik, ed., *Handbook of Optical Constants of Solids* (Elsevier Science, 1985), ISBN 9780080547213.

[83] H. Ehrenreich and H. R. Philipp, *Optical Properties of Ag and Cu*, Phys. Rev. **128**, 1622 (1962), URL http://link.aps.org/doi/10.1103/PhysRev.128.1622.

[84] H. Wang, F. Tam, N. K. Grady, and N. J. Halas, *Cu nanoshells: effects of interband transitions on the nanoparticle plasmon resonance*, The Journal of Physical Chemistry B **109**, 18218 (2005), pMID: 16853342, URL https://doi.org/10.1021/jp053863t.

[85] S. A. Maier, *Plasmonics: fundamentals and applications* (Springer Science & Business Media, 2007).

[86] S. Link and M. A. El-Sayed, *Size and temperature dependence of the plasmon absorption of colloidal gold nanoparticles*, The Journal of Physical Chemistry B **103**, 4212 (1999), URL https://doi.org/10.1021/jp984796o.

[87] U. Thumm, P. Kürpick, and U. Wille, *Size quantization effects in atomic level broadening near thin metallic films*, Phys. Rev. B **61**, 3067 (2000), URL https://link.aps.org/doi/10.1103/PhysRevB.61.3067.

[88] E. Merzbacher, *Quantum Mechanics* (Wiley, 1998), ISBN 9780471887027.

[89] W. M. Haynes, *CRC handbook of chemistry and physics* (CRC press, Boca Raton, FL, 2015), 95th ed.

[90] A. Sekiyama, J. Yamaguchi, A. Higashiya, M. Obara, H. Sugiyama, M. Y. Kimura, S. Suga, S. Imada, I. A. Nekrasov, M. Yabashi, et al., *The prominent 5d-orbital contribution to the conduction electrons in gold*, New Journal of Physics **12**, 043045 (2010), URL https://doi.org/10.1088%2F1367-2630%2F12%2F4%2F043045.

[91] S. Tanuma, C. J. Powell, and D. R. Penn, *Calculations of electron inelastic mean free paths. ix. data for 41 elemental solids over the 50 ev to 30 kev range*, Surface and Interface Analysis **43**, 689 (2011), URL https://onlinelibrary.wiley.com/doi/abs/10.1002/sia.3522.

[92] J. Stöhr, F. R. McFeely, G. Apai, P. S. Wehner, and D. A. Shirley, *Photoemission from cu valence bands using 50-175-ev synchrotron radiation*, Phys. Rev. B **14**, 4431 (1976), URL https://link.aps.org/doi/10.1103/PhysRevB.14.4431.

[93] M. I. Stockman, *Nanoplasmonics: The physics behind the applications*, Phys. Today **64**, 39 (2011).

[94] M. I. Stockman, *Nanoplasmonics: past, present, and glimpse into future*, Opt. Express **19**, 22029 (2011), URL http://www.opticsexpress.org/abstract.cfm?URI=oe-19-22-22029.

[95] W. Zhu, R. Esteban, A. G. Borisov, J. J. Baumberg, P. Nordlander, H. J. Lezec, J. Aizpurua, and K. B. Crozier, *Quantum mechanical effects in plasmonic structures with subnanometre gaps*, Nature Communications **7**, 11495 (2016), ISSN 2041-1723, URL https://doi.org/10.1038/ncomms11495.

[96] Y. Sun, B. Mayers, and Y. Xia, *Metal nanostructures with hollow interiors*, Advanced Materials **15**, 641 (2003), URL https://onlinelibrary.wiley.com/doi/abs/10.1002/adma.200301639.

[97] Y. Jin, *Multifunctional compact hybrid au nanoshells: A new generation of nanoplasmonic probes for biosensing, imaging, and controlled release*, Acc. Chem. Res. **47**, 138 (2014), ISSN 0001-4842, URL https://doi.org/10.1021/ar400086e.

[98] J. Li and U. Thumm, *A semi-classical approach for solving the time-dependent schrödinger equation in spatially inhomogeneous electromagnetic pulses*, Submitted (2019).

[99] M. Boiron and M. Lombardi, *Complex trajectory method in semiclassical propagation of wave packets*, J. Chem. Phys. **108**, 3431 (1998), URL https://doi.org/10.1063/1.475743.

[100] Y. Goldfarb, J. Schiff, and D. J. Tannor, *Complex trajectory method in time-dependent wkb*, J. Chem. Phys. **128**, 164114 (2008), URL https://doi.org/10.1063/1.2907336.

[101] H. Goldstein, C. Poole, and J. Safko, *Classical mechanics* (Addison-wesley, 2001), 3rd ed., ISBN 9780201657029.

[102] C. G. Broyden, *A class of methods for solving nonlinear simultaneous equations*, Mathematics of Computation **19**, 577 (1965), ISSN 00255718, 10886842, URL http://www.jstor.org/stable/2003941.

[103] K. E. Atkinson, *An introduction to numerical analysis* (John Wiley & Sons, 2008).

[104] G. K. Batchelor, *An introduction to fluid dynamics* (Cambridge University Press, 1967).

[105] L. D. Landau and E. M. Lifshitz, *Quantum mechanics: non-relativistic theory* (Elsevier, 1977), 3rd ed., ISBN 0-08-020940-8.

[106] L. Rosenberg and F. Zhou, *Generalized volkov wave functions: Application to laser-assisted scattering*, Phys. Rev. A **47**, 2146 (1993), URL https://link.aps.org/doi/10.1103/PhysRevA.47.2146.

[107] H. R. Reiss and V. P. Krainov, *Approximation for a coulomb-volkov solution in strong fields*, Phys. Rev. A **50**, R910 (1994), URL https://link.aps.org/doi/10.1103/PhysRevA.50.R910.

[108] P. A. Macri, J. E. Miraglia, and M. S. Gravielle, *Ionization of hydrogen targets by short laser pulses*, J. Opt. Soc. Am. B **20**, 1801 (2003), URL http://josab.osa.org/abstract.cfm?URI=josab-20-9-1801.

[109] J. Dubois, S. A. Berman, C. Chandre, and T. Uzer, *Inclusion of coulomb effects in laser-atom interactions*, Phys. Rev. A **99**, 053405 (2019), URL https://link.aps.org/doi/10.1103/PhysRevA.99.053405.

[110] S. Patchkovskii and H. Muller, *Simple, accurate, and efficient implementation of 1-electron atomic time-dependent schrödinger equation in spherical coordinates*, Comp. Phys. Commun. **199**, 153 (2016), ISSN 0010-4655, URL http://www.sciencedirect.com/science/article/pii/S001046551500394X.

[111] R. W. Boyd, Z. Shi, and I. D. Leon, *The third-order nonlinear optical susceptibility of gold*, Optics Communications **326**, 74 (2014), ISSN 0030-4018, URL http://www.sciencedirect.com/science/article/pii/S0030401814002351.

[112] R. W. Boyd, *Nonlinear optics* (Academic Press, 2008), ISBN 9780123694706.

[113] S. Palomba, M. Danckwerts, and L. Novotny, *Nonlinear plasmonics with gold nanoparticle antennas*, Journal of Optics A: Pure and Applied Optics **11**, 114030 (2009), URL https://doi.org/10.1088%2F1464-4258%2F11%2F11%2F114030.

[114] J. A. Powell, A. M. Summers, Q. Liu, S. J. Robatjazi, P. Rupp, J. Stierle, C. Trallero-Herrero, M. F. Kling, and A. Rudenko, *Interplay of pulse duration, peak intensity, and particle size in laser-driven electron emission from silica nanospheres*, Opt. Express **27**, 27124 (2019), URL http://www.opticsexpress.org/abstract.cfm?URI=oe-27-19-27124.

[115] P. B. Johnson and R. W. Christy, *Optical Constants of the Noble Metals*, Phys. Rev. B **6**, 4370 (1972), URL https://link.aps.org/doi/10.1103/PhysRevB.6.4370.

[116] N. Bloembergen, W. Burns, and M. Matsuoka, *Reflected third harmonic generated by*

picosecond laser pulses, Optics Communications **1**, 195 (1969), ISSN 0030-4018, URL http://www.sciencedirect.com/science/article/pii/0030401869900649.

[117] E. Hecht, *Optics* (Reading, Mass. : Addison-Wesley, Reading, Mass., 2002), 4th ed.

Appendix A

Mathematical derivation of plasmonic field reconstruction

In this appendix, we present the detailed mathematical derivation of several key equations in Chapter 3.

A.1 Evaluation of the spatial integral in Eq. (3.3)

The amplitudes of the initial states $\Psi_i(\mathbf{r})$ decay exponentially outside of the nanosphere, and the amplitudes of the final state $\Psi^{\tau}_{\mathbf{k}_f}(\mathbf{r}, t_z)$ vanish exponentially inside the nanoparticle due to the damping factor $f(l;\kappa) = exp[-l/(2\kappa)]$. The spatial integral in Eq. (3.3) is thus confined within a range of several atomic units near the nanosphere surface which is located at a distance R of the order 10^3 a.u. from the center of the sphere. The photoelectron-energy range in the discussion, lying between $\sim$ 25 and $\sim$ 60 eV, then implies that the condition $k_f r \gg 1$ is satisfied, allowing the plane-wave factor in Eq. (2.11) to be approximated by its asymptotic form [88],

$$e^{i\mathbf{k}_f\cdot\mathbf{r}} \approx \frac{2\pi\ e^{ik_f r}}{ik_f r}\delta(\hat{\mathbf{n}}-\hat{\mathbf{r}}) - \frac{2\pi\ e^{-ik_f r}}{ik_f r}\delta(\hat{\mathbf{n}}+\hat{\mathbf{r}}). \tag{A.1}$$

The transition amplitude (3.3) is thus approximately given by the 1-dimensional integral

$$T_i(\mathbf{k}_f,\tau) \approx \frac{\sqrt{2}\pi E_X}{\omega_X}\hat{\mathbf{x}}^{lab}\cdot\int dr\; r^2\Big[\nabla\Psi_i(\hat{\mathbf{n}}r)\Big]f[l(\hat{\mathbf{n}}r);\kappa)] \times \frac{e^{-ik_f r-i\phi^\tau_{\mathbf{k}_f}(\hat{\mathbf{n}}r,t_z)}}{k_f r}\,\frac{1}{b^\tau_{\mathbf{k}_f}(\hat{\mathbf{n}}r,t_z)} \times \exp\left\{-\left[\frac{\frac{\partial}{\partial t_z}\phi^\tau_{\mathbf{k}_f}(\hat{\mathbf{n}}r,t_z)+\omega_X+\omega_i}{2b^\tau_{\mathbf{k}_f}(\hat{\mathbf{n}}r,t_z)}\right]^2\right\}, \tag{A.2}$$

where the ∇ operator does not act beyond the square bracket. Note that the second term in Eq. (A.1) does not contribute to the spatial integral since the damping factor $f(l;\kappa)$ prevents electrons from traversing the nanoparticle with noticeable transmitted amplitude.

The factor $\big[\nabla\Psi_i(\hat{\mathbf{n}}r)\big]f[l(\hat{\mathbf{n}}r);\kappa)]$ vanishes exponentially inside and outside the nanoparticle, selectively enhancing contribution near the surface at $r=R$. Therefore, replacing this term by a factor proportional to $\delta(r-R)$ in Eq. (A.2) permits the radial integral to be approximated as given by Eqs. (3.5) and (3.6) of the main text, i.e., by

$$T_i(\mathbf{k}_f,\tau) \approx C_i\frac{\sqrt{2}\pi E_X R\; e^{-ik_f R-i\phi^\tau_{\mathbf{k}_f}(\hat{\mathbf{n}}R,\tilde{t}_z)}}{\omega_X k_f\; b^\tau_{\mathbf{k}_f}(\hat{\mathbf{n}}R,\tilde{t}_z)} \times \exp\left\{-\left[\frac{\frac{\partial}{\partial t_z}\phi^\tau_{\mathbf{k}_f}(\hat{\mathbf{n}}R,\tilde{t}_z)+\omega_X+\omega_i}{2b^\tau_{\mathbf{k}_f}(\hat{\mathbf{n}}R,\tilde{t}_z)}\right]^2\right\}, \tag{A.3}$$

with $\tilde{t}_z = R\cos\theta/c$ and

$$C_i = \int dr\Big[\hat{\mathbf{x}}^{lab}\cdot\nabla\Psi_i(\hat{\mathbf{n}}r)\Big]\; f[l(\hat{\mathbf{n}}r);\kappa]. \tag{A.4}$$

A.2 Evaluation of Eq. (3.11)

A spherical square well of radius $R = 50$ nm and depth $V_0 = -13.1$ eV, binds approximately 3 million states below Fermi level at $-W_f = -5.1$ eV, resulting in a quasi-continuum of conduction-band states with a density of states that is proportional to $\sqrt{\omega_i - V_0}$. The incoherent sum over occupied initial states in the photoemission-probability distribution in

Eq. (3.2) can therefore be converted to the integral

$$P(\mathcal{E}_f)\big|_{\tau,\hat{\mathbf{n}}} \approx \frac{1}{N}\int_{V_0}^{V_0+\sigma_c} d\omega_i \sqrt{\omega_i - V_0}\; P_i(\mathcal{E}_f)\Bigg|_{\tau,\hat{\mathbf{n}}}. \tag{A.5}$$

with contributions to the photoemission probability from each individual occupied state

$$\begin{aligned} P_i(\mathcal{E}_f)\big|_{\tau,\hat{\mathbf{n}}} \approx & \frac{\left|\pi C_i E_X R/\omega_X\right|^2 \mathcal{E}_f^{-3/2}}{\sqrt{8(\ln 2)^2/\tau_X^4 + \mathcal{E}_f E_{tot}^2(\hat{\mathbf{n}}R, \tilde{t}_z + \tau)}} \\ & \times \exp\left\{ - \frac{\left[\mathcal{E}_f + \sqrt{2\mathcal{E}_f} A_{tot}(\hat{\mathbf{n}}R, \tilde{t}_z + \tau) - \omega_X - \omega_i\right]^2}{\sqrt{16(\ln 2)^2/\tau_X^4 + 2\mathcal{E}_f E_{tot}^2(\hat{\mathbf{n}}R, \tilde{t}_z + \tau)}} \right\}. \end{aligned} \tag{A.6}$$

This results allows us to write the first line in the center of energy (CoE) of the photoelectron streaking trace (Eq. (3.11) in the main text) as

$$\begin{aligned} \overline{\mathcal{E}_f}(\tau)\big|_{\hat{\mathbf{n}}} &\approx \frac{\int d\mathcal{E}_f\; \mathcal{E}_f \int_{V_0}^{V_0+\sigma_c} d\omega_i \sqrt{\omega_i - V_0} P_i(\mathcal{E}_f)}{\int d\mathcal{E}_f \int_{V_0}^{V_0+\sigma_c} d\omega_i \sqrt{\omega_i - V_0} P_i(\mathcal{E}_f)}\Bigg|_{\tau,\hat{\mathbf{n}}} \\ &= \frac{\int_{V_0}^{V_0+\sigma_c} d\omega_i \sqrt{\omega_i - V_0} \int d\mathcal{E}_f\; \mathcal{E}_f P_i(\mathcal{E}_f)}{\int_{V_0}^{V_0+\sigma_c} d\omega_i \sqrt{\omega_i - V_0} \int d\mathcal{E}_f P_i(\mathcal{E}_f)}\Bigg|_{\tau,\hat{\mathbf{n}}}. \end{aligned} \tag{A.7}$$

A.2.1 Simplification of Eq. (A.6)

For a typical single attosecond pulse with a temporal FWHIM of $\sim 10^2$ as, the term $16(\ln 2)^2/\tau_X^4$ in Eq. (A.6) is equal to 1.64×10^{-3} a.u. In comparison, for photoelectron energies $\mathcal{E}_f \sim 1$ a.u. and IR intensity $I = 10^{11}\mathrm{W/cm^2}$ assumed in the main text, the term $2\mathcal{E}_f E_{tot}^2(\hat{\mathbf{n}}R, \tilde{t}_z + \tau) \sim 10^{-5}$ a.u. in Eq. (A.6) is two orders of magnitude smaller, allowing us to approximate

$$\sqrt{16(\ln 2)^2/\tau_X^4 + 2\mathcal{E}_f E_{tot}^2(\hat{\mathbf{n}}R, \tilde{t}_z + \tau)} \approx 4\ln 2/\tau_X^2, \tag{A.8}$$

such that Eq. (A.6) can be expressed with a Gaussian exponential factor in the final photoelectron energy,

$$P_i(\mathcal{E}_f)\big|_{\tau,\hat{\mathbf{n}}} \approx \frac{\left|\pi C_i E_X R/\omega_X\right|^2 \mathcal{E}_f^{-3/2}}{2\sqrt{2}\ln 2/\tau_X^2} \times \exp\left\{ -\frac{\left[\mathcal{E}_f + \sqrt{2\mathcal{E}_f} A_{tot}(\hat{\mathbf{n}}R, \tilde{t}_z + \tau) - \omega_X - \omega_i\right]^2}{4\ln 2/\tau_X^2} \right\}. \tag{A.9}$$

The center $\langle \mathcal{E}_f(\tau;\omega_i)\rangle\big|_{\hat{\mathbf{n}}}$ of the above exponential term is given as the zero of the function

$$g(\mathcal{E}_f)\big|_{\tau,\hat{\mathbf{n}}} = \mathcal{E}_f + \sqrt{2\mathcal{E}_f} A_{tot}(\hat{\mathbf{n}}R, \tilde{t}_z + \tau) - \omega_X - \omega_i, \tag{A.10}$$

or

$$\langle \mathcal{E}_f(\tau;\omega_i)\rangle\big|_{\hat{\mathbf{n}}} = -\sqrt{2\langle \mathcal{E}_f(\tau;\omega_i)\rangle\big|_{\hat{\mathbf{n}}}} A_{tot}(\hat{\mathbf{n}}R, \tilde{t}_z + \tau) + \omega_X + \omega_i. \tag{A.11}$$

Taylor expansion of $g(\mathcal{E}_f)\big|_{\tau,\hat{\mathbf{n}}}$ in terms of the dimensionless parameter

$$\delta = \frac{\mathcal{E}_f - \langle \mathcal{E}_f(\tau;\omega_i)\rangle}{\langle \mathcal{E}_f(\tau;\omega_i)\rangle} \tag{A.12}$$

near $\langle \mathcal{E}_f(\tau;\omega_i)\rangle$ yields

$$g(\mathcal{E}_f)\big|_{\tau,\hat{\mathbf{n}}} = \langle \mathcal{E}_f(\tau;\omega_i)\rangle \left\{ \left[1 + \frac{A_{tot}(\hat{\mathbf{n}}R, \tilde{t}_z + \tau)}{\sqrt{2\langle \mathcal{E}_f(\tau;\omega_i)\rangle}}\right]\delta + \sqrt{\pi}\, \frac{A_{tot}(\hat{\mathbf{n}}R, \tilde{t}_z + \tau)}{\sqrt{2\langle \mathcal{E}_f(\tau;\omega_i)\rangle}} \sum_{j=2}^{\infty} \frac{\delta^j}{j!\ \Gamma(3/2 - j)} \right\}\Bigg|_{\hat{\mathbf{n}}}. \tag{A.13}$$

For the delay range and initial-state energies ω_i relevant in this work, and for all detection angles ω_i, $\langle \mathcal{E}_f(\tau;\omega_i)\rangle\big|_{\hat{\mathbf{n}}} \sim 1$ a.u.. However, $|\mathcal{E}_f - \langle \mathcal{E}_f(\tau;\omega_i)\rangle|$ is effectively limited by the XUV spectral width $2ln2/\tau_X = 0.168$ a.u., as expressed in the denominator of the exponent in Eq. (A.9). Thus, $|\delta|$ is $\sim 10^{-1}$ or smaller. Furthermore, the amplitude of $A_{tot}(\hat{\mathbf{n}}R, \tilde{t}_z + \tau)$ is about $\sim 10^{-1}$ a.u. for a 10^{11}W/cm^2 IR pulse, which means

that $|A_{tot}(\hat{\mathbf{n}}R, \tilde{t}_z + \tau) \Big/ \sqrt{2\langle \mathcal{E}_f(\tau;\omega_i)\rangle}|$ is at the most about 10^{-1}. The first-order term in Eq. (A.13) thus dominates all higher-order terms by at least two orders of magnitude, justifying the truncation of Eq. (A.13) after the first-order term.

Keeping only the first-order term in Eq. (A.13) transforms the exponential factor in Eq. (A.9) into a Gaussian distribution, casting Eq. (A.9) into the form

$$P_i(\mathcal{E}_f)\big|_{\tau,\hat{\mathbf{n}}} \approx \frac{\left|\pi C_i E_X R/\omega_X\right|^2 \mathcal{E}_f^{-3/2}}{2\sqrt{2}\ln 2/\tau_X^2} * \exp\left\{ -\Big[\mathcal{E}_f - \langle \mathcal{E}_f(\tau;\omega_i)\rangle\Big]^2 \Big/ \left[\frac{4\ln 2\sqrt{2\langle \mathcal{E}_f(\tau;\omega_i)\rangle}\,\Big/\tau_X^2}{\sqrt{2\langle \mathcal{E}_f(\tau;\omega_i)\rangle} + A_{tot}(\hat{\mathbf{n}}R, \tilde{t}_z + \tau)}\right]\right\}\Bigg|_{\hat{\mathbf{n}}}. \quad \text{(A.14)}$$

A.2.2 Integration over $\mathcal{E}_f$ in Eq. (A.7)

In our numerical application, the pre-exponential factor ($\backsim \mathcal{E}_f^{-3/2}$) does not vary significantly over the width of the Gaussian exponential in Eq. (A.14). This justifies a '*peaking approximation*' that consists in replacing $\mathcal{E}_f^{-3/2}$ in the pre-exponential factor in Eq. (A.14) by its value $\langle \mathcal{E}_f(\tau;\omega_i)\rangle^{-3/2}$ at the central energy. This results in the Gaussian distribution centered at $\langle \mathcal{E}_f(\tau;\omega_i)\rangle$

$$P_i(\mathcal{E}_f)\big|_{\tau,\hat{\mathbf{n}}} \approx \frac{\left|\pi C_i E_X R/\omega_X\right|^2 \langle \mathcal{E}_f(\tau;\omega_i)\rangle^{-3/2}}{2\sqrt{2}\ln 2/\tau_X^2} * \exp\left\{ -\Big[\mathcal{E}_f - \langle \mathcal{E}_f(\tau;\omega_i)\rangle\Big]^2 \Big/ \left[\frac{4\ln 2\sqrt{2\langle \mathcal{E}_f(\tau;\omega_i)\rangle}\,\Big/\tau_X^2}{\sqrt{2\langle \mathcal{E}_f(\tau;\omega_i)\rangle} + A_{tot}(\hat{\mathbf{n}}R, \tilde{t}_z + \tau)}\right]\right\}\Bigg|_{\hat{\mathbf{n}}}. \quad \text{(A.15)}$$

The two integrals over $\mathcal{E}_f$ in Eq. (A.7) can now be conveniently evaluated analytically as

the lowest two moments (of order zero and one) of a Gaussian distribution, with the result

$$\begin{aligned}\overline{\mathcal{E}_f}(\tau)\big|_{\hat{\mathbf{n}}} &= \frac{\int_{V_0}^{V_0+\sigma_c} d\omega_i \sqrt{\omega_i - V_0}\, \big\langle \mathcal{E}_f(\tau;\omega_i)\big\rangle\Big|_{\hat{\mathbf{n}}}}{\int_{V_0}^{V_0+\sigma_c} d\omega_i \sqrt{\omega_i - V_0}} \\ &= \frac{3}{2\sigma_c^{3/2}} \int_{V_0}^{V_0+\sigma_c} d\omega_i \sqrt{\omega_i - V_0}\, \big\langle \mathcal{E}_f(\tau;\omega_i)\big\rangle\Big|_{\hat{\mathbf{n}}} \\ &= \Big\lceil \big\langle \mathcal{E}_f(\tau;\omega_i)\big\rangle \Big\rfloor\Big|_{\hat{\mathbf{n}}}. \end{aligned} \tag{A.16}$$

The CoE of the photoelectron-streaking trace is now seen to be equal to central energy $\big\langle \mathcal{E}_f(\tau;\omega_i)\big\rangle$, averaged over the occupied initial-state energies ω_i. The averaging over ω_i is denoted by the brackets $\lceil\ \rfloor$ and evaluated in the following subsection.

A.2.3 Integration over the initial-state energy

The combination of Eq. (A.11) and (A.16) results in

$$\begin{aligned}\overline{\mathcal{E}_f}(\tau)\big|_{\hat{\mathbf{n}}} &= \frac{3}{2\sigma_c^{3/2}} \int_{V_0}^{V_0+\sigma_c} d\omega_i \sqrt{\omega_i - V_0} \Big[\omega_X + \omega_i - \sqrt{2\big\langle \mathcal{E}_f(\tau;\omega_i)\big\rangle} A_{tot}(\hat{\mathbf{n}}R, \tilde{t}_z + \tau)\Big]\Big|_{\hat{\mathbf{n}}} \\ &= \omega_X + V_0 + \frac{3}{5}\sigma_c - A_{tot}(\hat{\mathbf{n}}R, \tilde{t}_z + \tau) \Big\lceil \sqrt{2\big\langle \mathcal{E}_f(\tau;\omega_i)\big\rangle} \Big\rfloor\Big|_{\hat{\mathbf{n}}}, \end{aligned} \tag{A.17}$$

where,

$$\Big\lceil \sqrt{2\big\langle \mathcal{E}_f(\tau;\omega_i)\big\rangle} \Big\rfloor\Big|_{\hat{\mathbf{n}}} = \frac{3\int_{V_0}^{V_0+\sigma_c} d\omega_i \sqrt{\omega_i - V_0}\, \sqrt{2\big\langle \mathcal{E}_f(\tau;\omega_i)\big\rangle}}{2\sigma_c^{3/2}}\Big|_{\hat{\mathbf{n}}}. \tag{A.18}$$

Taylor expansion of $\sqrt{2\big\langle \mathcal{E}_f(\tau;\omega_i)\big\rangle}\big|_{\hat{\mathbf{n}}}$ as a function of $\big\langle \mathcal{E}_f(\tau;\omega_i)\big\rangle\big|_{\hat{\mathbf{n}}}$ about $\Big\lceil \big\langle \mathcal{E}_f(\tau;\omega_i)\big\rangle \Big\rfloor\Big|_{\hat{\mathbf{n}}} = \overline{\mathcal{E}_f}(\tau)\big|_{\hat{\mathbf{n}}}$, in conjunction with Eq. (A.16) leads to

$$\sqrt{2\big\langle \mathcal{E}_f(\tau;\omega_i)\big\rangle} = \sum_{j=0}^{\infty} \frac{\sqrt{2\pi\overline{\mathcal{E}_f}(\tau)}}{j!\ \Gamma(3/2-j)} * \left\{ \frac{\big\langle \mathcal{E}_f(\tau;\omega_i)\big\rangle - \overline{\mathcal{E}_f}(\tau)}{\overline{\mathcal{E}_f}(\tau)} \right\}^j \Bigg|_{\hat{\mathbf{n}}}. \tag{A.19}$$

Since $\overline{\mathcal{E}_f}(\tau)\big|_{\hat{\mathbf{n}}} \sim 1$ a.u. and, by solving Eq. (A.11) $\left|\langle\mathcal{E}_f(\tau;\omega_i)\rangle - \overline{\mathcal{E}_f}(\tau)\right|\Big|_{\hat{\mathbf{n}}} \sim \sigma_c \sim 10^{-1}$ a.u., the second order-term in (A.19) is two orders of magnitudes smaller than the zeroth-order term. This allows us to truncate after the first-order term to obtain first

$$\sqrt{2\langle\mathcal{E}_f(\tau;\omega_i)\rangle} \approx \sqrt{2\overline{\mathcal{E}_f}(\tau)} + \left.\frac{\langle\mathcal{E}_f(\tau;\omega_i)\rangle - \overline{\mathcal{E}_f}(\tau)}{\sqrt{2\overline{\mathcal{E}_f}(\tau)}}\right|_{\hat{\mathbf{n}}}, \tag{A.20}$$

and next, from Eq. (A.18),

$$\begin{aligned}\left[\sqrt{2\langle\mathcal{E}_f(\tau;\omega_i)\rangle}\right]\Big|_{\hat{\mathbf{n}}} &= \frac{3}{2\sigma_c^{3/2}}\int_{V_0}^{V_0+\sigma_c} d\omega_i\sqrt{\omega_i - V_0}\times\left\{\sqrt{2\overline{\mathcal{E}_f}(\tau)} + \frac{\langle\mathcal{E}_f(\tau;\omega_i)\rangle - \overline{\mathcal{E}_f}(\tau)}{\sqrt{2\overline{\mathcal{E}_f}(\tau)}}\right\}\Big|_{\hat{\mathbf{n}}} \\ &= \sqrt{2\overline{\mathcal{E}_f}(\tau)}\,\Big|_{\hat{\mathbf{n}}}.\end{aligned} \tag{A.21}$$

Equation Eq. (A.17) can now be written as

$$\overline{\mathcal{E}_f}(\tau)\big|_{\hat{\mathbf{n}}} = \omega_X + V_0 + \frac{3}{5}\sigma_c - A_{tot}(\hat{\mathbf{n}}R, \tilde{t}_z + \tau)\sqrt{2\overline{\mathcal{E}_f}(\tau)}\,\Big|_{\hat{\mathbf{n}}}, \tag{A.22}$$

which is Eq. (3.11) in the main text. Finally, by inverting Eq. (A.22) we retrieve the plasmonically enhanced electric field at the position $\hat{\mathbf{n}}$ at the nanosphere surface at time t from the streaked photoelectron spectra,

$$E_{tot}(\hat{\mathbf{n}}R, t) = \frac{\partial}{\partial t}\left.\frac{\overline{\mathcal{E}_f}(t - R\cos\theta/c) - \omega_X - (3/5)\sigma_c - V_0}{\sqrt{2\overline{\mathcal{E}_f}(t - R\cos\theta/c)}}\right|_{\hat{\mathbf{n}}}, \tag{A.23}$$

which is Eq. (3.12) in the main text.

Appendix B

Mathematical derivation and comments on three applications of the ACCTIVE method

B.1 Derivation of Eq. (4.19)

We here derive the Volkov wavefunction Eq. (4.19) using ACCTIVE. Starting from the potentials and initial wavefunction in Eq. (4.18), the velocity field along the classical trajectory $\tilde{\mathbf{r}}(t)$ is

$$\mathbf{v}(\mathbf{r},t) = \frac{\mathbf{p}}{m} + \frac{q}{m}\int_{t_0}^{t} \mathbf{E}(t')dt' = \frac{\mathbf{p} - q\mathbf{A}(t)}{m}. \tag{B.1}$$

Therefore,

$$\tilde{\mathbf{r}}(t) = \mathbf{r}_0 + \int_{t_0}^{t} \left[\frac{\mathbf{p} - q\mathbf{A}(t)}{m}\right] dt', \tag{B.2}$$

$$\nabla \cdot \mathbf{v}(\mathbf{r},t) = 0, \tag{B.3}$$

and Eq. (4.16), applied to the example in Sec. 4.2.1, becomes

$$\begin{aligned}
\Psi(\mathbf{r},t) &= \exp\left\{\frac{i\mathbf{p}\cdot\mathbf{r}_0}{\hbar} + \frac{i}{\hbar}\int_{t_0}^{t}\left[\frac{m}{2}\left(\frac{\mathbf{p}-q\mathbf{A}(t')}{m}\right)^2 + q\left(\frac{\mathbf{p}-q\mathbf{A}(t')}{m}\right)\cdot\mathbf{A}(t')\right]dt'\right\} \\
&= \exp\left\{\frac{i\mathbf{p}}{\hbar}\cdot\left[\mathbf{r} - \int_{t_0}^{t}\left(\frac{\mathbf{p}-q\mathbf{A}(t)}{m}\right)dt'\right]\right. \\
&\qquad \left. + \frac{i}{\hbar}\int_{t_0}^{t}\left[\frac{m}{2}\left(\frac{\mathbf{p}-q\mathbf{A}(t')}{m}\right)^2 + q\left(\frac{\mathbf{p}-q\mathbf{A}(t')}{m}\right)\cdot\mathbf{A}(t')\right]dt'\right\} \\
&= \exp\left\{\frac{i\mathbf{p}\cdot\mathbf{r}}{\hbar} + \frac{i}{\hbar}\int_{t_0}^{t}\left[\frac{m}{2}\left(\frac{\mathbf{p}-q\mathbf{A}(t')}{m}\right)^2 - m\left(\frac{\mathbf{p}-q\mathbf{A}(t')}{m}\right)^2\right]dt'\right\} \\
&= \exp\left\{\frac{i\ \mathbf{p}\cdot\mathbf{r}}{\hbar} - \frac{i}{2m\hbar}\int_{t_0}^{t}\left[\mathbf{p}-q\mathbf{A}(t')\right]^2 dt'\right\},
\end{aligned} \tag{B.4}$$

which is the Volkov wavefunction Eq. (4.19).

B.2 Numerical calculation of Coulomb wavefunctions using ACCTIVE

The ACCTIVE method links a quantum-mechanical problem of obtaining wavefunctions $\Psi(\mathbf{r},t)$ to a classical problem of determining velocity fields $\mathbf{v}(\mathbf{r},t)$. However, in some cases, e.g., for Coulomb wavefunctions, such velocity fields are not uniquely defined (Fig. B.1). This can result in interference patterns in the obtained wavefunctions, as pointed out by Goldfarb *et al.* [100].

For each event $(\mathbf{r},t)$, two possible classical trajectories can be found to satisfy the same boundary condition of an outgoing plane wave in Eq. (4.21), as shown in Fig. B.1. Goldfarb *et al.* [100] take this interference into account by approximating the wavefunction as the superposition of contributions from different trajectories,

$$\Psi(\mathbf{r},t) \approx \sum_l \exp\left[\frac{i}{\hbar}S^l\big(\tilde{\mathbf{r}}(t),t\big)\right], \tag{B.5}$$

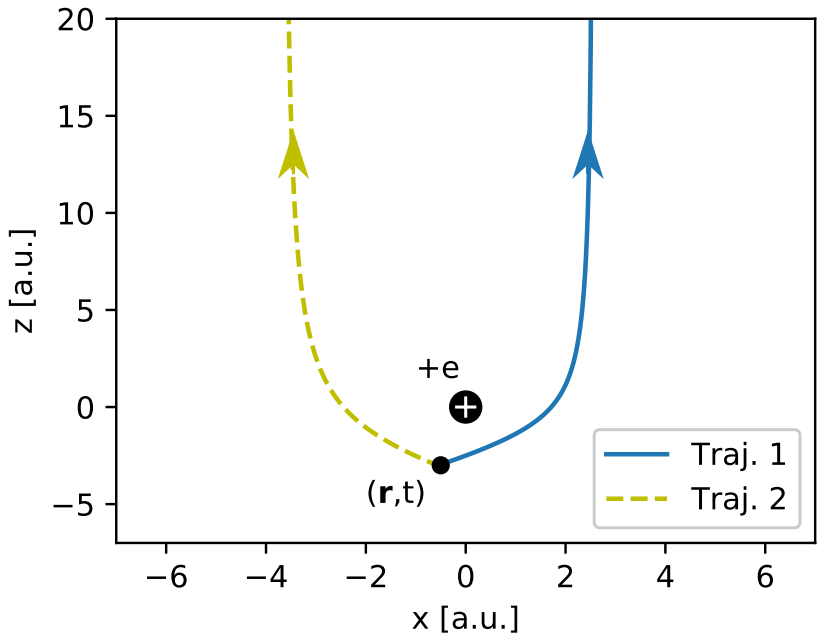


Figure B.1: *Two possible classical trajectories passing through* $(\boldsymbol{r}, t)$ *satisfying the same outgoing plane wave boundary condition.*

where each action $S^l(\mathbf{r}, t)$ is associated with a trajectory $\tilde{\mathbf{r}}^l(t)$. In this work, we follow a different and simpler approach.

The TDSE is a linear partial differential equation. Its solution can be expressed as the superposition of a set of linearly independent basis functions $\Psi^l(\mathbf{r}, t)$,

$$\Psi(\mathbf{r}, t) = \sum_l C^l \Psi^l(\mathbf{r}, t) = \sum_l C^l \exp\left[\frac{i}{\hbar} S^l\big(\mathbf{r}, t\big)\right], \tag{B.6}$$

where each $S^l(\mathbf{r}, t)$ is uniquely determined by a velocity field $\mathbf{v}^l(\mathbf{r}, t)$ and the coefficients C^l are obtained from the initial condition,

$$\Psi_0(\mathbf{r}) = \sum_l C^l \Psi^l(\mathbf{r}, t_0). \tag{B.7}$$

Since two possible trajectories can be obtained for each given event $(\mathbf{r}, t)$, we can find

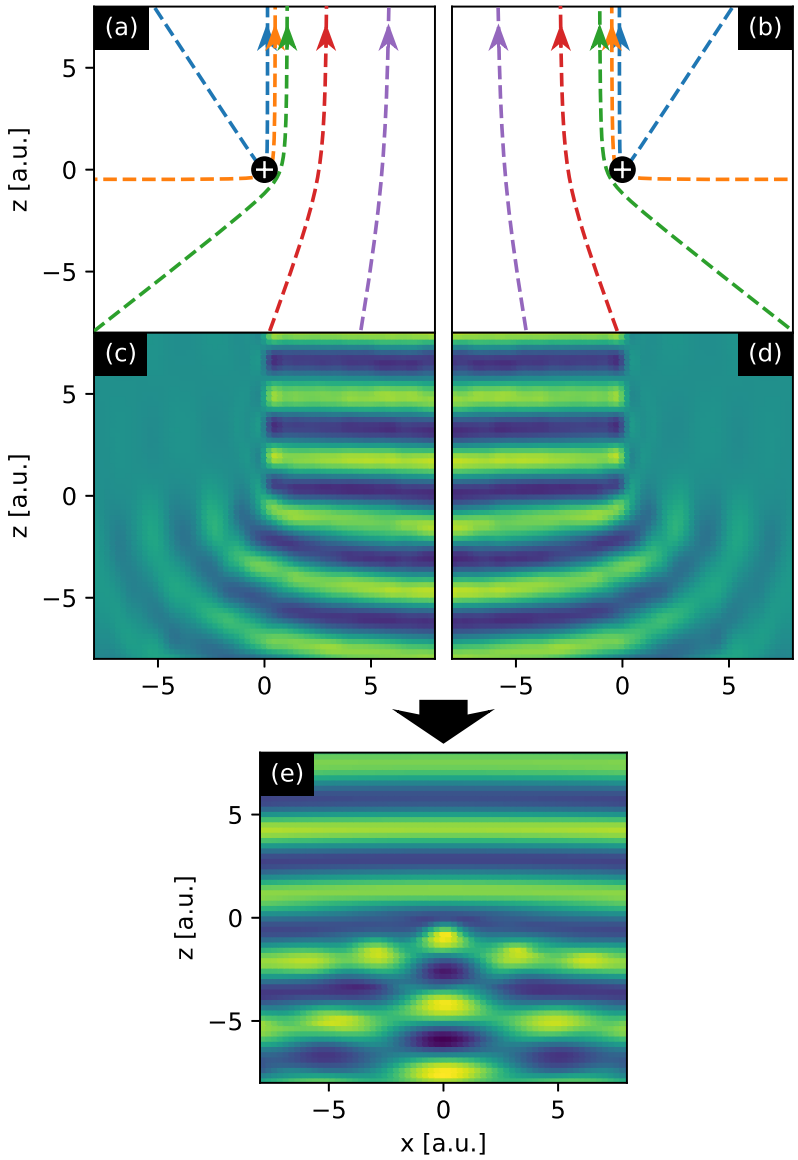


Figure B.2: *Two possible velocity fields (a)* $\boldsymbol{v}^{+}(\boldsymbol{r},t)$*, and (b)* $\boldsymbol{v}^{-}(\boldsymbol{r},t)$*. (c)* $\Psi^{+}(\boldsymbol{r},t)$ *and (d)* $\Psi^{-}(\boldsymbol{r},t)$ *are the real parts of the corresponding 1st order ACCTIVE wavefunctions at* $y=0$ *plane, respectively, and (d)* $\Psi(\boldsymbol{r},t)$ *is the linear combination of these two wavefunctions.*

two velocity fields, $\mathbf{v}^+(\mathbf{r},t)$ and $\mathbf{v}^-(\mathbf{r},t)$, which are defined by

$$\mathbf{v}^+(\mathbf{r},t) \xrightarrow{z\to+\infty,\ x>0} \hat{\mathbf{z}}p/m \tag{B.8a}$$

$$\mathbf{v}^-(\mathbf{r},t) \xrightarrow{z\to+\infty,\ x<0} \hat{\mathbf{z}}p/m, \tag{B.8b}$$

as illustrated in Fig. B.2(a) and B.2(b), respectively. Figures B.2(c) and B.2(d) show the calculated 1st-order ACCTIVE wavefunctions, $\Psi^+(\mathbf{r},t)$ and $\Psi^-(\mathbf{r},t)$, associated with these two velocity fields at $t=0$. Numerical calculation shows that,

$$\Psi^+(\mathbf{r},t) \xrightarrow{z\to+\infty} \begin{cases} e^{ikz} & x>0 \\ 0 & x<0 \end{cases} \tag{B.9a}$$

$$\Psi^-(\mathbf{r},t) \xrightarrow{z\to+\infty} \begin{cases} e^{ikz} & x<0 \\ 0 & x>0 \end{cases}. \tag{B.9b}$$

Therefore, at t_0, $\Psi_0(\mathbf{r}) = \Psi(\mathbf{r},0)$ can be written as the linear combination of $\Psi^+(\mathbf{r},t_0)$ and $\Psi^-(\mathbf{r},t_0)$ and satisfies the boundary condition (B.8),

$$\Psi_0(\mathbf{r}) = \Psi^+(\mathbf{r},t_0) + \Psi^-(\mathbf{r},t_0). \tag{B.10}$$

The wavefunction at any given time t is then obtained with the same coefficients,

$$\Psi(\mathbf{r},t) = \Psi^+(\mathbf{r},t) + \Psi^-(\mathbf{r},t), \tag{B.11}$$

as shown in Fig. B.2 (e).

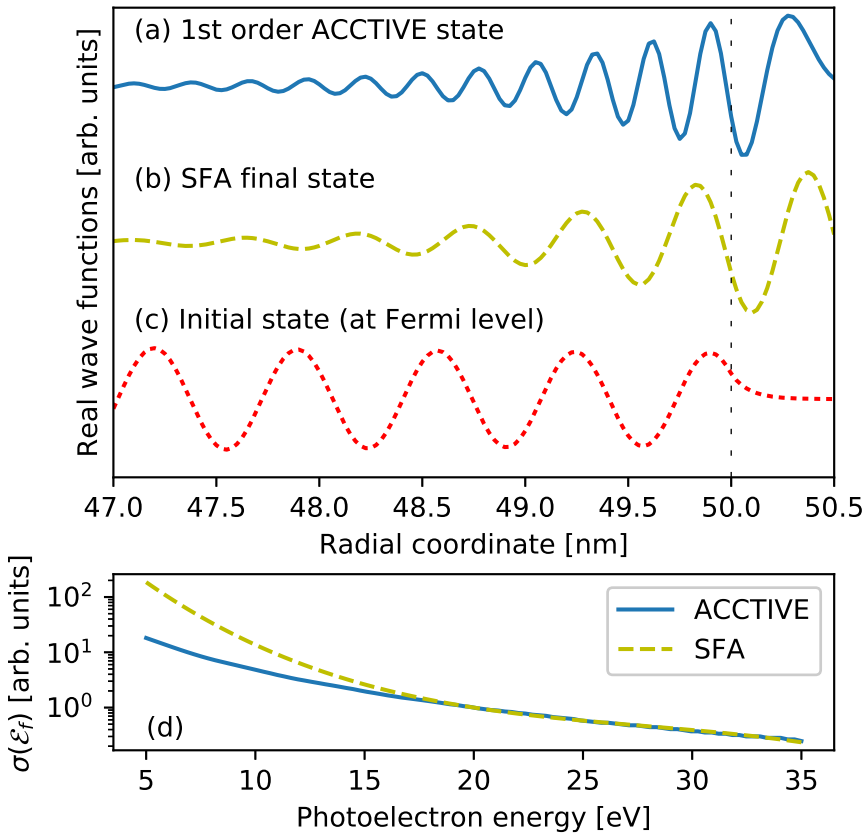


Figure B.3: *Real parts of photoelectron final-state wavefunctions near the surface of Au nanospheres along the XUV polarization direction: (a) 1st order ACCTIVE wavefunction and (b) SFA modeled wavefunction in Ref. [60], for the electron detection along the XUV polarization direction and asymptotic photoelectron energy $\mathcal{E}_f = 5$ eV. (c) Initial state wavefunction, modeled as bound state in a spherical square well potential, at the Fermi level. The vertical dashed line indicates the nanosphere surface. (d) Simulated XUV photoemission cross sections.*

B.3 Comments on streaked photoemission from Au nanospheres

Figure 4.5 in the main text shows the comparison of simulated streaked photoelectron spectra using either ACCTIVE wavefunctions as final states or Volkov wavefunction in SFA. ACCTIVE wavefunctions are more accurate at low photoelectron energy, but entail higher CoEs than Volkov wavefunctions [Fig. 4.5(c)]. In comparison with Fig. 4.4(d), this might appear as counter-intuitive. An explanation is given below.

Figure B.3(a) shows the real part of the 1st-order ACCTIVE wavefunction near the Au nanosphere surface, and Fig. B.3(b) the corresponding Volkov wavefunction in SFA [60]. Both are calculated for photoelectron detection along the XUV polarization direction and outgoing photoelectron energy $\mathcal{E}_f = 5$ eV. Inside the nanosphere, the Volkov final-state wavefunction neglects the spherical well potential. It therefore has a longer wavelength than the ACCTIVE wavefunction and more strongly overlaps with the initial-state wavefunction shown in Fig. B.3(c). Thus, the cross section, calculated following Ref. [88], is larger in SFA than if based on ACCTIVE final states.

This effect becomes less significant a larger photoelectron kinetic energies, where both, ACCTIVE and SFA wavefunctions have shorter wavelengths and overlap less with initial-state wavefunction. Figure B.3(d) shows that the energy-dependent photoemission cross sections calculated with ACCTIVE and Volkov final states converge at large photoelectron energies, while at small energies the SFA leads to larger cross sections. The net effect of this cross-section difference is to put more weight on photoelectron yields at lower energy and thus to shift streaking traces and CoEs in SFA photoemission spectra to lower energies as compared to ACCTIVE-calculated spectra.